d/Collection

공학박사 학위논문

Optimal production of olfactory receptors embedded in nanodisc and nanovesicle and their applications for pattern analysis and visualization of odors

나노디스크 및 나노베지클에 내장된 후각
수용체의 최적의 생산과 냄새의 패턴 및 시각화에
대한 응용

2022년 8월

서울대학교 대학원
공과대학 화학생물공학부

문 동 석

Optimal production of olfactory receptors embedded in nanodisc and nanovesicle and their applications for pattern analysis and visualization of odors

지도 교수 박 태 현

이 논문을 공학박사 학위논문으로 제출함

2022년 5월

서울대학교 대학원
공과대학 화학생물공학부
문 동 석

문동석의 공학박사 학위논문을 인준함
2022년 6월

위 원 장 _____황 석 연_____ (인)

부위원장 _____박 태 현_____ (인)

위 원 _____서 상 우_____ (인)

위 원 _____송 현 석_____ (인)

위 원 _____이 숭 환_____ (인)

Abstract

Optimal production of olfactory receptors embedded in nanodisc and nanovesicle and their applications for pattern analysis and visualization of odors

Dongseok Moon

School of Chemical and Biological Engineering

The Graduate School

Seoul National University

G protein-coupled receptors (GPCRs) are the most intensively studied for screening drug targets. Especially, class A GPCR including olfactory receptor (OR) which accounts for about 85 % of GPCR family is more important for codifying and screening target receptors. There are about 400 kinds of ORs in human olfactory system. The interactions between ORs and odorants generate signals which are transferred to brain as combinatorial codes. Humans can discriminate more than 1 trillion olfactory stimuli with a limited number of ORs because of widespread OR-driven modulation such as inhibition and enhancement in peripheral olfactory coding. Since the sense of smell perceives the complex external world as a pattern, many studies have been conducted to mimic the response of ORs. In particular, protein-based nanobiosensor is expected as a platform to mimic the olfaction because it has advantages such as mass production, ease of reuse, and low cost.

However, reconstitution of the structure of GPCRs is challenging

because almost all GPCRs produced in *E. coli* system are expressed as inclusion bodies. For this reason, reconstitution techniques have been developed to recover the functionality of GPCRs, such as the use of detergent micelles, nanovesicles, bicelles and nanodiscs (NDs). Among these materials, NDs have been considered the most effective reconstitution material because of their stability in various environments and their functional lifetimes.

In this thesis, ORs were produced in *E. coli* system with high productivity and reconstituted to ND or nanovesicle forms.   Then the functional reconstituted ORs were applied to monitoring meat freshness/spoilage, disease diagnosis and practical colorimetric sensor.

First, OR was overexpressed by coexpressing effector genes, such as *djlA*, the membrane-bound DnaK cochaperone, and *rraA*, inhibitor of the mRNA-degrading activity of *E. coli* RNase E. The *E. coli* strains coexpressing DjlA or RraA suppressed protein-induced toxicity and overexpressed the ORs. By controlling the molar ratio of OR, membrane scaffold protein, and phospholipid, ND of appropriate size were made, and high-purity ND could be purified. OR-embedded NDs showed stability to various temperature and storage time.

Second, Human ORs which bind to gastric cancer and halitosis biomarkers were successfully reconstituted to ND form and purified. The NDs had various patterns to artificial saliva samples because NDs had various binding affinities to target molecules. Through principal

component analysis of various patterns for artificial saliva samples, it was possible to distinguish between healthy control samples and patient samples.

Third, trace amine-associated receptors (TAARs), TAAR13c and TAAR13d, were successfully overexpressed in *E. coli* system and reconstituted to ND form. These NDs were utilized for development of ND-based BE-nose for monitoring meat freshness. The ND-based BE-noses was successfully performed towards diverse on-site and the various real samples and could be used to monitor freshness of meat.

Lastly, human OR1A2 (hOR1A2) was reconstituted into detergent micelle and it was used for development of colorimetric sensor detecting geraniol. Polydiacetylene (PDA) was used as secondary transducer for visualization of responses of OR. The structural and functional properties of the hOR1A2 were maintained when it was embedded in PDA/lipid nanovesicles. The hOR1A2 embedded in PDA/lipid nanovesicle caused a color transition from blue to purple when it reacted with geraniol, whereas there was no color transition when it reacted with other molecules.

In this study, various ORs were successfully reconstituted with ND or nanovesicles. The reconstructed OR is expected to be applied to food freshness monitoring, disease diagnosis by pattern analysis, and practical colorimetric sensors.

Student Number: 2015-22830

Contents

List of figures

11

List of tables

List of abbreviations

BE-nose: Bioelectronic nose
cAMP: cylic adenosine monophosphate
CD: Circular dichroism
CNT: Carbon nanotube
CPNT: Conducting polymer nanotube
CV: Cadaverine
Cymal 6: 6-Cyclohexylhexyl-β-D-maltoside
DDM: dodecyl-β-D-maltoside
DLS: Dynamic light scattering
DMEM: Dulbecco's Modified Eagles Medium
DMPC: 1,2-Dimyristoyl-sn-glycero-3-phosphocholine
DMSO: Dimethyl sulfoxide
E. coli: *Escherichia coli*
EDTA: Ethylenediaminetetraacetic acid
FBS: Fetal bovine serum
FE-SEM: Field-emission scanning electron microscopy
FET: Field-effect transistor
GC/MS: Gas chromatography-mass spectrometry
GPCRs: G protein-coupled receptors
HEK-293 cell: Human embryonic kidney 293 cell
HR-TEM: High-resolution transmission electron microscopy
IPTG: Isopropyl β-D-1-thiogalactopyranoside
Liquid chromatography-mass spectrometry: LC/MS
LOD: Limit of detection
MOB: Main olfactory bulb
MSP: Membrane scaffold protein
ND: Nanodisc
OBP: Odorant binding protein
OR: Olfactory receptors
OSN: Olfactory sensory neuron
PBS: Phosphate-buffered saline
PDA: Polydiacetylene
PT: Putrescine
SDS: Sodium dodecyl sulfate
SDS-PAGE: Sodium dodecyl sulfate-polyacrylamide gel electrophoresis
SEC: Size exclusion chromatography
Surface-enhanced Raman spectroscopy: SERS
TAARs: Trace amine-associated receptors
TCDA: 10,12-Tricosadiynoic acid
TMA: Trimethyl amine
VBN: Volatile basic nitrogen
VOC: Volatile organic compound

Chapter 1

Research background and objective

Research background and objective

ORs are chemoreceptors expressed in membranes of OSNs and are responsible for the perception of odorants which cause the sense of smell. Activated ORs trigger nerve impulses which transmit information of odor responses to the brain. ORs are members of the class A rhodopsin-like family of GPCRs. The OR gene superfamily is the largest in the human genome. It comprises 18 families and 301 subfamilies[1].

OR proteins have seven hydrophobic α-helix transmembrane domains, a disulfide connection between conserved cysteines in extracellular loops, a conserved glycosylation site in the N-terminal region[2], and multiple conserved amino acid sequences[3,4]. PMYFFL (transmembrane domain [TM] 2), MAYDRYVAIC (TM3), KAFSTC (TM6), and PMLNPXXY are among the OR consensus sequences found on the cytoplasmic side of each transmembrane region (TM7). Despite the fact that these consensus sequences differ slightly between species, they have been frequently employed to recover OR genes from genomes. Furthermore, thorough motif analysis has found more than 80 distinct short motifs, some of which serve as signature sequences for a certain species' OR subfamily or have implications for the function and development of ORs. These conserved motifs are likely involved in the proper folding of ORs in the plasma membrane, allowing ORs to bind odorants and connect to relevant G proteins. The transmembrane

regions, on the other hand, contribute to the formation of the odorant-binding pocket. Because the sequences in the binding pocket are somewhat varied, ORs can bind a diverse range of odorant molecules.

Neurons in the olfactory system have been demonstrated to transform the strength of excitatory input into response delay[5], and it has been hypothesized that ORs with high affinity will depolarize OSNs earlier than those with low affinity[6–8]. This results from a number of processes, including intracellular signal integration[9] and the temporal dynamics of odorant concentration[10–12]. Sniffing influences the temporal dynamics of odorant concentration in the nose in air-breathing animals, resulting in an affinity-defined sequence of OSN recruitment. While these recruitment sequences varied amongst odorants, they have been demonstrated to be mostly concentration invariant, since changes in concentration preserve temporal ranks of ORs with various affinities, and these latencies are considered to encode information about odor identity[7,13].

The type of nanobiosensor for the detection of smell and taste is mainly composed of two parts, biomaterials as primary transducer, and nanomaterials as secondary transducer. Biomaterials are usually receptors derived from various organisms. These have higher selectivity to ligands, compared to chemical-based receptors. In the nanobiosensor system, biomaterials are immobilized on secondary transducers, and retain the ability to interact with target ligands. Secondary transducers

are the devices that convert biological interactions to other signals, such as electrical signals. The events of interactions between receptors and ligands occur at nanoscale, and are unable to be observed by the naked eye. Secondary transducers change the events to detectable electrical signals. Users can assume the ligand-receptor interaction by analyzing the electrical signals that occur in the nanobiosensor system.

GPCRs are very hard to be overexpressed in *E. coli* systems because of hydrophobicity of their complex structure, seven transmembrane protein. There are three main reasons for GPCRs production in *E. coli* system: (1) there is usually very low level of membrane-incorporated GPCRs per cell, (2) when the amount of GPCRs in the cell membrane are accumulated with substantial level, there is typically a very low amount of GPCRs that is produced in a well-folded and functional structure, and (3) significant levels of toxicity for the host are typically associated with overexpression[14,15].

Despite these clear limitations, there have been some reports of GPCRs expressed successfully in *E. coli*[16–18]. Unmodified GPCRs tend to be expressed as inclusion bodies and may aggregate in such systems[16]. The use of fusion partners or tags is a key strategy for effective expression and well-folding of GPCRs in the *E. coli* system[19]. These aid in both expression and purification by directing the precise insertion of GPCRs into the membrane and enhancing its overall solubility[20]. Furthermore, some approaches such as selective mutagenesis to generate mutations

and the use of insertion or truncation have been shown to be effective in some researches[16,21]. Indeed, *E. coli* genetic alteration can be utilized to select for variations with higher stability and expression, even for somewhat difficult to manage receptors[22,23].

In summary, the objectives of this study are:

1. Enhancement of OR production in *E. coli* system and characterization of OR-embedded nanodiscs

2. Development of nanodisc-based bioelectronic nose using trace amine-associated receptors for monitoring meat freshness/spoilage

3. Pattern analysis for gastric cancer biomarkers using human OR-embedded nanodiscs

4. Pattern analysis for halitosis biomarkers in artificial saliva using human OR-embedded nanodiscs

5. Visual detection of geraniol using human OR embedded in polydiacetylene/lipid nanovesicle

Chapter 2

Literature review

2.1 Olfaction

2.1.1 Olfactory system

The olfactory system, or sense of smell, is the sensory system used for detecting odorants (olfaction). Olfaction is one of the special senses, that have directly associated specific organs. Most of the breakthrough discoveries was done by Richard Axel at Columbia University (New York, NY, USA) and Linda Buck at the Fred Hutchinson Cancer Research Center in Seattle (WA, USA), who won the 2004 Nobel Prize in Physiology or Medicine "for their discoveries of odorant receptors and the organization of the olfactory system". Their discoveries provide a picture of how sensory neurons in the olfactory epithelium of the nose detect odorants, which, in turn, transmits this information to the olfactory bulb that passes the signal on to the olfactory cortex (**Figure 2.1**)[24].

OSNs send their signals through axons into a part of the forebrain known as the olfactory bulb. The researches using transgenic mice have shown that all the neurons expressing only one particular receptor, no matter where they are found on the olfactory epithelium, converge to a single 'odorant' in the olfactory bulb[25]. These targets are the glomeruli, spherical conglomerates of neuropil some 50–100 μm in diameter that consist of the incoming axons of OSNs and the dendrites of the main projection cell in the olfactory bulb, the mitral cell.

G-proteins contain three subunits; an alpha subunit, known as Gα-olf which is specific to the ORs, a beta subunit and a gamma subunit. G-alpha is considered as the active unit while beta and gamma subunits regulate the activity of the alpha subunit. While in inactive state, alpha subunit binds to GDP. OR activates on binding to an odorant and causes a transduction cascade. The activation initiates conformational changes in OR, both tilting and rotation of TM6 relative to TM3[26–29]. Coupling of stimulated OR and G-protein, causes a replacement of GDP in the alpha subunit by GTP. GTP bound Gα-olf dissociates itself from beta- and gamma- subunits and moves on to stimulate adenylyl cyclase III (ACIII), which cyclizes adenosine triphosphate (ATP) into second messenger, cAMP. Various studies have indicated the vital role of cAMP in olfactory signal transduction[30–36]. The increased intracellular concentration of cAMP moves throughout the cell cytoplasm and causes olfactory-specific cyclic nucleotide-gated channel (CNG) (ion-channels) to be activated. CNG channel leads to an influx of extracellular calcium and sodium ions into the OSN. Calcium influx through CNG channels activates Ca2+-gated Cl- channel, causing efflux of chloride ion from the OSN through cilia. The concentration of cAMP is decreased as it hydrolyzes to AMP. Meanwhile, the G-alpha terminates its own activity, hydrolyzes GTP to GDP, reunites to the beta and gamma subunits and remains its resting state[37] (**Figure 2.2**).

Mitral cell

Glomerulus

Olfactory bulb

Bone

Nasal epithelium

Olfactory receptor cells

Air with odorant molecules

4. The signals are transmitted to higher regions of the brain

3. The signals are relayed in glomeruli

2. Olfactory receptor cells are activated and send electric signals

1. Odorants bind to receptors

Odorant receptor
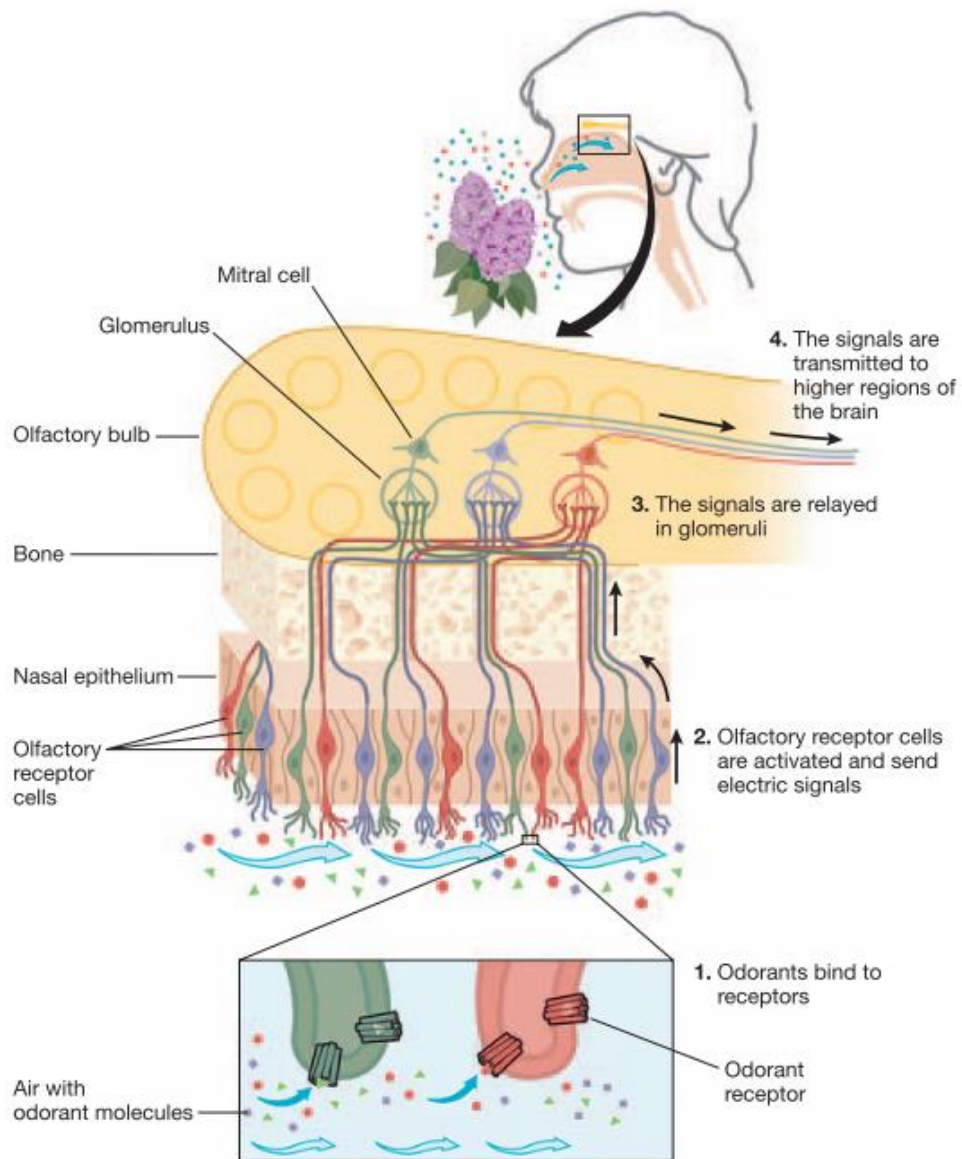
Figure 2.1 The human olfactory system

A. Rinaldi, *EMBO reports* **8, 629-633 (2007)**
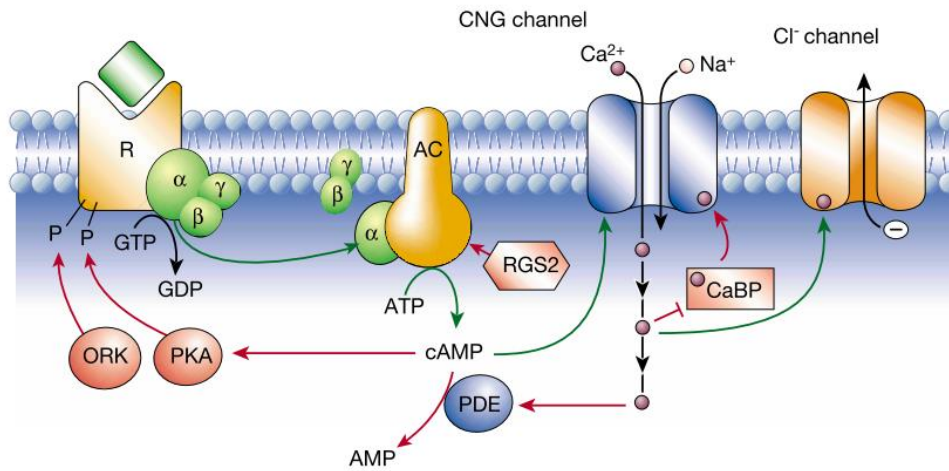
Figure 2.2 Signal transduction in ONS

S. Firestein, *Nature* **413, 211–218 (2001).**

2.1.2 Olfactory receptors

ORs are chemoreceptors expressed in membranes of OSNs and are responsible for the perception of odorants which cause the sense of smell. Activated ORs trigger nerve impulses which transmit information of odor responses to the brain. ORs are members of the class A rhodopsin-like family of GPCRs. The OR gene superfamily is the largest in the human genome. It comprises 18 families and 301 subfamilies[1] (**Table 2.1**).

OR proteins have seven hydrophobic α-helix transmembrane domains, a disulfide connection between conserved cysteines in extracellular loops, a conserved glycosylation site in the N-terminal region[2], and multiple conserved amino acid sequences[3,4]. PMYFFL (transmembrane domain [TM] 2), MAYDRYVAIC (TM3), KAFSTC (TM6), and PMLNPXXY are among the OR consensus sequences found on the cytoplasmic side of each transmembrane region (TM7) (**Figure 2.3**). Despite the fact that these consensus sequences differ slightly between species, they have been frequently employed to recover OR genes from genomes. Furthermore, thorough motif analysis has found more than 80 distinct short motifs, some of which serve as signature sequences for a certain species' OR subfamily or have implications for the function and development of ORs. These conserved motifs are likely involved in the proper folding of ORs in the plasma membrane, allowing ORs to bind odorants and connect to relevant G proteins. The transmembrane

regions, on the other hand, contribute to the formation of the odorant-binding pocket. Because the sequences in the binding pocket are somewhat varied, ORs can bind a diverse range of odorant molecules.

No.	Family	No. of Subfamily	No. of genes	No. of pseudo-genes	Chromosome
1	OR1	21	28	11	1, 5, 9, 11, 16, 17, 19, X
2	OR2	41	67	46	1, 5, 6, 7, 9, 11, 12, 16, 19, X
3	OR3	3	4	2	1, 17, X
4	OR4	24	57	80	1, 5, 6, 8, 11, 14, 15, 18, 19, 21, X
5	OR5	49	47	64	2, 3, 6, 9, 11, X
6	OR6	21	30	21	1, 2, 7, 8, 10, 11, 12, 14
7	OR7	9	11	102	2, 3, 4, 5, 7, 8, 9, 10, 11, 12, 13, 14, 19, 21
8	OR8	18	24	23	11, 12
9	OR9	12	9	14	1, 2, 7, 11, 12
10	OR10	28	36	28	1, 6, 7, 11, 12, 14, 19
11	OR11	11	8	17	1, 5, 12, 14, 15, X
12	OR12	1	2	1	6
13	OR13	11	12	10	1, 9, 10, X
14	OR14	6	6	1	1, 6
15	OR51	21	23	21	11
16	OR52	22	26	23	11
17	OR55	1	0	1	11
18	OR56	2	6	3	11
Total number	18	301	396	468	

Table 2.1 Human olfactory receptor family

27
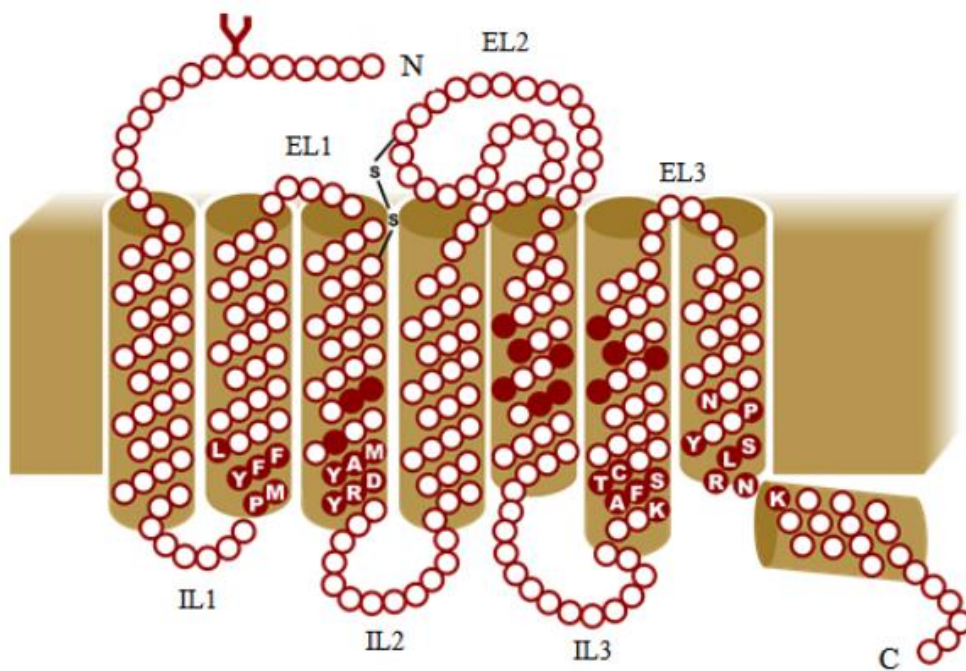
Figure 2.3 Transmembrane topology of olfactory receptor (OR)

A. Sharma *et. al.*, *Curr. Neuropharmacol.* **17, 891–911 (2018).**

2.1.3 Patterns of odorants

Odorant features are represented by a combinatorial code in the current model of the olfactory system (**Figure 2.4**). Each odorant has a unique set of characteristics that are extracted by the receptors and represented as distinct glomeruli in the MOB. Although odorant molecular features are thought to be a key determinant of olfactory perception, the rules governing this relationship are unknown. The relationship between perceptual properties, molecular structure, and neural response, or any combination of these, is unclear. Three basic principles emerge from spatial patterns of ORs. First, individual odorants activate subsets of receptors. This finding lends support to a hypothesis of combinatorial coding in which most odorants are identified not by the response of a single receptor, but by a pattern of receptor responses. Second, subsets of odorants activate particular receptors. ORs vary in their breadth of tuning: some are broadly tuned, responding to many odorants, while others are narrowly tuned, responding to only a few specific odorants. Broadly tuned receptors are particularly sensitive to odorants that are structurally similar. Third, increased odorant concentrations stimulate activity from a larger number of receptors. Thus, the number of active receptors represents both odor strength and odor identity[38–43].

Neurons in the olfactory system have been demonstrated to transform the strength of excitatory input into response delay[5], and it has been hypothesized that ORs with high affinity will depolarize OSNs earlier

than those with low affinity[6–8]. This results from a number of processes, including intracellular signal integration[9] and the temporal dynamics of odorant concentration[10–12]. Sniffing influences the temporal dynamics of odorant concentration in the nose in air-breathing animals, resulting in an affinity-defined sequence of OSN recruitment. While these recruitment sequences varied amongst odorants, they have been demonstrated to be mostly concentration invariant, since changes in concentration preserve temporal ranks of ORs with various affinities, and these latencies are considered to encode information about odor identity[7,13].

Figure 2.4 Spatial patterns of peripheral activation of ORs

S. Firestein, *Nature* 413, 211-218 (2001).

2.2 Nanobiosensor

2.2.1 Nanobiosensor system

Figure 2.5 shows the concept of the nanobiosensor utilizing olfactory or taste receptors. These sensors have both the advantages of high selectivity of sensory receptors and high sensitivity of nanomaterial-based electronic sensing platforms.

The type of nanobiosensor for the detection of smell and taste is mainly composed of two parts, biomaterials as primary transducer, and nanomaterials as secondary transducer. Biomaterials are usually receptors derived from various organisms. These have higher selectivity to ligands, compared to chemical-based receptors. In the nanobiosensor system, biomaterials are immobilized on secondary transducers, and retain the ability to interact with target ligands. Secondary transducers are the devices that convert biological interactions to other signals, such as electrical signals. The events of interactions between receptors and ligands occur at nanoscale, and are unable to be observed by the naked eye. Secondary transducers change the events to detectable electrical signals. Users can assume the ligand-receptor interaction by analyzing the electrical signals that occur in the nanobiosensor system.

There have been many approaches taken to immobilize the biomaterials on nanomaterials. Nanovesicles including ORs were immobilized on carbon nanotube by a charge-charge interaction, because the lipid

bilayer of the nanovesicle has negative charges, while poly-D-lysine (PDL) has positive charges[44–48]. Nickel-functionalized CNT was used to immobilize the ORs because nickel has high affinity with polyhistidine-tag at C-terminus of OR[49]. OR-derived peptide was immobilized by interaction between phenylalanine residues of peptide and CNT, which is called π–π stacking[50–52]. Recently, OR-embedded NDs were immobilized on the CNT-FET sensor by half-V5 antibody used as a linker[53,54]. Half-V5 antibody generates disulfide bonding with gold, which is on the gold-based floating electrode CNT-FET sensor. V5 tag at the C-terminus of the OR has antigen-antibody binding with half-V5 antibody, which is coated on gold floating electrode. Using the half-fragment V5 antibody, OR-embedded NDs could be immobilized with the desired orientation.
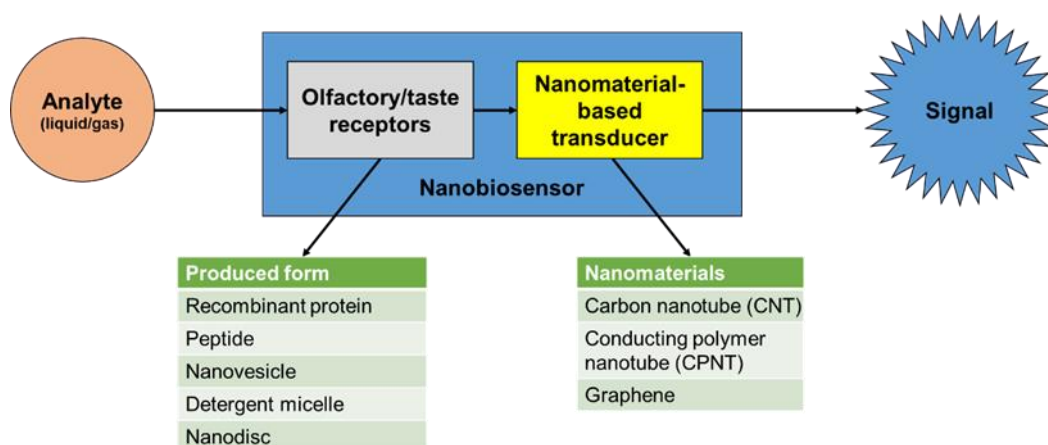
Figure 2.5 Scheme of nanobiosensors composed of olfactory/taste receptors and nanomaterials

2.2.2 Components for the nanobiosensor

Since the human olfactory mechanism has been elucidated, some researchers have developed the electronic nose that mimics the olfactory system for volatile chemical compounds. It is composed of sensor arrays, each one of which has different selectivity to a volatile compound[55]. In the field of taste sensors, researchers have also utilized sensor arrays based on metallic or lipid-polymer compounds for the electronic tongue[56]. To enhance the selectivity and sensitivity of the electronic nose and tongue, other researchers use biomaterials that can bind to specific ligands. In the beginning, human nasal and taste epithelium was immobilized on microarray electrode[57,58]. Furthermore, artificial cells expressing human receptor proteins were utilized as biomaterials within surface plasmon resonance (SPR) and quartz crystal microbalance (QCM)[59,60]. Epithelium and artificial sensory cells can mimic human sensory systems, but these are difficult to prepare in large quantities, and are very unstable. To improve the stability and selectivity of nanobiosensor, various types of biomaterials have been developed to replace the epithelium and artificial sensor cells. In addition, sensor platforms should be more sensitive, easy-to-use, and allow real-time measurement. For these purposes, the FET is a candidate for the nanobiosensor platform for the next generation. The FET is an electrical device whose flowing current is controlled by an electrical field. The electrolyte gate layer includes biomaterials and ligand solution. Hence,

interactions between receptors and ligands are converted into amplified channel current in the electrical field of the electrolyte gate between source and drain electrodes. Moreover, the FET-based nanobiosensor adopts nano-sized materials as channels. Carbon-based materials, including carbon nanotube and graphene, can be used as channel materials [61,62]. Biomaterials are easily immobilized on carbon materials, and these carbon materials have the potential for mass production. Conducting polymer-based organic FET can also be used with receptor proteins[63]. Therefore, nano-sized biomaterials can be combined with the nanomaterial-based FET to develop high-performance nanobiosensors.

Nanovesicles derived from artificial cells expressing olfactory and taste receptors have a similar signal pathway to olfactory neurons and taste buds. After specific ligands bind to receptors on the surface of nanovesicles, calcium ion influx occurs by signal pathway cascade and is converted to electrical signal by transducers such as CNT-FET[44,61]. The nanovesicle has the advantage of being more stable than using artificial cells. This system using nanovesicles mimics the human sensory pathway, and demonstrates olfaction and taste signal transduction, which is induced by the ligand-receptor interaction, like artificial cells.

The receptor protein itself was also utilized with FET. The binding of specific ligands induces conformational change of the receptor proteins. FET converts the signal of conformational change into electrical signals

and amplifies the signals with their altering electrostatic distribution. In previous studies, the insoluble fraction of human ORs from *E. coli* was used with FET[63,64]. Peptides derived from OR or OBP were immobilized on transducer for advanced stable and high performance[52].

Recently, human OR-embedded in detergent micelle or ND for the reconstitution of membrane receptor proteins have been applied to nanobiosensors[49,53]. In the development of the bioelectronic tongue, purified and reconstituted taste receptor proteins in the form of a detergent micelle were combined with nanomaterials and showed high sensitivity and selectivity[62,65]. For the reconstitution of these proteins, they can be produced in large quantities from *E. coli*. In the form of reconstitution, NDs have a high stability, comparable to other reconstituted proteins[66]. The ND is composed of phospholipids that mimic the native environment of cell membrane and MSP that encircle the hydrophobic region of the phospholipid bilayer for stable structure of the receptor. The ND is the most promising biomaterial in the nanobiosensor field.

2.2.3 Nanobiosensor detecting smell

Nanobiosensors that can detect various smells have been developed over many years (**Table 2.2**). The nanobiosensors have excellent sensitivity and selectivity to target molecules. Biomolecules, such as OR and olfactory peptide, have selectivity to target ligands.

Nanomaterials, such as CNT and CPNT, can sensitively transduce the conformational change of nanovesicle, ND, and detergent micelle to electric device. In particular, the nanovesicle transfers the odorant signal to nanomaterials *via* cAMP signal pathway or IP$_3$ pathway, causing calcium signaling[67] (**Figure 2.6**).

Human ORs have been used as a biomaterial of nanobiosensors for the detection of various smells, because of their selectivity to target smell molecules. hOR2AG1, which binds to amyl butyrate, pear or apricot smell, was used to mimic the human olfactory system[44,48,62,63,68,69,70]. Human ORs (hOR2J2, hOR2W1) produced in *E. coli* were used to detect food contamination. Octanol and hexanal are indicators for bacterial contamination in beef, and lipid oxidation of dairy products, respectively. The human OR-based nanobiosensor could also distinguish contaminated foods such as beef, pork, cheese and milk[49]. hOR3A1 selectively binds with helional which has floral smell[71]. hOR3A1 produced in *E. coli* was immobilized on CPNT or graphene by covalent bonding[64], or π–π stacking[68]. hOR3A1-based nanobiosensors could selectively detect liquid or gas phase helional, and each hOR3A1-based nanobiosensor has 0.1 fM and 0.02 ppt LOD. Son et al. (2015) deorphanized hOR3A4 and hOR51S1 by using luciferase assay. hOR3A4 and hOR51S1 bound with 2-methylisoborneol and geosmin, respectively. 2-Methylisoborneol and geosmin are produced when water is contaminated by cyanobacteria[72]. The nanobiosensor that has two channels and is immobilized with single-type nanovesicle containing

hOR3A4 or hOR51S1 could sensitively detect 2-methylisoborneol and geosmin, indicators of water contamination in real-time. Yang et al. (2017) developed the nanobiosensor capable of detecting a CV, death-associated odor, which is generated by the bacterial decarboxylation of lysine. CV can be a target molecule for the evaluation of food spoilage. TAAR13c, which originated from Zebrafish (*Danio rerio*), was used as biomaterials, selectively binding to CV. TAAR13c-embedded ND was constructed and immobilized on floating electrode CNT-FET with the desired orientation. The nanobiosensor could selectively detect the target molecules from real samples, such as spoiled salmon and beef. As the spoilage period of real samples was longer, the death-associated odor nanobiosensor showed higher responses to the real samples.

Canine OR (cfOR5269) was also used for real-time assessment of food quality[46]. Hexanal was identified as a VOC that was produced in oxidation of lipid[73]. The nanobiosensor that contains cfOR5269-embedded nanovesicles could detect hexanal as low as 1 fM. Wu and Lo (2000) established the oligo-peptide sequences (NQLSNLSFSDLCFFF), which was derived from dog OR (*olfd canfa*). The peptide could selectively bind with trimethylamine (TMA), which could be used as a good indicator for sea food quality[75]. Lim et al. (2013) and Lee et al. (2015) developed nanobiosensors, that could sensitively detect TMA in liquid or gas phase. Each nanobiosensor had 10 fM and 100 ppt LOD, respectively. Additionally, the nanobiosensors could sensitively examine the quality of sea food samples, such as oyster,

shrimp, and lobster. Another peptide-based nanobiosensor that could assess the *Salmonella* contamination of food was developed[50]. Through GC/MS, 3-methyl-1-butanol was identified as a major VOC of *Salmonella*-contaminated ham[76]. *Drosophila* OBP-derived peptide was used to detect 3-methyl-1-butanol from *Salmonella*-contaminated ham. The nanobiosensor could detect 3-methyl-1-butanol as low as 1 fM, and assess the degree of *Salmonella* contamination of food. These results show that the nanobiosensors using ORs and related derivatives can be used to quantitatively evaluate the quality of food, by smelling the odors derived from various spoiled foods.

Lee et al. (2018) developed the nanobiosensor that mimics human smelling rose odorants (geraniol, citronellol). Like the human olfactory system, the CNT-FET sensor immobilized with hOR1A2-embedded ND showed the responses when it was treated with ligands, and showed higher response by the treatment of ligand and enhancer.

Since a well-trained dog discriminates cancer patients from healthy people with high accuracy, many interests have focused on how to diagnose diseases by smell. Here, a nanobiosensor to replace the role of a dog was developed to smell the specific odor derived from a cancer. Lim et al. (2014) developed the nanobiosensor that could be applied to the diagnosis of lung cancer. Heptanal was identified as a volatile biomarker of lung cancer[77]. By using a calcium signaling assay, hOR1J2 was identified as a receptor for the specific binding with a heptanal. The

CNT-FET sensor immobilized with nanovesicles containing hOR1J2 could selectively and sensitively detect the target molecules. Also, the nanobiosensor could distinguish heptanal from human blood plasma in real-time.

Thus, it is expected that the development of nanobiosensors that detect diverse smells can be applied to extensive fields related to the odors.

Receptor	Type	Transducer	Target (phase)	Odor	LOD	Refs.
TAAR13c	nanodisc	CNT-FET*	cadaverine (liquid)	foul	10 pM	(Yang et al., 2017)
hOR1A2	nanodisc	CNT-FET	geraniol, citronellol (liquid)	floral	1 fM, 10 fM	(Lee et al., 2018)
olfactory receptor-derived peptide	peptide	CNT-FET	trimethylamine (liquid, gas)	fishy	10 fM, 100 ppt	(Lim et al., 2013), (Lee et al., 2015)
odorant binding protein-derived peptide	peptide	CNT-FET	3-methyl-1-butanol (liquid)	whiskey	1 fM	(Son et al., 2016)
hOR1J2	nanovesicle	CNT-FET	heptanal (liquid)	fatty	10 fM	(Lim et al., 2014)
hOR3A4, hOR51S1	nanovesicle	CNT-FET	geosmin, 2-methylisoborneol (liquid)	earthy, musty	10 ng/L	(Son et al., 2015)
hOR3A1	recombinant protein	CVD graphene* CPNT-FET*	helional (liquid, gas)	floral	0.1 fM, 0.02 ppt	(Kwon et al., 2015), (Lee et al., 2012b)
hOR2AG1	recombinant protein	CPNT-FET	amyl butyrate (liquid)	fruity	400 fM	(Yoon et al., 2009)
		CVD graphene			0.04 fM, 0.01 fM	(Park et al., 2012b), (Kwon et al., 2015)
		CNT-FET			100 fM, 1fM	(Kim et al., 2009), (Lee et al., 2012a)
	nanovesicle	CNT-FET			1 fM	(Jin et al., 2012), (Lim et al., 2015)
hOR2J2	detergent micelle	CNT-FET	octanol (liquid)	soap	1 pM	(Son et al., 2017a)
hOR2W1	detergent micelle	CNT-FET	hexanal (liquid)	fruity	1 pM	
cfOR5269	nanovesicle				1 fM	(Park et al., 2012a)

* CNT-FET (carbon nanotube-field effect transistor); CPNT (conducting polymer nanotube); CVD (chemical vapor deposition)

Table 2.2 Natural biomaterial-based nanobiosensors that detect various odors
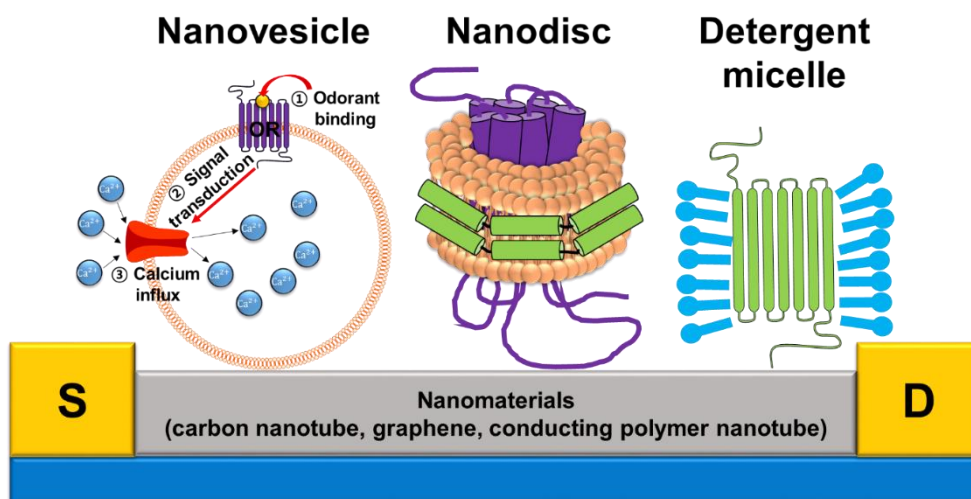
Figure 2.6 Schematics of nanobiosensors showing olfactory receptor based-biomaterials that are immobilized on nanomaterials (OR: olfactory receptor)

2.3 Biomarkers in disease and food spoilage

2.3.1 Gastric cancer

Gastric cancer (cardia and noncardia gastric cancer combined) is the fifth most often diagnosed cancer and the third largest cause of cancer death, accounting for approximately 1,000,000 new cases in 2018 and an estimated 783,000 deaths (equating to 1 in every 12 deaths globally) (**Figure 2.7**)[78].

Helicobacter pylori is the leading cause of stomach cancer, accounting for about 90% of new occurrences of noncardia gastric cancer[79]. Although international diversity in *H. pylori* prevalence correlates reasonably with stomach cancer incidence, additional factors are likely to play a significant role. There is a nutritional component, with salt-preserved foods and a lack of fruits raising risk, and both alcohol drinking and active cigarette smoking are proven risk factors[80].

Although they are frequently presented as a single entity, gastric cancers can be divided into two topographical types. Noncardia gastric cancer rates (arising from more distant regions) have been steadily dropping in most populations over the previous half-century. The trends are related to success of prevention, such as a lower prevalence of *H. pylori* and breakthroughs in food preservation and storage[81]. Cancers of the gastric cardia (arising in the area adjacent to the esophageal-gastric junction) have epidemiological characteristics more similar to esophageal

adenocarcinoma (AC), and important risk factors include obesity and gastroesophageal reflux disease (GERD), with Barrett esophagus (a condition caused by GERD) also thought to increase risk; the incidence of these cancers has been increasing, particularly in high-income countries[78].

Many researchers analyzed breath from gastric cancer patients and found some VOCs regarded as gastric cancer biomarkers, such as fatty acids, phenol and aldehyde[82–85] (**Table 2.3**).

Previous research has found a link between short-chain fatty acids (SCFAs) and gastrointestinal cancer. Some SCFAs, such as acetic acid, butyric acid, and propionic acid, are known to be generated by colonic bacteria through anaerobic fermentation of dietary carbohydrates[86,87]. Butyric and propionic acids have also been shown to cause apoptosis in a gastric carcinoma cell line[88]. As a result, SCFA monitoring is anticipated to be critical for understanding the activity of cancer cells in the digestive tract. Furthermore, several studies propose that SCFAs act as potent indicators in the exhaled breath of stomach cancer patients. Cross-platform validation has confirmed that butyric acid, valeric acid, and hexanoic acid are biomarkers of gastrointestinal cancer in the breath[82,84,89,90].

Figure 2.7 Pie charts present the distribution of cases and deaths for the 10 most common cancers in 2018 for both sexes

F. Bray, *et. al.***,** *CA. Cancer J. Clin.* **68, 394–424 (2018).**

Biomarker	Reference
acetone, formaldehyde, acetaldehyde, hexanoic acid, hydrogen sulfide, hydrogen cyanide, and methyl phenol	S. Kumar, *et al.*, *Analytical chemistry* 84, 2012.
hexanoic acid, phenol, methyl phenol, and ethyl phenol	S. Kumar, Sacheen, *et al.*, *Analytical chemistry* 85, 2013.
valeric acid, hexanoic acid, phenol, methyl phenol, ethyl phenol, butanal, pentanal, hexanal, heptanal, octanal, nonanal, and decanal	S. Kumar, Sacheen, *et al.*, *Annals of surgery* 262, 2015.
butyric acid, valeric acid, and hexanoic acid	M. Adam, *et al., Analytical chemistry* 91, 2019.
propionic acid and butyric acid	S. W. Cho, writing a paper

Table 2.3 Biomarkers of gastric cancer

2.3.2 Halitosis

Halitosis is a broad term that refers to any unpleasant odor that emanates from the mouth, air, or breath, regardless of the source of the odor compounds[91–93]. VOCs in human breath will have originated from multiple sources inside the respiratory system. There are three major VOC sources that can be identified: (1) exogenous sources; VOCs inspired from background ambient gases and then expelled; (2) extra-oral; from microbes further down the respiratory tract (oropharynx, bronchioles), or else blood- circulatory VOCs that enter the lungs and are removed from the body through gaseous exchange; and (3) intra-oral; microbial VOCs from microbial biofilms encountered in the oral cavity[94]. Because of microbial activity from biofilms within the oral cavity, the majority of human people with halitosis (80 to 90 percent) have oral malodour[92].

The VOCs causing halitosis are sulfur compounds, diamines, short-chain fatty acids, alcohols, phenyl compounds and ketones (**Table 2.4**)

Categories	Compounds
Volatile sulfur compounds	Methyl mercaptan
	Hydrogen sulfide
	Dimethyl sulfide
Diamines	Putrescine
	Cadaverine
Short-chain fatty acids	Butyric acid
	Propionic acid
	Valeric acid
Phenyl compounds	Indole
	Skatole
	Pyridine
Alcohols	Methanol
	Ethanol
	Propanol
Ketones	Acetone

Table 2.4 Volatile molecules contributing to oral malodour

2.3.3 Meat spoilage

Food safety is a major concern in the worldwide, in both the food industry and the healthcare system[95]. In particular, among numerous information of the food products in both consumer and modern society, food spoilage is the main issue because of the critical negative effect on humans of food containing unsafe microorganisms[96]. For example, meat is a perishable food that usually deteriorates rapidly, within a few days[97]. Meat spoilage progresses in time via biochemical and physicochemical transformations[98]. In the biochemical spoilage process of meat, decarboxylation of amino acids by bacteria generates biogenic amines[99,100]. In addition, the amino acids in meat can be degraded into simple compounds such as NH_3 and H_2S by hydrolysis[98]. These biogenic amines and small chemical compounds produced by the deterioration of meat can be used as spoilage indicators. Targets indicating the freshness of food are normally complex mixtures; therefore, the development of monitoring tools offering multiplexed platforms for the detection of these spoilage indicators with high selectivity is required.

CV and PT are biogenic amines that are produced by the microbial decarboxylation of amino acids[101]. CV and PT are formed by the decarboxylation of lysine and ornithine, respectively[99,100]. There have been reports that the mass of CV and PT increases with the incubation time of fresh meat, such as pork, beef, sausage, anchovy and tuna[100,102–

[104]. For this reason, CV and PT have been suggested as chemical indicators of meat spoilage, and monitoring the concentrations of the generated biogenic amines is important for determining food freshness and spoilage[105].

2.4 Expression of GPCR in *E. coli* system

GPCRs are very hard to be overexpressed in *E. coli* systems because of hydrophobicity of their complex structure, seven transmembrane protein. There are three main reasons for GPCRs production in *E. coli* system: (1) there is usually very low level of membrane-incorporated GPCRs per cell, (2) when the amount of GPCRs in the cell membrane are accumulated with substantial level, there is typically a very low amount of GPCRs that is produced in a well-folded and functional structure, and (3) significant levels of toxicity for the host are typically associated with overexpression[14,15].

Despite these clear limitations, there have been some reports of GPCRs expressed successfully in *E. coli*[16–18]. Unmodified GPCRs tend to be expressed as inclusion bodies and may aggregate in such systems[16]. The use of fusion partners or tags is a key strategy for effective expression and well-folding of GPCRs in the *E. coli* system[19]. These aid in both expression and purification by directing the precise insertion of GPCRs into the membrane and enhancing its overall solubility[20]. Furthermore,

some approaches such as selective mutagenesis to generate mutations and the use of insertion or truncation have been shown to be effective in some researches[16,21]. Indeed, *E. coli* genetic alteration can be utilized to select for variations with higher stability and expression, even for somewhat difficult to manage receptors[22,23].

In recent studies, development of *E. coli* strains for suppressing membrane protein-induced toxicity and obtaining high-level recombinant membrane protein[106–108]. The *E. coli* strains co-expressing DjlA, the membrane-bound DnaK cochaperone and RraA, the inhibitor of the mRNA-degrading activity of the *E. coli* RNase E, showed high productivity of GPCRs such as cannabinoid receptor, neurotensin receptor, neurokinin receptor and bradykinin receptor which are belong to class A GPCR.

Chapter 3

Experimental procedures

3.1 Materials

10,12-Tricosadiynoic acid (TCDA) powder was purchased from GFS Chemicals, Inc. 1,2-Dimyristoyl-sn-glycero-3-phosphocholine (DMPC) was purchased from Avanti Polar Lipids, Inc. Tris buffered saline (TBS) was prepared using 100 mM Tris-HCl (pH 7.4), 300 mM NaCl, 1 mM DDM, 1 mM Cymal-6, and 1 mM EDTA. All odorants (geraniol, trimethylamine (TMA), helional, and amyl butyrate (AB) were purchased from Sigma-Aldrich. For the specificity test, all odorants were prepared in dimethyl sulfoxide (DMSO, Sigma-Aldrich). Deionized (D.I.) water was purified with a Millipore water purifier, and its resistivity was 18.2 MΩ cm. IPTG, EDTA, sodium phosphate, DDM, cymal-6, glutathione reduced (GSH), glutathione oxidized (GSSG), sodium chloride, methyl-β-cyclodextrin, linalool, α-damascone, geranyl chloride, geranyl formate, 1,7-octandiene, 3,7-dimethyl-1-octanol, geraniol, hydroxylamine, ethanolamine, putrescine, cadaverine 1,10-diaminodecane, thiamine, tryptamine, L-lysine, acetic acid, propionic acid, butyric acid, valeric acid and hexanoic acid were purchased from Sigma-Aldrich. Sodium cholate, HEPES and SDS were purchased from Sigma-Aldrich. Rosetta TM 2 (DE3) *E. coli* strain (Merk Millipore) were used for expressing ORs and membrane scaffold protein.

3.2 Gene Cloning

Human OR 1A2, 51E1, 51E2, 52D1 and 51B4 genes were cloned in the pET-DEST42 vector containing hexahistidine tags for *E. coli* expression.

TAAR13c gene was obtained from zebrafish (Danio rerio) cDNA by PCR with primers (5′ ATG AAT TCA TGG ATT TAT CAT CAC AAG AAT 3′ and 5′ ATC TCG AGT CAA ACC GTA AAT AAA TTG ATA 3′) for mammalian expression and (5′ CAC CAG GAG ATA TAC ATA TGA TGC CCT TTT GCC ACA AT 3′ and 5′ TGA ACT CAA TTC CAA AAA TAA TTT ACA C 3′) for bacterial expression. The TAAR13c gene was cloned into mammalian expression vector pcDNA3 and the bacterial expression vector pET-DEST42 (Invitrogen). The TAAR13d gene was synthesized for codon optimization in a bacterial expression system (Bionics). Additionally, the TAAR13d gene was cloned into the mammalian expression vector pcDNA3 and the bacterial expression vector pET-DEST42 (Invitrogen).

3.3 Expression
3.3.1 Expression of olfactory receptors in *E. coli*

The Rosetta™ 2 (DE3) *E. coli* strain (Merck) was used for production of all proteins. SuptoxD and SuptoxR which coexpress DjlA and RraA, respectively, were used to overexpress ORs. The OR gene was

transformed into *E. coli* and incubated in 100 μg/mL ampicillin and 40 μg/mL chloramphenicol agar plates for 16 h at 37°C. A single colony was inoculated into 5 mL LB medium containing antibiotics (100 μg/mL ampicillin and 40 μg/mL chloramphenicol) and incubated for 16 h at 37°C. The bacterial cells were inoculated into 1 L fresh LB medium and incubated until the OD600 value reached 0.3~0.5 at 30°C after 0.2% arabinose induction. The temperature was decreased to 25°C, and 0.1 mM IPTG was added to the medium to induce the expression of ORs. After incubating the medium for 16 h at 25°C, the cells were harvested by centrifugation (4°C, 7000 g, 15 min) and resuspended in PBS buffer containing 2 mM EDTA (pH 7.4). The insoluble fraction of cell lysates was obtained by sonication (5 s on/off, 38% amplitude, 5 min) and centrifugation (4°C, 12000 g, 30 min). The insoluble fraction was solubilized with solubilization buffer (0.1 M Tris-HCl, 20 mM SDS, 1 mM EDTA, 0.1 M DTT, pH 8.0) and incubated at 30°C overnight. The solubilized proteins were obtained by centrifugation (20°C, 12 000 g, 30 min) and dialyzed by dialysis membrane tubing (MEMBRA-CEL®, 14 kDa cutoff) with binding buffer (0.1 M sodium phosphate, 10 mM SDS, pH 8.0). The OR was purified by HisTrap™ HP column (GE Healthcare) using washing buffer (0.1 M sodium phosphate, 10 mM SDS, pH 7.0) and elution buffer (0.1 M sodium phosphate, 10 mM SDS, pH 6.0). We exchanged the buffer of the purified OR with HEPES buffer I (20 mM HEPES, 100 mM NaCl, 25 mM cholate, pH 8.0) by HiTrap™ Desalting column (GE Healthcare) for assembly of NDs.

3.3.2 Expression of membrane scaffold protein in *E. coli*

The membrane scaffold protein gene (pMSP1E3D1 (Addgene)) was transformed into *E. coli* and incubated in 50 µg/mL kanamycin agar plates for 16 h at 37°C. A single colony was inoculated into 5 mL LB medium containing antibiotics (50 µg/mL kanamycin) and incubated for 16 h at 37°C. The bacterial cells were inoculated into 1 L fresh LB medium and incubated until the OD600 value reached 0.5 at 37°C. Expression of MSP1E3D1 was induced by 1 mM IPTG and the cells were incubated for 4 h at 37°C. The cells were harvested by centrifugation (4°C, 7000 g, 15 min) and resuspended in binding buffer (20 mM Tris-HCl, 0.5 M NaCl, 20 mM imidazole pH 8.0). The supernatant of cell lysates was obtained by sonication (5 s on/off, 38% amplitude, 5 min) and centrifugation (4°C, 12000 g, 30 min). The supernatant was applied to a HisTrap™ HP column (GE Healthcare) and purified by using washing buffer (20 mM Tris-HCl, 0.5 M NaCl, 50 mM imidazole pH 8.0) and elution buffer (20 mM Tris-HCl, 0.5 M NaCl, 350 mM imidazole pH 8.0). The buffer of purified MSP1E3D1 was exchanged with HEPES buffer II (20 mM HEPES, 100 mM NaCl, pH 8.0) by a HiTrap™ Desalting column (GE Healthcare) for assembly of NDs. To cleave off the histidine tag of MSP1E3D1, purified MSP1E3D1 was incubated with TEV protease at a molar ratio of 1:100 for 16 h at 4°C. Truncated MSP1E3D1 was obtained from the flow-through of a HisTrap™ HP column.

3.3.3 Expression of olfactory receptors in HEK-293T cell

HEK-293 cells were cultured in Dulbecco's Modified Eagles Medium (DMEM) (HyClone, USA) supplemented with 1 % penicillin, 1% streptomycin (Gibco, USA) and 10% Fetal Bovine Serum (FBS) (Gibco, USA) at 37 °C under 5% CO2. The transfection was performed with Lipofectamine3000 (Invitrogen, USA) following the manufacturer's protocol. The cells were transfected with Liopofectamine3000 DNA mixture containing GPCR, pCRE-Luc, pSV40-RL, Gαolf and RTP1S. The cells were harvested with PBS (pH 7.4) and then disrupted by sonication (2 s on/off, 2 min) (Sonics Vibracell, USA).

3.4 Purification

3.4.1 Purification of olfactory receptors

The Rosetta™ 2 (DE3) *E. coli* strain (Merck) was used for production of all proteins. SuptoxD and SuptoxR which coexpress DjlA and RraA, respectively, were used to overexpress ORs. The OR gene was transformed into *E. coli* and incubated in 100 μg/mL ampicillin and 40 μg/mL chloramphenicol agar plates for 16 h at 37°C. A single colony was inoculated into 5 mL LB medium containing antibiotics (100 μg/mL ampicillin and 40 μg/mL chloramphenicol) and incubated for 16 h at 37°C. The bacterial cells were inoculated into 1 L fresh LB medium and incubated until the OD_{600} value reached 0.3~0.5 at 30°C after 0.2%

arabinose induction. The temperature was decreased to 25°C, and 0.1 mM IPTG was added to the medium to induce the expression of ORs. After incubating the medium for 16 h at 25°C, the cells were harvested by centrifugation (4°C, 7000 g, 15 min) and resuspended in PBS buffer containing 2 mM EDTA (pH 7.4). The insoluble fraction of cell lysates was obtained by sonication (5 s on/off, 38% amplitude, 5 min) and centrifugation (4°C, 12000 g, 30 min). The insoluble fraction was solubilized with solubilization buffer (0.1 M Tris-HCl, 20 mM SDS, 1 mM EDTA, 0.1 M DTT, pH 8.0) and incubated at 30°C overnight. The solubilized proteins were obtained by centrifugation (20°C, 12 000 g, 30 min) and dialyzed by dialysis membrane tubing (MEMBRA-CEL®, 14 kDa cutoff) with binding buffer (0.1 M sodium phosphate, 10 mM SDS, pH 8.0). The OR was purified by HisTrap™ HP column (GE Healthcare) using washing buffer (0.1 M sodium phosphate, 10 mM SDS, pH 7.0) and elution buffer (0.1 M sodium phosphate, 10 mM SDS, pH 6.0). We exchanged the buffer of the purified OR with HEPES buffer I (20 mM HEPES, 100 mM NaCl, 25 mM cholate, pH 8.0) by HiTrap™ Desalting column (GE Healthcare) for assembly of NDs.

3.4.2 Purification of membrane scaffold protein

The membrane scaffold protein gene (pMSP1E3D1 (Addgene)) was transformed into *E. coli* and incubated in 50 μg/mL kanamycin agar plates for 16 h at 37°C. A single colony was inoculated into 5 mL LB medium containing antibiotics (50 μg/mL kanamycin) and incubated for

16 h at 37°C. The bacterial cells were inoculated into 1 L fresh LB medium and incubated until the OD_{600} value reached 0.5 at 37°C. Expression of MSP1E3D1 was induced by 1 mM IPTG and the cells were incubated for 4 h at 37°C. The cells were harvested by centrifugation (4°C, 7000 g, 15 min) and resuspended in binding buffer (20 mM Tris-HCl, 0.5 M NaCl, 20 mM imidazole pH 8.0). The supernatant of cell lysates was obtained by sonication (5 s on/off, 38% amplitude, 5 min) and centrifugation (4°C, 12000 g, 30 min). The supernatant was applied to a HisTrap™ HP column (GE Healthcare) and purified by using washing buffer (20 mM Tris-HCl, 0.5 M NaCl, 50 mM imidazole pH 8.0) and elution buffer (20 mM Tris-HCl, 0.5 M NaCl, 350 mM imidazole pH 8.0). The buffer of purified MSP1E3D1 was exchanged with HEPES buffer II (20 mM HEPES, 100 mM NaCl, pH 8.0) by a HiTrap™ Desalting column (GE Healthcare) for assembly of NDs. To cleave off the histidine tag of MSP1E3D1, purified MSP1E3D1 was incubated with TEV protease at a molar ratio of 1:100 for 16 h at 4°C. Truncated MSP1E3D1 was obtained from the flow-through of a HisTrap™ HP column.

3.5 Functional reconstitution of olfactory receptors

3.5.1 Nanodisc

DMPC (20mM) in HEPES buffer (20 mM HEPES, 100 mM NaCl, 50

mM cholate, pH 8.0) was used for assembly of OR-embedded NDs. MSP1E3D1 was added to the DMPC solution at a 1:150 molar ratio, and the mixture was incubated for 10 min at 24°C. The OR in HEPES buffer I was added to the mixture, and the mixture was incubated for 2 h at 24°C. The final molar ratio of OR, MSP1E3D1 and DMPC was 1:5:750. To remove cholate, 0.5 g Bio-Beads (Bio-Rad)/mL of mixture assembly was added to the mixture, and the mixture was incubated for 16 h at 24°C. To remove empty NDs, the mixture was applied to a HisTrap™ HP column and purified by HEPES elution buffer (20 mM HEPES, 100 mM NaCl, 350 mM imidazole pH 8.0). SEC (Superdex 200 Increase 10/300 GL, GE Healthcare) was used to purify OR-embedded NDs with optimal size.

3.5.2 Detergent micelle

Purified hOR1A2 was dialyzed with Tris buffer I (0.1 M Tris-HCl, 10 mM SDS, 0.5 mM EDTA, pH 8.0) and same step was repeated with Tris buffer II (0.1 M Tris-HCl, 3 mM SDS, 0.5 mM EDTA, pH 8.0). 1 mM GSSG, 6 mM GSH, 6 mM DDM, 6 mM Cymal-6 and 6 mM methyl-β-cyclodextrin were added for refolding the structure of hOR1A2. The solution was stored at -20 °C for 24 h and thawed at -4 °C gradually. The refolded hOR1A2 was obtained by dialysis using refolding buffer (0.1 M Tris-HCl, 0.3 M NaCl, 1 mM DDM, 1 mM Cymal-6, 1 mM EDTA, pH 7.4).

3.5.3 Polydiacetylene/Lipid nanovesicle

The fabrication method of the PDA vesicles was similar to that in earlier researches[109]. Briefly, the diacetylene monomer TCDA and DMPC powders (7:3 mole ratio) were dissolved in chloroform (Sigma-Aldrich) and dried together in vacuum. Then, deionized (D.I.) water was added, and probe sonication (Model 550 Sonic Dismembrator, Fisher Scientific) was performed for 15 min at approximately 70°C. The vesicle solutions were filtered through 0.22 μm filters (JetBiofil), and then cooled and maintained at 4°C overnight. The 1 mM PDA vesicle solution and 200 μg mL^{-1} hOR1A2 (3:1 volume ratio) were incubated at 30°C and 400 rpm for 45 min (Mixing Block MB-102, BIOER), and then, the solution was centrifuged at 4°C and 12000 rpm for 30 min to remove the free hOR from the PDA/hOR complex solution. Polymerization was carried out by 30 s irradiation at 254 nm (2 mW/cm^2). The PDA/lipid/hOR assembly prepared using the diacetylene monomer TCDA and DMPC powders (6:4 mole ratio) did not interact with the target geraniol 1 mM.

3.6 Characterization
3.6.1 Nano-glo dual luciferase assay

Nano-glo dual luciferase reporter assay (Promega) was applied for characterization of TAAR13c and TAAR13d receptors. We used *firefly* luciferase as a reporter to measure the response of ORs and NanoLuc®

luciferase for constitutively expressed control reporter. A total of 1.5×10^4 HEK-293T cells were transferred into 96-well plates and cultured in DMEM (HyClon) containing 1% penicillin, 1% streptomycin (Gibco), and 10% FBS (Gibco) at 37°C under 5% CO_2. After 24 h, ORs and other accessory proteins were transfected at a fixed ratio (pCRE-luc:pNL:M3R:RTP1S:Ric8b:$G_{\alpha olf}$:OR) = 2:1:2:2:1:1:10) with Lipofectamine 3000 (Invitrogen). After transfection, the medium was replaced with 50 μL CD293 with 1XGlutaMAX™ (Gibco) and the plates were incubated for 30 min at 37°C. The plates were incubated for 4 h at 37°C after odorant stimulation. The luminescence was measured by Spark™ 10M multimode microplate reader (TECAN). The normalized luciferase activity was calculated with the formula [CRE/NL(N) − CRE/NL(0)]/[CRE/NL(FSK)-CRE/NL(0)]. Forskolin (FSK)-treated cells (10 μM) were used as a positive control and odorant-untreated cells (0) were used as a negative control.

3.6.2 SDS-PAGE analysis

An acrylamide gel loaded with purified protein or ND samples was incubated with Coomassie Blue staining solution (Coomassie Blue 0.5 g/L, acetic acid 7% (v/v), methanol 40% (v/v)) for 1 h at room temperature. The gel was destained by destaining solution I (acetic acid 7% (v/v), methanol 40% (v/v)) for 1 h at room temperature and destaining solution II (acetic acid 7% (v/v), methanol 5% (v/v)) overnight at room temperature. Anti-V5 epitope tag mouse antibody

(Santa Cruz Biotechnology) was used as a primary antibody for detecting ORs and HRP-conjugated anti-mouse antibody (Merck) was used as a secondary antibody in Western blot analysis.

3.6.3 Dynamic light scattering

The size of the NDs was analyzed by a DLS spectrophotometer (DLS-7000). The measurement conditions for DLS were as follows; temperature (25°C), refractive index (1.3315), and viscosity (0.891). Field-emission scanning electronic microscopy (AURIGA, Carl Zeiss) was used to analyze the size analysis of olfactory-receptor-embedded NDs and their shape.

3.6.4 Circular dichroism

The secondary structure of hOR1A2 embedded in the PDA samples was analyzed using a CD spectrometer (ChirascanTM-Plus CD Spectrometer, Applied Photophysics) at wavelengths between 190 and 260 nm.

3.6.5 Tryptophan fluorescence quenching assay

The functionality of OR-embedded NDs was analyzed by means of a tryptophan fluorescence quenching assay using a luminescence spectrometer (LS 55 Luminescence Spectrometer, PerkinElmer). We excited the NDs at 290 nm and detected the emission at 350 nm. The normalized fluorescence intensity was calculated with the formula

$(\Delta F/F_0 \ (\%) = [(F_0 - F)/F_0] \times 100 \ (\%))$. F_0 is fluorescence intensity of odorant-untreated NDs and F is fluorescence intensity of odorant-treated NDs.

3.7 Immobilization of olfactory receptor-embedded nanodisc on graphene

For analyzing the shape of OR-embedded NDs by scanning electron microscope (SEM), 1 mM 1-pyrenebutyric acid N-hydroxysuccinimide ester (PSE) 10 μL in methanol was loaded on graphene for 1 hour. Graphene was washed with methanol for 2-3 times to remove remain PSE. The methanol was evaporated by flushing nitrogen gas until no solvent on the graphene. 10 μL, 1 μM olfactory-receptor embedded nanodics were treated on the graphene and incubated for 4 hours at room temperature. The remain NDs were washed out with 20 μL 20 mM HEPES buffer for 2-3 times. 33%, 66%, 99% and 100% ethanol were treated respectively for 10 minutes to dehydration of graphene. The graphene was incubated for 1 hour at -80°C deep freezer. Finally, the graphene was lyophilized for overnight.

For immobilization of the TAAR13 NDs on BE-nose, 10 μL 20 μM the interfacial chemical bis(2-aminoethylene)perylene-3,4,9,10-tetracarboxyldiimide (PDA) was dropped on the graphene micropattern (GM) and reacted for 1 hour at room temperature. The PDA-

immobilized GM was treated with 10 μL 2% glutaraldehyde (GA) over 4 hours at 4°C and washed using PBS solution and DW. Finally, 10 μL 1 μM TAAR13 NDs was treated on GA/PDA-immobilized GM over 12 hours at 4°C and then cleaned using PBS solution and DW.

Chapter 4

Enhancement of olfactory receptor production in *E. coli* system and characterization of olfactory receptor-embedded nanodiscs

4.1 Introduction

GPCRs are very hard to be overexpressed in *E. coli* systems because of hydrophobicity of their complex structure, seven transmembrane protein. There are three main reasons for GPCRs production in *E. coli* system: (1) there is usually very low level of membrane-incorporated GPCRs per cell, (2) when the amount of GPCRs in the cell membrane are accumulated with substantial level, there is typically a very low amount of GPCRs that is produced in a well-folded and functional structure, and (3) significant levels of toxicity for the host are typically associated with overexpression[14,15].

Despite these clear limitations, there have been some reports of GPCRs expressed successfully in *E. coli*[16–18]. Unmodified GPCRs tend to be expressed as inclusion bodies and may aggregate in such systems[16]. The use of fusion partners or tags is a key strategy for effective expression and well-folding of GPCRs in the *E. coli* system[19]. These aid in both expression and purification by directing the precise insertion of GPCRs into the membrane and enhancing its overall solubility[20]. Furthermore, some approaches such as selective mutagenesis to generate mutations and the use of insertion or truncation have been shown to be effective in some researches[16,21]. Indeed, *E. coli* genetic alteration can be utilized to select for variations with higher stability and expression, even for somewhat difficult to manage receptors[22,23].

In recent studies, development of *E. coli* strains for suppressing membrane protein-induced toxicity and obtaining high-level recombinant membrane protein[106–108]. The *E. coli* strains co-expressing DjlA, the membrane-bound DnaK cochaperone and RraA, the inhibitor of the mRNA-degrading activity of the *E. coli* RNase E, showed high productivity of GPCRs such as cannabinoid receptor, neurotensin receptor, neurokinin receptor and bradykinin receptor which are belong to class A GPCR.

In the form of reconstitution, NDs have a high stability, comparable to other reconstituted proteins[66]. The ND is composed of phospholipids that mimic the native environment of cell membrane and MSP that encircle the hydrophobic region of the phospholipid bilayer for stable structure of the receptor. The ND is the most promising biomaterial in the nanobiosensor field.

In this chapter, OR was overexpressed by co-expressing effector genes, such as *djlA*, the membrane-bound DnaK cochaperone, and *rraA*, inhibitor of the mRNA-degrading activity of *E. coli* RNase E. The *E. coli* strains coexpressing DjlA or RraA suppressed protein-induced toxicity and overexpressed the ORs. By controlling the molar ratio of OR, membrane scaffold protein, and phospholipid, ND of appropriate size were made, and high-purity ND could be purified. OR-embedded NDs showed stability to various temperature and storage time.

4.2 Expression and purification of olfactory receptor in *E. coli* system

TAAR13c and TAAR13d were overexpressed in *E. coli* strains which co-express effector genes, *djlA* and *rraA* (**Figure 4.1**). We used the *E. coli* strains coexpressing either DjlA, a the membrane-bound DnaK cochaperone, or RraA, an inhibitor of the mRNA-degrading activity of *E. coli* RNase E, to suppress protein-induced toxicity and overexpress the ORs in a bacterial system[106–108]. The *E. coli* strain coexpressing DjlA was termed SuptoxD and the *E. coli* strain coexpressing RraA was termed SuptoxR. We collected samples during the purification of TAAR13c expressed in wild-type cells. SDS-PAGE analysis of the samples showed the high purity but low content of TAAR13c in the eluent lane (E) (**Figure 4.2**). The contents of TAAR13c and TAAR13d were increased in both SuptoxD and SuptoxR cells (**Figure 4.3**). SuptoxR cells expressing TAAR13c after 0.1 mM IPTG induction and SuptoxR cells expressing TAAR13d after 0.5 mM IPTG induction showed the highest productivity in the experimental group (**Figure 4.4**). The purified TAAR13c and TAAR13d overexpressed in SuptoxR were confirmed by SDS-PAGE analysis (**Figure 4.5**) and Western blot analysis (**Figure 4.6**). In the SuptoxR cells, the production of the ORs caused lower protein-induced toxicity to the host cell than that in SuptoxD cells.
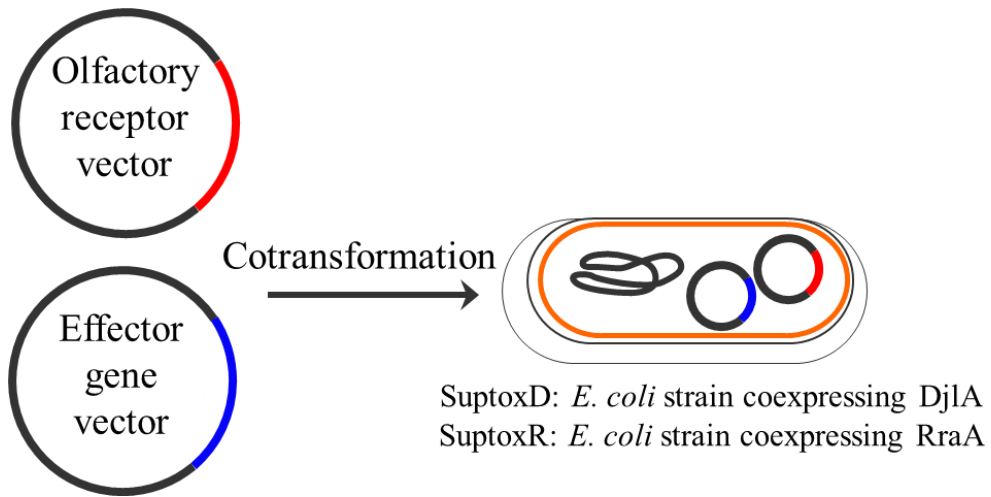
Figure 4.1 *E. coli* strains which co-express effector genes, *djlA* and *rraA*

P: Pellet after centrifugation
S: Supernatant after centrifugation
E: Eluent
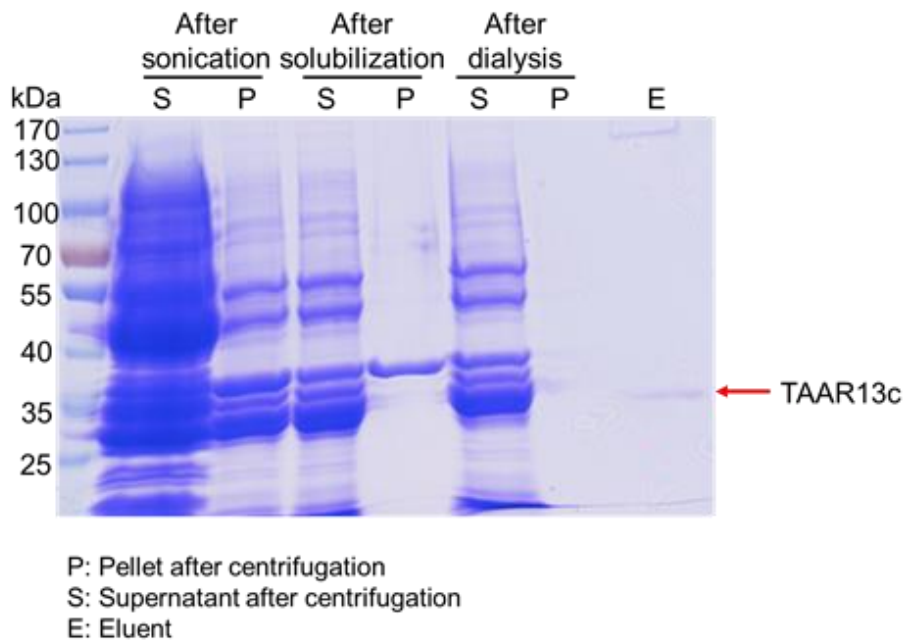
Figure 4.2 Productivity of olfactory receptors in wild-type *E. coli*

SuptoxD coexpressing DjlA; SuptoxR coexpressing RraA
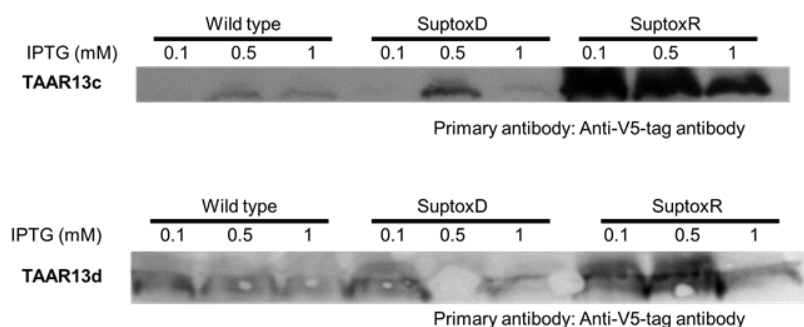
Figure 4.3 Western blot analysis for lysates of *E. coli* expressing TAAR13c (up) and TAAR13d (down)

SuptoxD coexpressing DjlA; SuptoxR coexpressing RraA
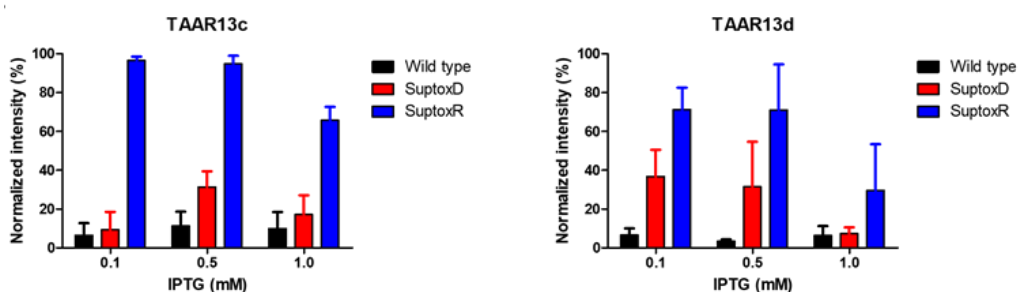
Figure 4.4 The relative Western blot signal intensities of Figure 4.3

SuptoxD coexpressing DjlA; SuptoxR coexpressing RraA. The error bars represent the standard error of the mean (n=3)
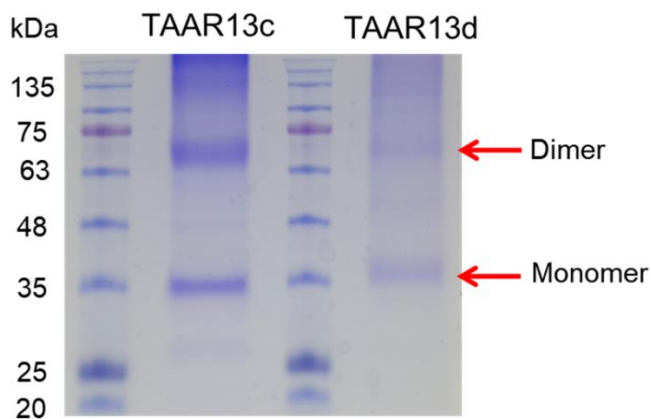
Figure 4.5 Coomassie blue staining analysis of purified TAAR13c and TAAR13d from *E. coli.*
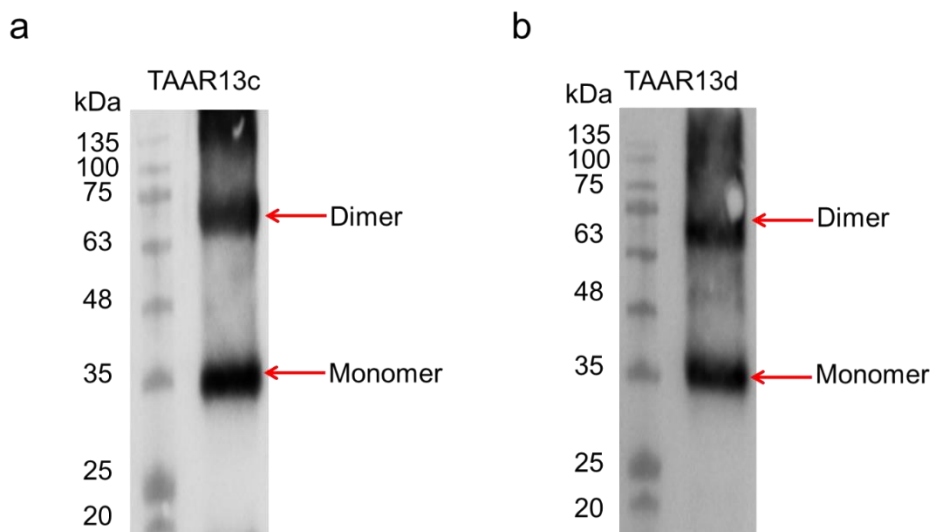
Figure 4.6 Western blot analysis of the purified TAAR13c (a) and TAAR13d (b) from *E. coli*

Anti-V5 tag antibody was primary antibody for detecting olfactory receptors.

4.3 Purification and size analysis of olfactory receptor-embedded nanodiscs

TAAR13 NDs were prepared using purified ORs, lipid bilayers, and MSPs via a facile self-assembly process described in our previous studies[53,110]. We optimized the size of the OR-embedded NDs in terms of the molar ratios of the ND components (**Table 4.1**)[111]. The optimal ratio of the OR, MSP1E3D1 and DMPC was 1:5:750. The absorbance peak of the OR-embedded NDs was observed at a retention volume of approximately 12 mL (**Figure 4.7**)[112]. The size distribution and homogeneity of the OR-embedded NDs were analyzed by DLS. The average diameters of TAAR13c NDs and TAAR13d NDs were 16.7 nm and 12.2 nm, respectively (**Figure 4.8**). The FE-SEM images clearly demonstrated that the shape of the OR-embedded NDs was a discoidal disc (**Figure 4.9**). These results clearly demonstrate that the NDs were successfully self-assembled in homogeneous discoidal shapes with proper size.

The composition of the ORs and MSP1E3D1 in the NDs was confirmed by SDS-PAGE analysis (**Figure 4.10**). The TAAR13c and TAAR13d bands were observed at approximately 38 kDa, and the MSP1E3D1 band was observed at approximately 30 kDa. The ORs within the TAAR13c and TAAR13d NDs were confirmed by Western blot analysis using an anti-V5 tag antibody (**Figure 4.11**).

Olfactory receptor (μM)	Membrane scaffold protein (μM)	DMPC (μM)	Average diameter (nm)
1	10	800	104.6
1	3	240	92.2
1	5	400	78.5
1	10	1500	24
1	3	450	60.8
1	5	750	16.7

Table 4.3 The molar ratio of OR, MSP and DMPC used to manufacture the nanodisc and average diameter of nanodisc
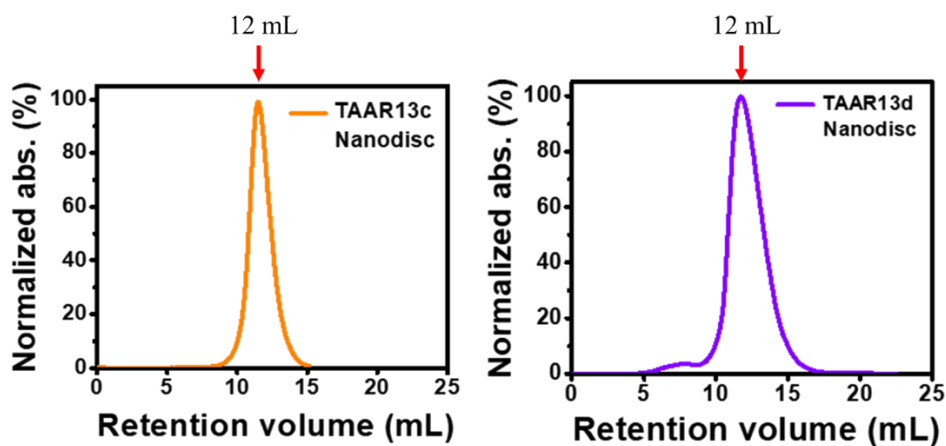
Figure 4.7 Size-exclusion chromatography profiles of TAAR13c ND and TAAR13d ND
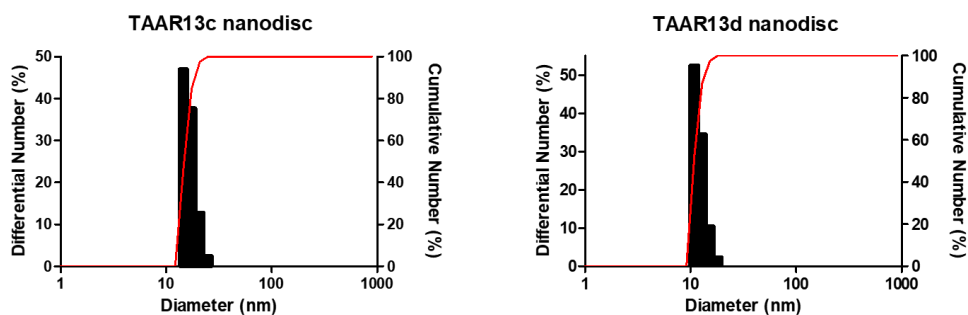
Average diameter = 16.7 nm   Average diameter = 12.2 nm

Figure 4.8 DLS profiles of TAAR13c ND and TAAR13d ND

74
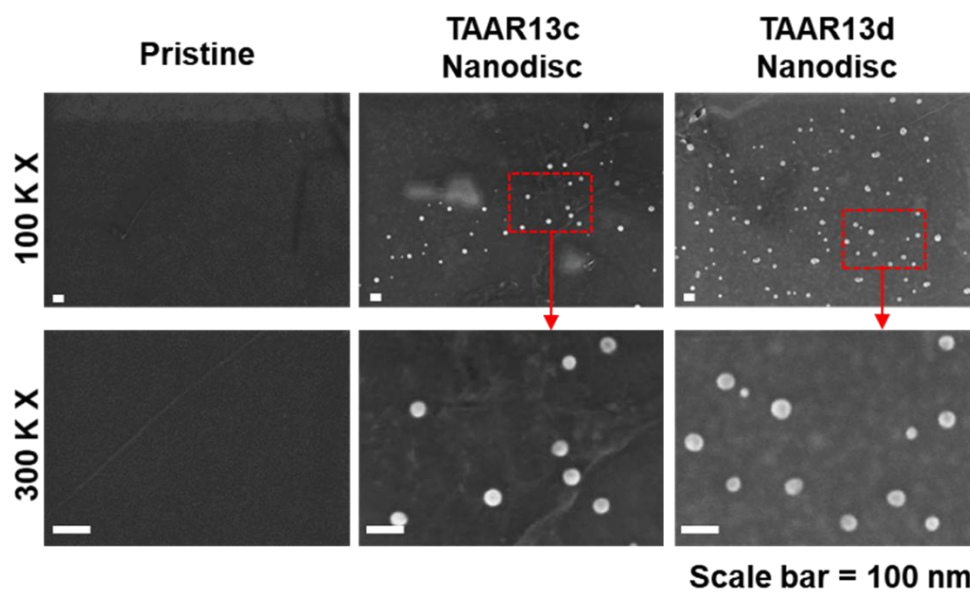
Figure 4.9 FE-SEM images of pristine graphene (left), TAAR13c ND (middle) and TAAR13d ND (right)
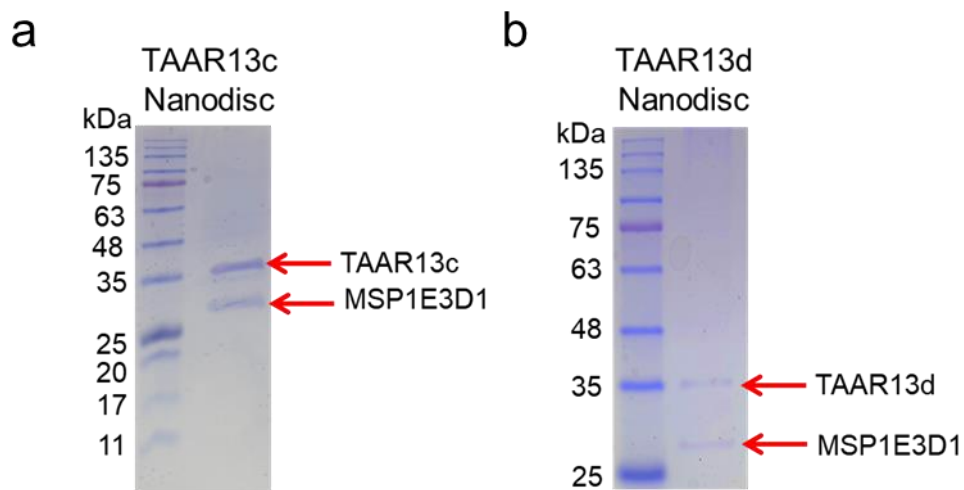
Figure 4.10 Coomassie blue staining analysis of purified (a) TAAR13c ND and (b) TAAR13d ND
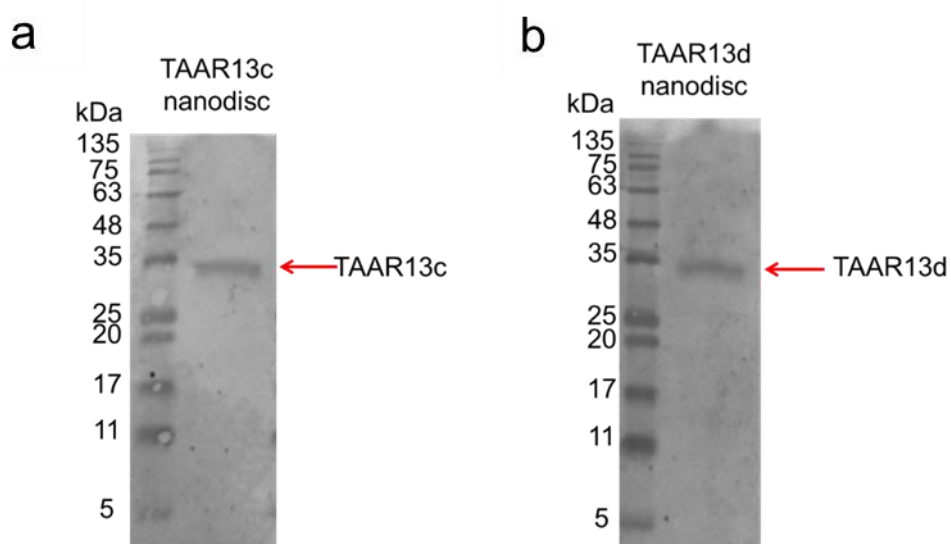
Figure 4.11 Western blot analysis of the purified TAAR13c nanodisc (a) and TAAR13d nanodisc (b).

Anti-V5 tag antibody was primary antibody for detecting olfactory receptors.

4.4 Stability of immobilized olfactory receptor-embedded nanodiscs

TAAR13c ND and hOR51E2 ND were immobilized on nickel-coated plate at 4°C for 16 hours and remain NDs were washed out with HEPES II buffer for 2-3 times. The immobilized NDs were eluted with HEPES elution buffer (20 mM HEPES, 100 mM NaCl, 350 mM imidazole, pH 8.0) at each incubation time and functionality of NDs were confirmed by tryptophan fluorescence quenching assay with target odorants (**Figure 4.12**).

Immobilized OR-embedded NDs maintained more than 80% functionality at 4°C for 16 weeks and 50% functionality at 37°C for 16 weeks (**Figure 4.13** and **Figure 4.15**). However, the functionality was drastically dropped to about 50% when olfactory-receptor embedded NDs were incubated at 37°C for 4 weeks. To determine the cause of the abrupt decrease, immobilized TAAR13c ND were incubated to 21 days at shorter intervals (**Figure 4.14**). Although, TAAR13c ND maintained 50% functionality until 21 days, the abrupt decrease of functionality was confirmed between 0 and 1 day. The functionality of hOR51E2 ND at 37°C showed same results of abrupt functionality decrease between 0 and 1 day (**Figure 4.15**). When the stability test was conducted at 37°C on a time scale, it was confirmed that the functionality of TAAR13c and hOR51E2 NDs decreased between 1 hour and 5 hours (**Figure 4.16**). After the NDs was immobilized at 4°C for 16 hours, the temperature

rapidly increased to 37°C, which affected the stability of the NDs, which seems to impair the functionality of the ORs.
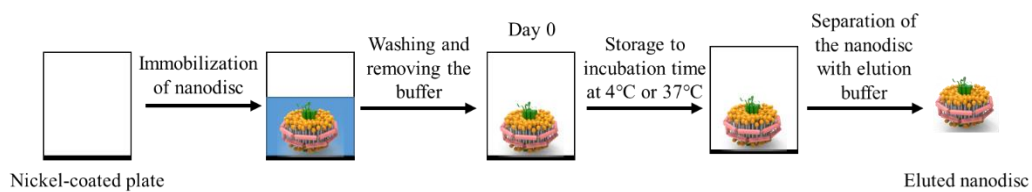
Figure 4.12 Schematic diagram for stability test of immobilized OR-embedded nanodisc
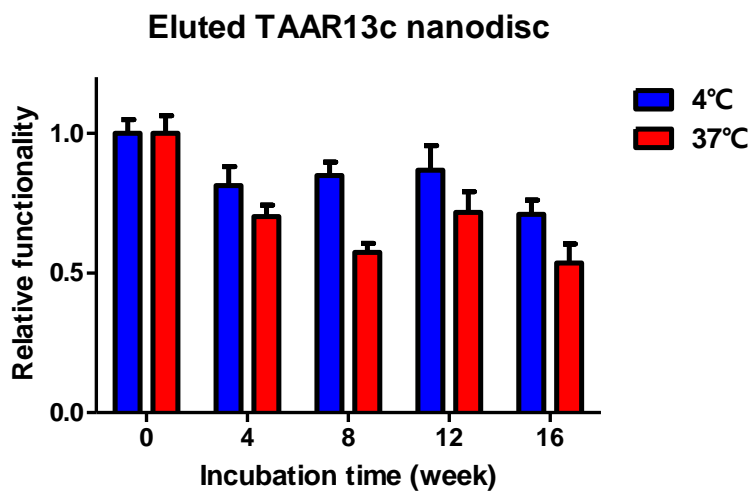
Figure 4.13 Stability test of immobilized TAAR13c nanodisc until 16 weeks at 4℃ and 37℃
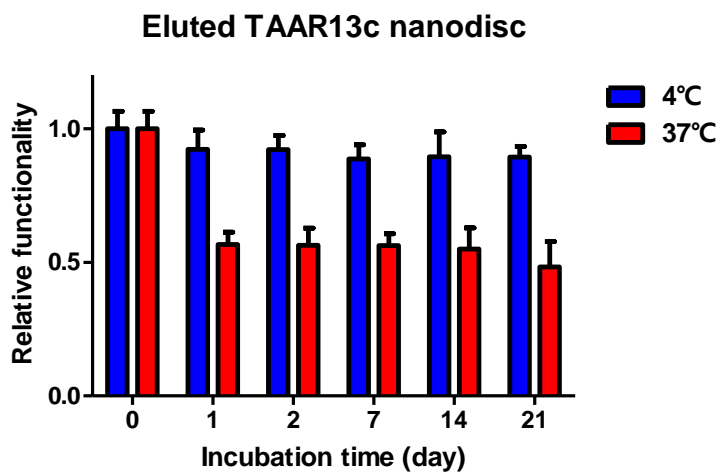
Figure 4.14 Stability test of immobilized TAAR13c nanodisc until 21 days at 4℃ and 37℃
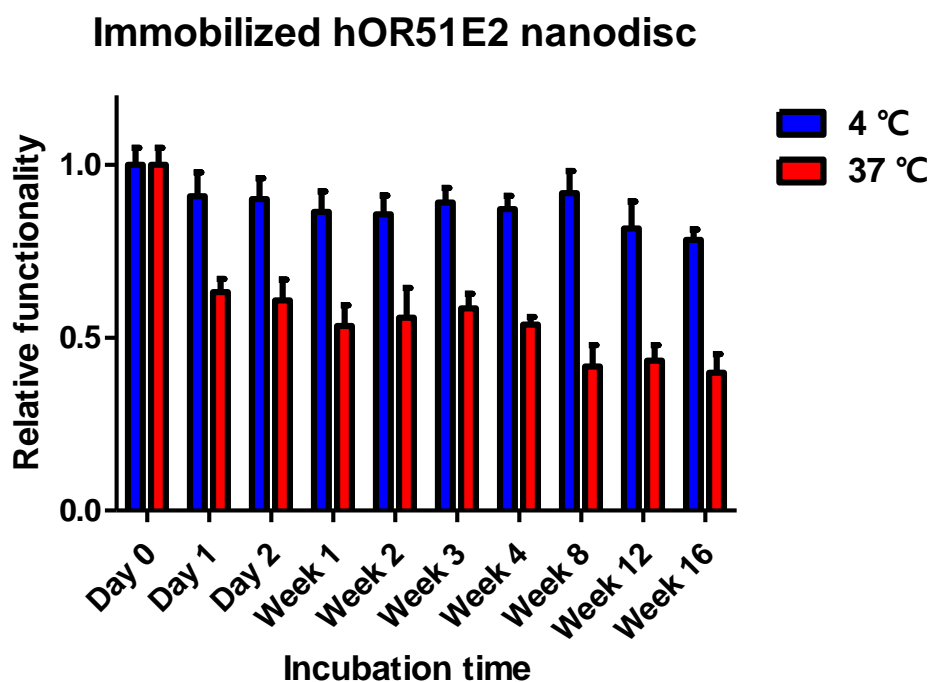
Figure 4.15 Stability test of immobilized hOR51E2 nanodisc until 16 weeks at 4℃ and 37℃

Odorant: 1mM cadaverine   Odorant: 1mM propionic acid
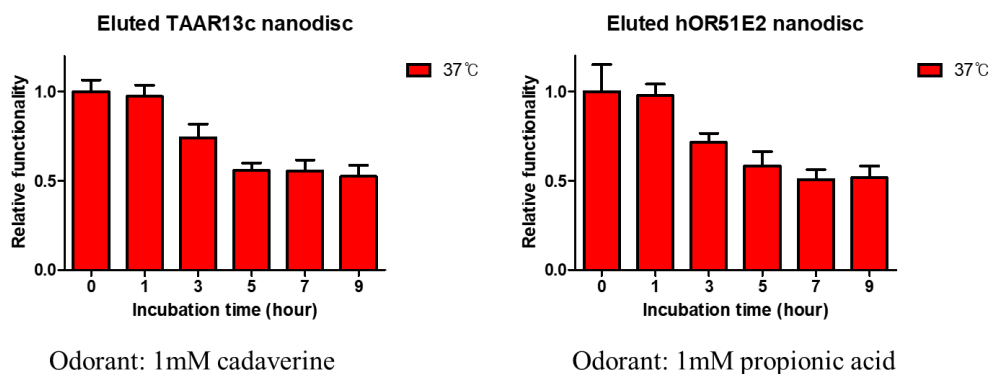
Figure 4.16 Stability test of immobilized TAAR13c and hOR51E2 nanodiscs until 9 hours at 37℃

4.5 Conclusions

SuptoxD and SuptoxR strains were used to suppress OR-induced cell toxicity and enhance productivity of ORs. As expected, SuptoxD and SuptoxR cells suppressed OR-induced toxicity and overexpressed the ORs in a *E. coli* system. In particular, when SuptoxR was induced with 0.1 mM IPTG, it showed 10 times higher protein productivity than wildtype.

By optimizing the molar ratio of ORs, DMPC, and MSP, ND with a proper size of less than 20 nm were assembled, and the OR-embedded NDs were purified with high purity.

In the stability experiment of the immobilized NDs, the functionality was maintained up to the 16 weeks at 4°C and 37°C after the first day. However, when the NDs immobilized at 4°C was incubated at 37°C, it was confirmed that the functionality of the NDs decreased due to a sudden temperature change. Nevertheless, when the immobilized OR-embedded ND reached the storage temperature, stability of the ND remained constant up to 16 weeks. In order to stably maintain the functionality of the immobilized ND, it is important to keep the immobilization temperature and storage temperature constant.

This study suggests an advanced method for mass-production of ORs in the *E. coli* system, and a method for high-purity purification of NDs with appropriate size and functionality. By showing that the

functionality of the NDs was maintained up to 16 weeks, it was confirmed that OR-embedded NDs are a promising biomaterial for the BE-nose.

Chapter 5

Development of nanodisc-based bioelectronic nose using trace amine-associated receptors for monitoring meat freshness/spoilage

5.1 Introduction

Food safety is a major concern in the worldwide, in both the food industry and the healthcare system[95]. In particular, among numerous information of the food products in both consumer and modern society, food spoilage is the main issue because of the critical negative effect on humans of food containing unsafe microorganisms[96]. For example, meat is a perishable food that usually deteriorates rapidly, within a few days[97]. Meat spoilage progresses in time via biochemical and physicochemical transformations[98]. In the biochemical spoilage process of meat, decarboxylation of amino acids by bacteria generates biogenic amines[100,113]. In addition, the amino acids in meat can be degraded into simple compounds such as NH_3 and H_2S by hydrolysis[98]. These biogenic amines and small chemical compounds produced by the deterioration of meat can be used as spoilage indicators. Targets indicating the freshness of food are normally complex mixtures; therefore, the development of monitoring tools offering multiplexed platforms for the detection of these spoilage indicators with high selectivity is required.

To date, various methods for CV and PT detection have been developed, such as cyclic voltammetry, resistance, colorimetry, polymerase chain reaction (PCR), fluorescence, GC/MS, LC/MS, SERS, chemiluminescence and FETs[114–121]. However, these techniques have limitations such as high cost, time-consuming, large instruments, low

sensitivity, and low selectivity. Although in our previous report, CV and PT were detected using SERS with-Au functionalized metal-organic frameworks (MOFs), which showed high performance, this technique still suffered from low repeatability, low reproducibility and non-specificity toward other biogenic amines because its mechanism is based on absorption[116]. Therefore, the development of a sensor platform for high-sensitivity and high-selectivity detection of CV and PT still remains challenging.

TAARs are GPCRs that recognize biogenic amines[122]. TAARs have been reported to function as vertebrate ORs. The kinds of TAARs vary between species, with 6 in humans (hTAARs), 15 in mice (mTAARs), 6 in macaques (macTAARs) and 112 in zebrafish (zTAARs)[123]. In particular, the TAAR13c and TAAR13d in zebrafish (*Danio rerio*) have been reported to selectively bind to death-associated odorants such as CV and PT[101,124,125]. CV and PT are biogenic amines that are produced by the microbial decarboxylation of amino acids[101]. CV and PT are formed by the decarboxylation of lysine and ornithine, respectively[100,113]. There have been reports that the mass of CV and PT increases with the incubation time of fresh meat, such as pork, beef, sausage, anchovy and tuna[100,102–104]. For this reason, CV and PT have been suggested as chemical indicators of meat spoilage, and monitoring the concentrations of the generated biogenic amines is important for determining food freshness and spoilage[105].

In this chapter, we developed TAAR ND-based BE-nose for monitoring meat freshness/spoilage. TAAR13c and TAAR13d, as ORs were utilized for specific recognition of the biogenic amines and were reconstituted with NDs to improve their functionality. The real-time responses of side-gated field-effect transistors (SG-FETs) toward various indicators showed high sensitivity and selectivity, and the LOD was 1 fM for CV and PT. In the gas sensor system, the LODs were 26.48 ppb for CV and 7.29 ppb for PT, indicating high performance. In addition, for the first time, a wireless portable TAAR13 NDs BE-nose integrated with commercial gas sensors allowed multiple monitoring of spoilage indicators from real food samples and showed high-performance and sensitivity. Our sensor system opens up the possibility of a portable TAAR13 NDs BE-nose system for on-site and in-situ freshness/spoilage monitoring.

5.2 Characterization of TAARs

It was reported that TAAR13c and TAAR13d, originating from zebrafish, interact specifically with CV and PT[101,124,125]. We confirmed their properties including their affinity and selectivity to CV and PT using luciferase reporter assay that has been widely applied for studying the function of GPCRs[42,126–128]. In this assay, HEK-293T cells expressing TAAR13c and TAAR13d responded to the death-associated odorants, CV and PT, respectively, in a dose-dependent manner (**Figure 5.1 (a)** and **(b)**). Additionally, we performed a selectivity test to confirm

that ORs specifically bind to the death-associated odorants. We chose different biogenic amines or amino acids containing monoamines or diamines (**Figure 5.2**). HEK-293T cells expressing TAAR13c responded to CV, and cells expressing TAAR13d responded to both CV and PT (**Figure 5.3**). A similar result in terms of the selectivity of TAAR13c and TAAR13d to these biogenic amines has been shown in a previous study[124].

To analyse the functionality and affinity of TAAR13 NDs for biogenic amines, a tryptophan fluorescence assay was carried out. It is known that the binding of functional receptors to selective ligands quenches the intrinsic fluorescence of the receptors[49,129,130]. The TAAR13c NDs and TAAR13d NDs exhibited dose-dependent responses to CV and PT, respectively, while the empty NDs did not bind to these death-associated odorants (**Figure 5.4**). TAAR13c NDs could detect CV with an EC_{50} of 370 nM and TAAR13d NDs could detect PT with an EC_{50} of 33 nM. The EC_{50} of these death-associated-odorants to the respective NDs indicated that the binding affinity of TAAR13d NDs to PT was approximately 10 times stronger than that of TAAR13c NDs to CV. these results are consistent with previous studies[101,124] and demonstrated that the TAAT13 NDs were prepared successfully and can be utilized as recognition elements in BE-noses for the efficient detection of biogenic amines.
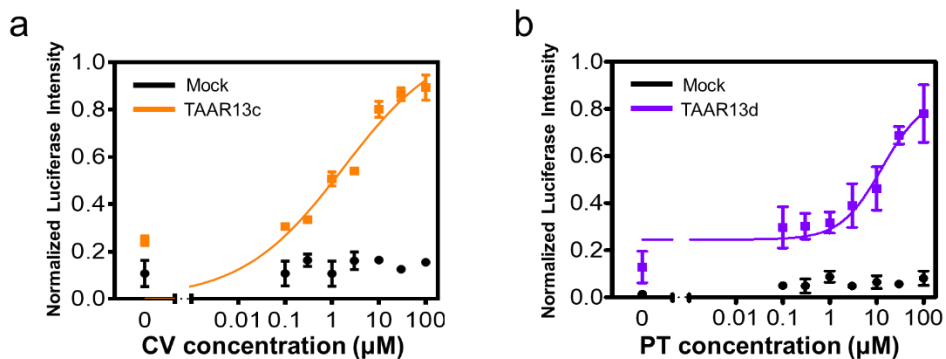
Figure 5.1 Dose-dependent responses of (a) TAAR13c to CV and (b) TAAR13d to PT
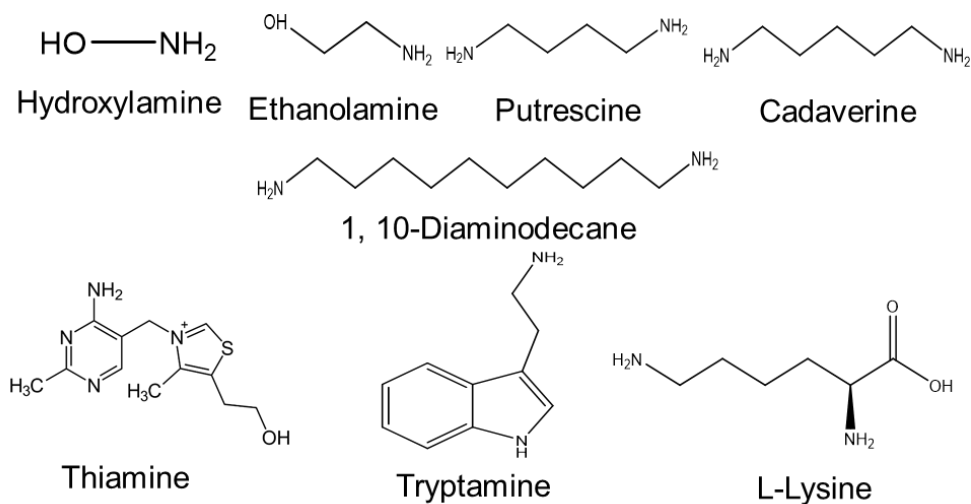
Figure 5.2 Chemical structures of various biogenic amines for the selectivity test
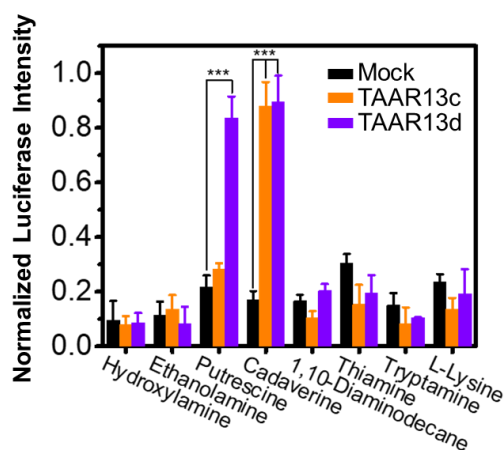
Figure 5.3 Selectivity test of TAAR13c and TAAR13d to various biogenic amines

The error bars represent the standard error of the mean (n=3, ***$P <$ 0.001).
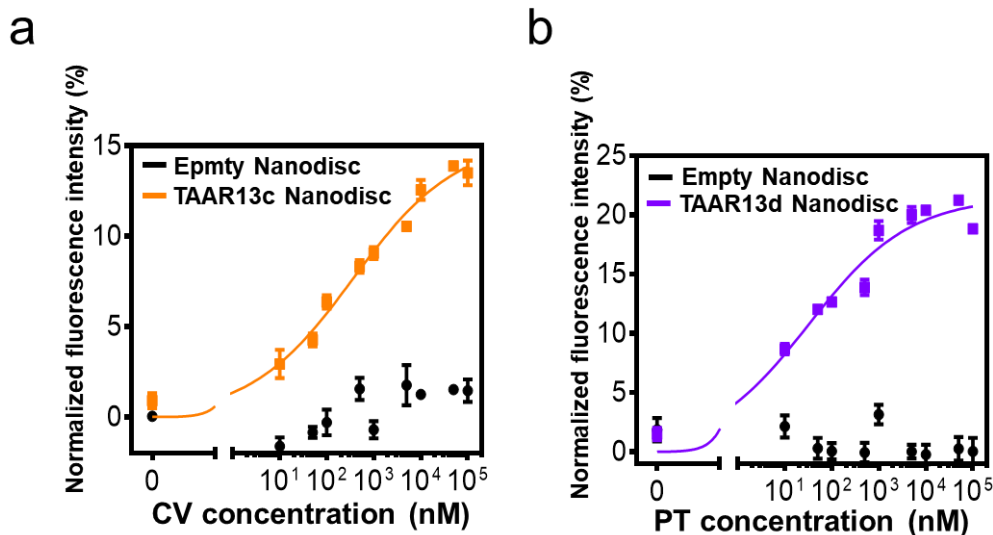
Figure 5.4 Tryptophan fluorescence quenching assay for dose-dependent responses of (a) TAAR13c ND to CV and (b) TAAR13d ND to PT

The error bars represent the standard error of the mean (n=3).

5.3 Performance of nanodisc-based bioelectronic nose in the liquid phase

The illustration in **Figure 5.5** indicates a dual-channel SG-FET, which is composed of a 3-ternary system of a side gate, a source, and drain electrodes to measure the electrical transport in real-time. In addition, the chamber was filled with a PBS (pH 7.4) solution as a dielectric material, which generated a field-effect by supplying voltage *via* the side-gate electrode.

To confirm the spoilage indicator detection performance of TAAR13 NDs-conjugated SG-FET platforms, dual GM channels were conjugated with TAAR13c ND and TAAR13d ND for CV and PT detection, respectively. The real-time responses were in terms of the concentrations of CV and PT, and the current change was normalized by the equation

$$\Delta I \,/\, I_0 = (I - I_0)/I_0 \tag{1}$$

where I and I_0 represent the instantaneous current changes after exposure to the target indicators and the initial current, respectively (**Figure 5.6 (a)** and **(b)**). Control experiments were carried out with empty NDs without receptors, such as TAAR13c or TAAR13d, to confirm the interaction between the receptors and the target indicators, which obviously showed no electrical signal (black line). **Figure 5.6 (a)** displays the real-time response of TAAR13c ND SG-FETs toward

various concentrations of CV ranging from 0.1 fM to 100 nM. Before monitoring the electrical signal toward CV, only buffer was injected to confirm the signal, and there was no current change. On the other hand, current changes were instantly observed upon CV injection, and the TAAR13c ND SG-FETs showed a linear range of 1 fM to 1 nM and excellent performance, with an LOD of 1 fM[110,131]. The TAAR13d ND SG-FET was monitored for detection toward various concentrations of PT in the range from 0.1 fM to 100 nM. Although buffer was injected to confirm the signal change, there was no current change. The TAAR13d ND SG-FETs exhibited a linear range from 1 fM to 100 pM and an LOD of 1 fM (**Figure 5.6 (b)**). The normalized sensitivities were determined by the current change level, and the concentration curves were obtained by normalizing the sensitivities depending on the concentration. The K constants were calculated by curve fitting based on Langmuir's adsorption isotherm equation (**Figure 5.7**)

$$N = C / (1 / K + C) \tag{2}$$

where N is the normalized sensitivity and C is the concentration of indicators[131–134]. The K values calculated based on the concentration curves were $2.616 \times 10^{12}\,\mathrm{M^{-1}}$ for the TAAR13c ND SG-FETs and $1.748 \times 10^{13}\,\mathrm{M^{-1}}$ for the TAAR13d ND SG-FETs. The TAAR13 NDs SG-FET system could detect CV and PT at various concentrations. To confirm the specific detection of the TAAR13 NDs, first, the TAAR13 ND SG-FETs were exposed to spoilage molecules such as (NH_3, H_2S, and PT or

CV (**Figure 5.8 (a)** and **(b)**). The TAAR13c ND SG-FETs clearly responded to CV at a concentration of 100 fM. However, no significant responses were observed toward NH_3, H_2S, or PT. The TAAR13c ND SG-FETs exhibited excellent sensitivity toward CV and showed no response for coexisting nontargets at concentrations 10^4 times higher than the CV concentrations (**Figure 5.8 (a)**). The TAAR13d ND SG-FETs showed a clear response toward 100 fM PT, as well as toward other death-associated odorants, such as trimethylamine (TMA) and NH_3. Although CV interacted with TAAR13d ND, the TAAR13d ND were 10^4 times more sensitivity PT than to CV (with a response at 1 nM). The interactions between TAAR13d ND and CV/PT are shown in **Figure 5.3** (**Figure 5.8 (b)**).

The storage stability of the TAAR13 NDs SG-FETs was evaluated for 30 days at 4°C with 10 pM aliquots of each target, and their current changes showed excellent environmental stability, which was maintained at over 95% as shown in **Figure 5.9**.
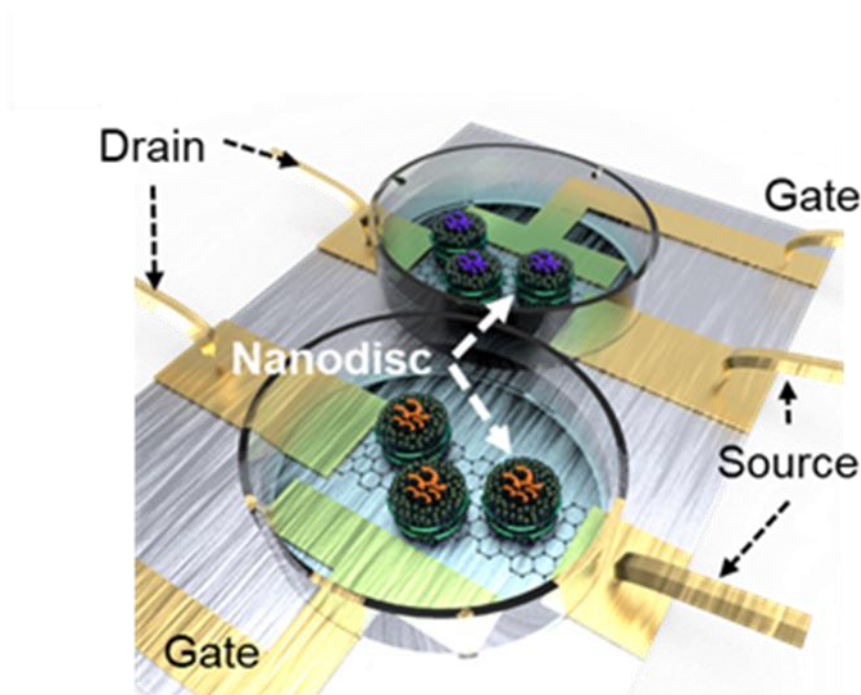
Figure 5.5 Schematic illustrations of the dual-channel liquid-ion-gated FET system for multidetection
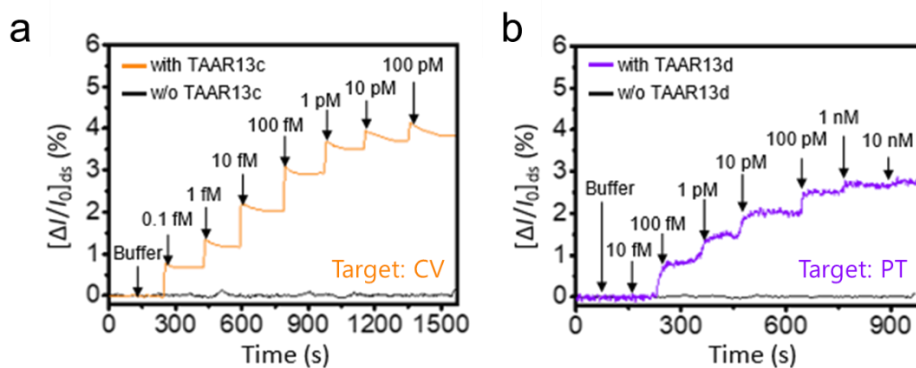
Figure 5.6 Real-time responses of TAAR13 NDs SG-FETs to various concentrations of (a) CV and (b) PT
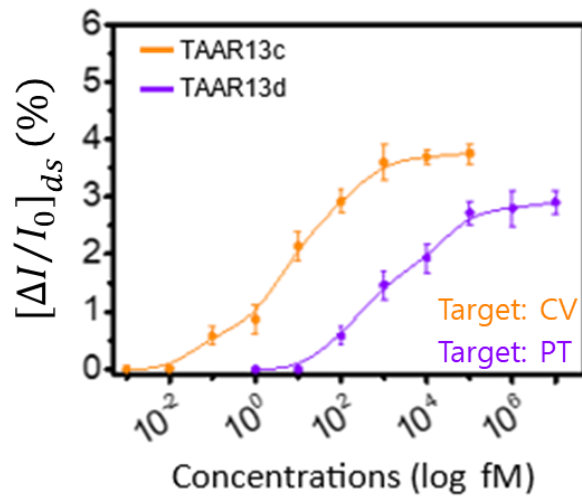
Figure 5.7 Calibration curves of the TAAR13 NDs SG-FET of CV (orange) and PT (violet)
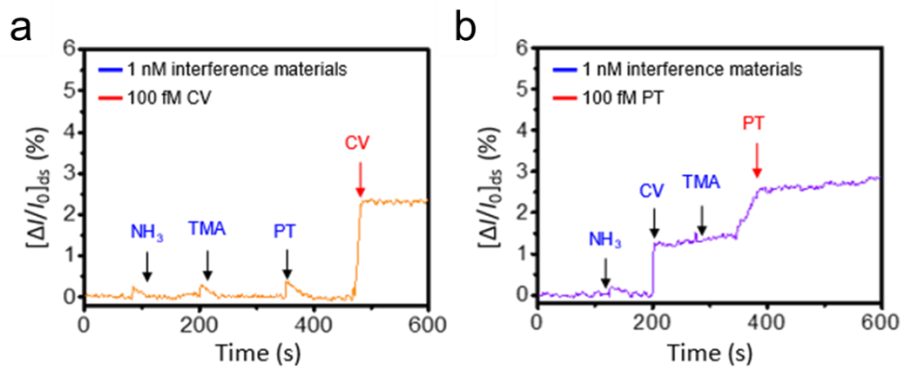
Figure 5.8 Specific test of TAAR13 NDs SG-FET toward (a) CV and (b) TAAR13d ND SG-FET for PT
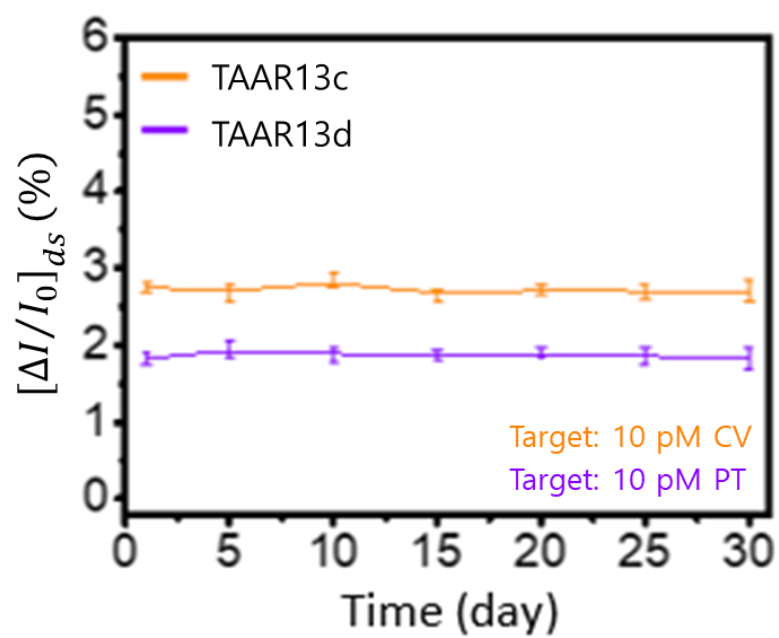
Figure 5.9 Long-term stability of each TAAR13 NDs SG-FET towards target indicators at 4℃

5.4 Gas sensing performance of bioelectronic nose and its application to meat spoilage

Real-time measurements were performed with the TAAR13 NDs BE-nose exposed periodically to CV gas (**Figure 5.10 (a)**). An abrupt resistance change was observed upon exposure to CV gas, which was proportional to the concentration, and the LOD was approximately 26.48 ppb. The NDs structure was exposed to environmental conditions for activation of the receptor in the dry state[110]. In addition, the CV gas from the NDs was detached by injection with N_2 gas thus, the resistance showed an instant change.

Figure 5.10 (b) shows the cross-reactivity of the TAAR13c ND BE-nose toward spoilage gases such as NH_3, H_2S and PT. No significant responses to similar concentrations of these other gases were observed. On the other hand, an obvious response to CV was observed. To confirm the performance of the TAAR13d ND BE-nose, the resistance change was measured after exposure to various concentrations of gases (**Figure 5.11 (a)**).

Finally, the selectivity of the TAAR13d ND BE-nose was determined by exposure to diverse spoilage gases, such as NH_3, H_2S and CV. However, the BE-nose was shown to respond specifically to CV and PT (**Figure 5.11 (b)**).
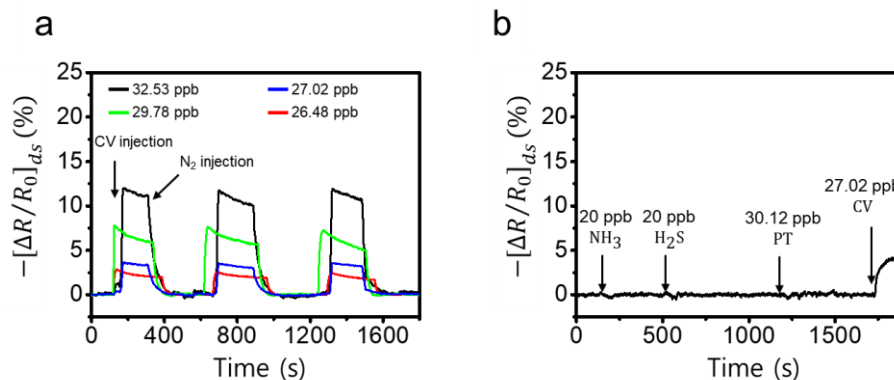
Figure 5.10 (a) Real-time responses of TAAR13c ND BE-nose upon cyclical exposure to CV concentrations of 26.48 to 32.527 ppb. (b) Specificity of the TAAR13c ND BE-nose
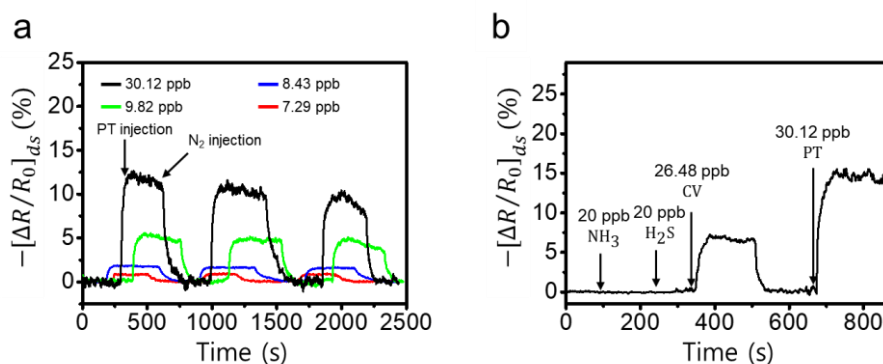
Figure 5.11 (a) Real-time responses of the TAAR13d ND BE-nose upon cyclical exposure to PT concentrations of 7.29 to 30.12 ppb. (b) Specificity of the TAAR13d ND BE-nose

5.5 Measurements of real samples using TAAR nanodisc-based bioelectronic nose

The resistance changes toward the indicators gradually increased with time; interestingly, CV and PT showed instantly increasing signals from 3 days. However, CV and PT showed no considerable signal changes after 4 days and 5 days, respectively (**Figure 5.12**).

The concentrations of CV and PT were analyzed by GC-FID for 6 days after collecting the real gas sample from the chamber in a Tedlar bag (**Figure 5.13**). The concentration changes for CV and PT were hardly observed, and the concentrations were 175 and 325 ppb, respectively, for two days. In addition, the changes of concentration gradually increased up to approximately 90 ppb, with the concentrations of CV and PT being raised to 260 and 400 ppb, respectively. The concentrations of CV and PT instantly increased after 4 days, whereas the portable TAAR13 NDs BE-nose could detect changes in CV and PT after 3 days (**Figure 5.12** and **Figure 5.13**).   To investigate the microbial content in meat, we incubated 25 g beef for 6 days at room temperature and performed a colony formation assay using Petrifilm™ (3M Science) (**Figure 5.14**). The number of *Enterobacteriaceae* in meat is proportional to the degree of spoilage and the quantity of CV and PT[135–137]. *Enterobacteriaceae* counts in beef increased until day 8, after which time, the microbial counts decreased during the spoilage period. Before incubating the beef under the experimental conditions (day 0),

the *Enterobacteriaceae* counts were 5.2 log (CFU)/mL, which is an acceptable level[138]. However, the counts exceeded the threshold levels of 7 log (CFU)/mL at day 1 and increased to 9 log (CFU)/mL at day 8 (**Figure 5.14**). These counts result in discoloration, strong off-odors and slime production of spoiled meat[139]. As the *Enterobacteriaceae* counts increased during the spoilage period, the quantities of CV and PT also showed an increasing trend and the portable TAAR13 NDs BE-nose showed a gradually increasing trend for resistance changes to CV and PT (**Figure 5.12**, **Figure 5.13** and **Figure 5.14**).

To investigate the concentration changes in the diverse samples, a portable TAAR13 NDs BE-nose was exposed to the collected gases from various real samples, such as pork, beef, chicken, sheep, and duck, in a chamber for 4 days at room temperature (**Figure 5.15 (a)**). We determined that the various real samples were in the spoilage stage by using the portable TAAR13 NDs BE-nose.   These results indicate that the portable TAAR13 NDs BE-nose can be utilized to monitor meat spoilage/freshness *via* the detection of CV and PT. In addition, to investigate the dependence of the sensitivity toward of CV and PT on the environment, a real sample was stored for 5 days at various temperatures, namely, 20°C, 4°C, 23°C, and 25°C (**Figure 5.15 (b)**). We determined that the real sample stored in the freezer (-20℃) remained fresh but the real samples stored in the refrigerator (4℃), laboratory (23℃) and restaurant (25℃) were in the spoilage state. Interestingly, a

decrease in resistance was observed with decreasing temperature due to deactivation of the decarboxylase activity of microorganisms[140].
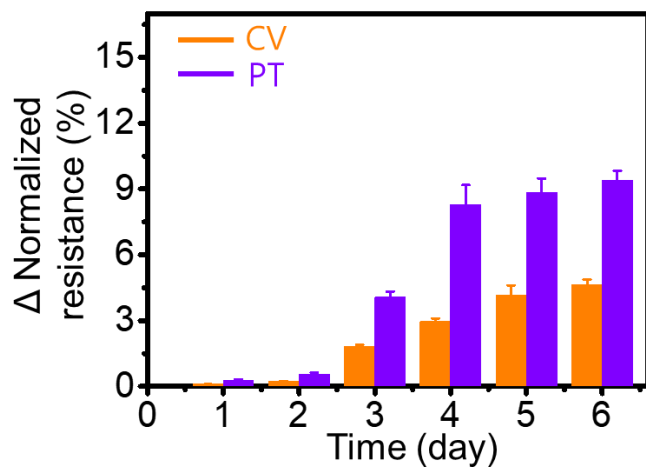
Figure 5.12 The measured sensitivity of the portable BE-nose for the gas collected from a real sample for 6 days
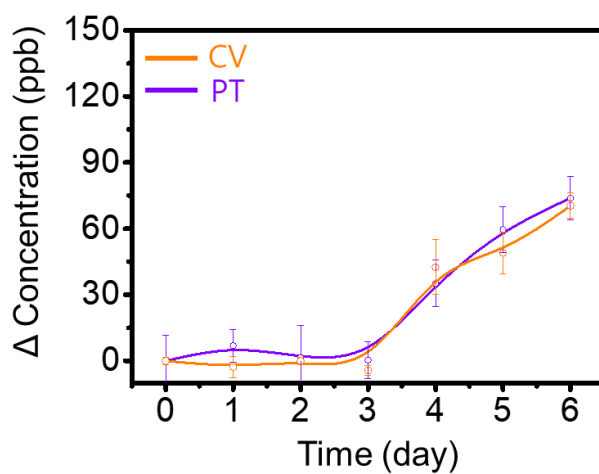
Figure 5.13 CV/PT GC-MS results in the real sample stored for 6 days
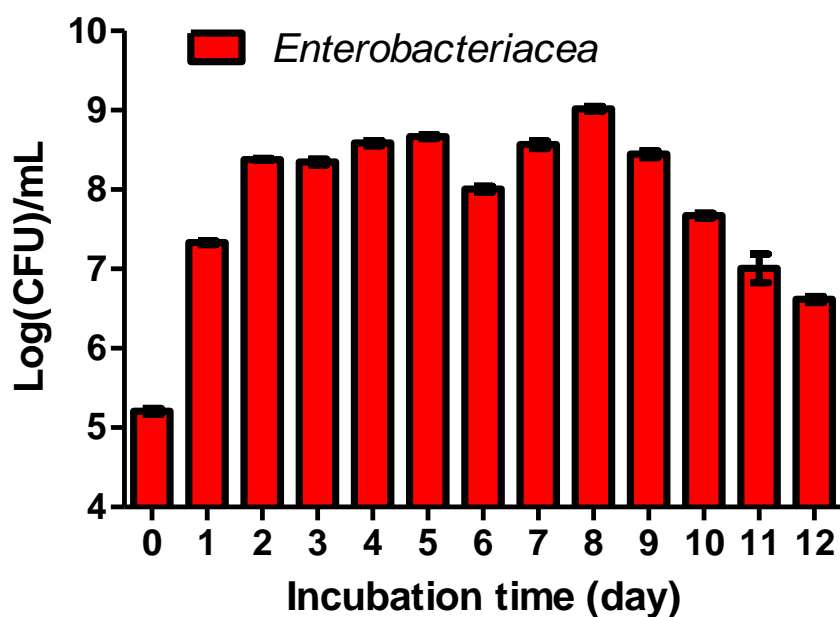
Figure 5.14 The number of *Enterobacteriaceae* in beef incubated for 12 days at room temperature
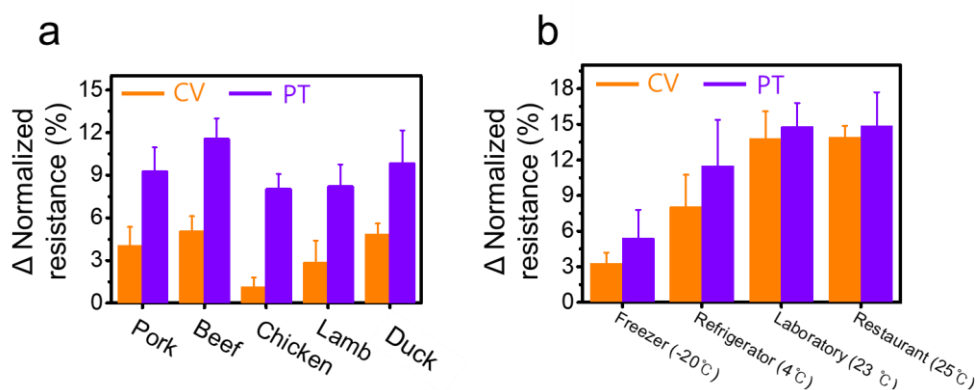
Figure 5.15 The measured sensitivity of portable BE-nose depending on the diverse (a) real samples stored at room temperature and (b) in various environments for 5 days.

5.6 Conclusions

In this study, a portable BE-nose demonstrated excellent sensitivity and selectivity toward various indicators and spoilage gases and was used to monitor the freshness and spoilage state over time. The TAAR13 family was used for the detection of CV and PT due to possible selective recognition and was fabricated in ND form to enhance its environmental stability. TAAR13 NDs SG-FETs showed excellent sensitivity, with LODs of 1 fM and 1 fM for CV and PT, respectively, and selectively responded to the various markers in the liquid state. The mechanisms and binding affinities were demonstrated by comparing the binding energies via biosimulations, and the binding of TAAR13d with PT showed higher affinity than that of TAAR13c with CV. The TAAR13 NDs BE-nose showed excellent LODs of 26.48 and 7.29 ppb for CV and PT, respectively, and displayed unprecedented detection ability for the spoilage indicators VOC and VBN. Based on these technologies, the TAAR13 NDs BE-nose was developed as a portable device, and was utilized for monitoring the freshness of various real samples in various environments. The responses toward the indicators in the real sample were also be detected in the fresh stage prior to spoilage. Finally, the portable TAAR13 NDs BE-nose platform was performed towards diverse on-site and the various real samples and was used to monitor the time of freshness. This BE-nose can potentially be utilized for the in situ and on-site monitoring of meat spoilage.

Chapter 6

Pattern analysis for gastric cancer biomarkers using human olfactory receptor-embedded nanodiscs

6.1 Introduction

Gastric cancer (cardia and noncardia gastric cancer combined) is the fifth most often diagnosed cancer and the third largest cause of cancer death, accounting for approximately 1,000,000 new cases in 2018 and an estimated 783,000 deaths (equating to 1 in every 12 deaths globally) (**Figure 2.7**)[78].

Helicobacter pylori is the leading cause of stomach cancer, accounting for about 90% of new occurrences of noncardia gastric cancer[79]. Although international diversity in *H. pylori* prevalence correlates reasonably with stomach cancer incidence, additional factors are likely to play a significant role. There is a nutritional component, with salt-preserved foods and a lack of fruits raising risk, and both alcohol drinking and active cigarette smoking are proven risk factors[80].

Although they are frequently presented as a single entity, gastric cancers can be divided into two topographical types. Noncardia gastric cancer rates (arising from more distant regions) have been steadily dropping in most populations over the previous half-century. The trends are related to success of prevention, such as a lower prevalence of *H. pylori* and breakthroughs in food preservation and storage[81]. Cancers of the gastric cardia (arising in the area adjacent to the esophageal-gastric junction) have epidemiological characteristics more similar to esophageal adenocarcinoma (AC), and important risk factors include obesity and

gastroesophageal reflux disease (GERD), with Barrett esophagus (a condition caused by GERD) also thought to increase risk; the incidence of these cancers has been increasing, particularly in high-income countries[78].

Many researchers analysed breath from gastric cancer patients and found some VOCs regarded as gastric cancer biomarkers, such as fatty acids, phenol and aldehyde[82–85] (**Table 2.3**).

Previous research has found a link between short-chain fatty acids (SCFAs) and gastrointestinal cancer. Some SCFAs, such as acetic acid, butyric acid, and propionic acid, are known to be generated by colonic bacteria through anaerobic fermentation of dietary carbohydrates[86,87]. Butyric and propionic acids have also been shown to cause apoptosis in a gastric carcinoma cell line[88]. As a result, SCFA monitoring is anticipated to be critical for understanding the activity of cancer cells in the digestive tract. Furthermore, several studies propose that SCFAs act as potent indicators in the exhaled breath of stomach cancer patients. Cross-platform validation has confirmed that butyric acid, valeric acid, and hexanoic acid are biomarkers of gastrointestinal cancer in the breath[82,84,89,90].

In this chapter, human OR embedded-NDs, hOR51E1, hOR51E2 and hOR52D1, were used for patterns of short-chain fatty acids. Short-chain fatty acids, such as propionic, butyric and valeric acids, were reported as biomarkers for gastric cancer or halitosis. ND is a suitable platform

for reconstitution of hORs because of its stable structure for transmembrane proteins. There were no reports about patterns of odors using hOR-embedded NDs. Through tryptophan fluorescence quenching assay, the hOR-embedded NDs respectively had different EC_{50} values to short-chain fatty acids. Propionic acid had the lowest EC_{50} value when it bound with hOR51E1 ND, while butyric and valeric acid had the lowest EC_{50} value when it bound with hOR52D1 ND. The different binding affinity of hOR-embedded NDs to short-chain fatty acids caused different patterns or identities. Samples of healthy group and gastric cancer patients were prepared with artificial saliva dissolving short-chain fatty acids, and it was confirmed through principal component analysis that healthy group and gastric cancer patients could be distinguished through the hOR-embedded ND.

6.2 Affinities of human olfactory receptor-embedded nanodiscs to gastric cancer biomarkers

Tryptophan fluorescence quenching assay was performed using empty ND and OR-embedded NDs to confirm patterns of NDs for gastric cancer biomarkers. Empty ND did not react to all odorants. On the other hand, hOR-embedded NDs showed various patterns to the gastric cancer biomarker compared to buffer (**Figure 6.1**). It was confirmed that each gastric cancer biomarker could be distinguished using only three ORs.

To confirm binding affinity of OR-embedded NDs to each gastric cancer biomarkers, tryptophan fluorescence quenching signals were observed while odorants were treated from low to high concentrations (**Figure 6.2**). By fitting the experimental results to Hill's equation curve, each half maximal concentrations for odorants binding to OR-embedded NDs were obtained (**Table 6.1**). hOR51E1 ND which is broadly tuned OR bound with propionic, butyric, valeric and hexanoic acid. hOR51E2 ND which is narrowly tuned OR bound with propionic and butyric acid. hOR52D1 which is broadly tuned OR bound with propionic, butyric, valeric and hexanoic acid. hOR51E1 ND.
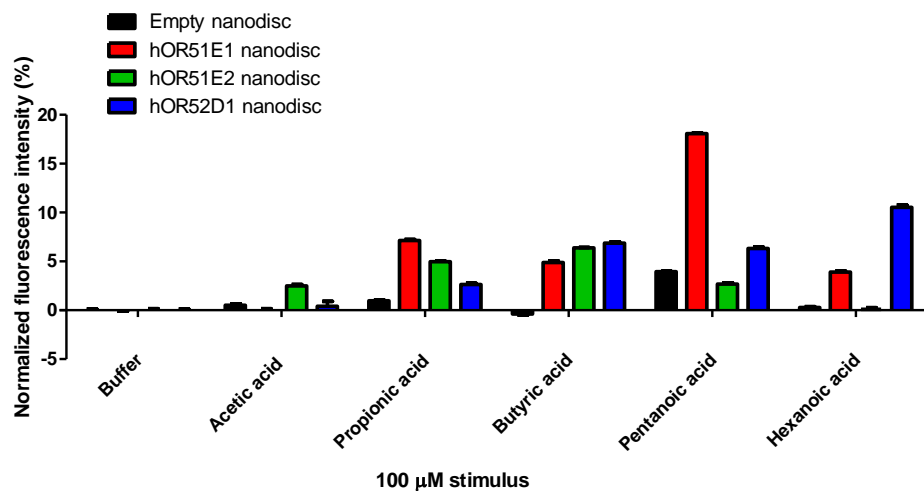
Figure 6.1 Tryptophan fluorescence quenching assay patterns of olfactory receptor responses to each gastric cancer biomarkers
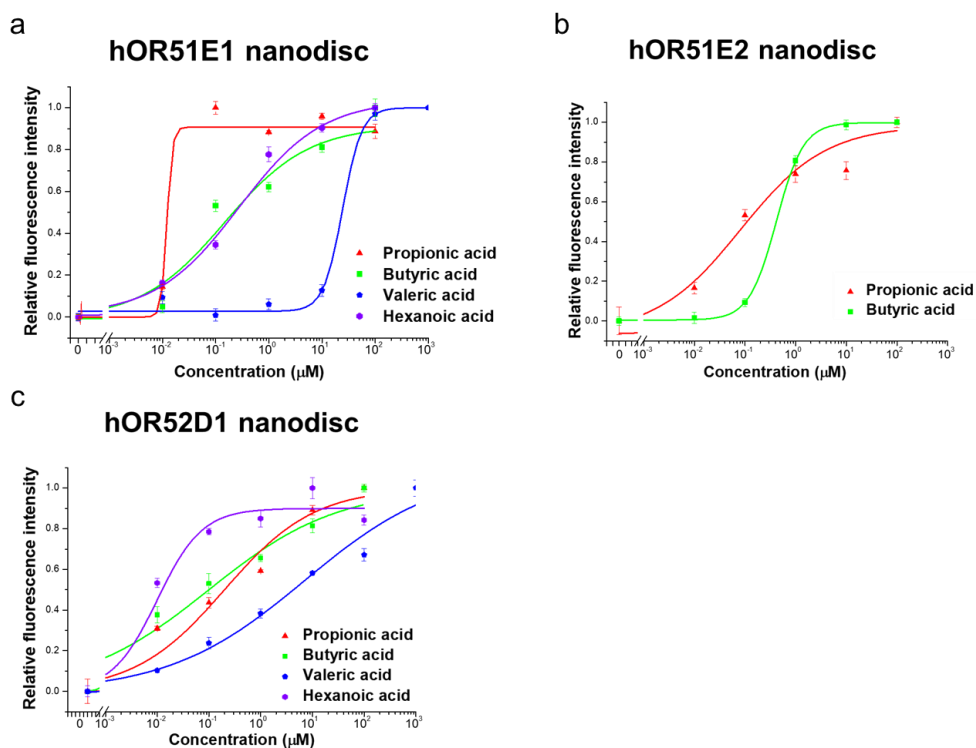
Figure 6.2 Tryptophan fluorescence quenching assay for dose-dependent responses of human olfactory receptor-embedded nanodiscs to gastric cancer biomarkers

		OR-embedded nanodiscs		
		hOR51E1	hOR51E2	hOR52D1
Gastric cancer biomarkers	Propionic acid	0.013	0.13	0.20
	Butyric acid	0.22	0.36	0.09
	Valeric acid	26	N.D.	4.98
	Hexanoic acid	0.22	N.D.	0.01

EC_{50} (µM): half maximal effective concentration

Table 6.1 Half maximal effective concentration of hOR51E1, hOR51E2 and hOR52D1 nanodiscs to each gastric cancer biomarkers

6.3 Patterns for gastric cancer biomarkers in artificial saliva

Through several researches, the amount of gastric cancer biomarkers present in exhaled breath of healthy group and gastric cancer patients was identified, and the concentration when dissolved in artificial saliva was estimated through Henry's law solubility constants for each odorants (**Table 6.2**)[141]. By combining the estimated concentration of gastric cancer biomarkers, healthy and patient artificial saliva samples were prepared (**Table 6.3**).

Human OR-embedded NDs showed different patterns for each sample (**Figure 6.3**).

a

Gastric cancer VOCs	Healthy	Gastric cancer
Propionic acid	0-1 ppb	5.8-49 ppb
Butyric acid	0.4-1.6 ppb	0.7-5.9 ppb
Valeric acid	0.2-0.5 ppb	0.2-0.7 ppb
Hexanoic acid	0.1-0.7 ppb	0.2-2.8 ppb

b

Gastric cancer VOCs	Healthy	Gastric cancer
Propionic acid	0-2 µM	27.4-232 µM
Butyric acid	1.9-7.6 µM	3.3-28 µM
Valeric acid	243-608 nM	243-851 nM
Hexanoic acid	132-922 nM	0.26-3.7 µM

Table 6.2 (a) Concentration of gastric cancer VOCs in exhaled breath and (b) Estimated concentration of gastric cancer biomarkers in artificial saliva

a

	Healthy 1	Healthy 2	Healthy 3	Healthy 4	Healthy 5	Healthy 6	Healthy 7	Healthy 8	Healthy 9	Healthy 10	Healthy 11	Healthy 12	Healthy 13	Healthy 14	Healthy 15	Healthy 16
Propionic acid	0 µM	0 µM	0 µM	0 µM	2 µM	2 µM	2 µM	2 µM	0 µM	0 µM	0 µM	0 µM	2 µM	2 µM	2 µM	2 µM
Butyric acid	1.9 µM	1.9 µM	7.6 µM	7.6 µM	1.9 µM	1.9 µM	7.6 µM	7.6 µM	1.9 µM	1.9 µM	7.6 µM	7.6 µM	1.9 µM	1.9 µM	7.6 µM	7.6 µM
Valeric acid	243 nM	608 nM	243 nM	608 nM	243 nM	608 nM	243 nM	608 nM	243 nM	608 nM	243 nM	608 nM	243 nM	608 nM	243 nM	608 nM
Hexanoic acid	132 nM	132 nM	132 nM	132 nM	132 nM	132 nM	132 nM	132 nM	922 nM	922 nM	922 nM	922 nM	922 nM	922 nM	922 nM	922 nM

b

	Gastric cancer 1	Gastric cancer 2	Gastric cancer 3	Gastric cancer 4	Gastric cancer 5	Gastric cancer 6	Gastric cancer 7	Gastric cancer 8	Gastric cancer 9	Gastric cancer 10	Gastric cancer 11	Gastric cancer 12	Gastric cancer 13	Gastric cancer 14	Gastric cancer 15	Gastric cancer 16
Propionic acid	27.4 µM	27.4 µM	27.4 µM	27.4 µM	232 µM	232 µM	232 µM	232 µM	27.4 µM	27.4 µM	27.4 µM	27.4 µM	232 µM	232 µM	232 µM	232 µM
Butyric acid	3.3 µM	3.3 µM	28 µM	28 µM	3.3 µM	3.3 µM	28 µM	28 µM	3.3 µM	3.3 µM	28 µM	28 µM	3.3 µM	3.3 µM	28 µM	28 µM
Valeric acid	243 nM	851 nM	243 nM	851 nM	243 nM	851 nM	243 nM	851 nM	243 nM	851 nM	243 nM	851 nM	243 nM	851 nM	243 nM	851 nM
Hexanoic acid	260 nM	260 nM	260 nM	260 nM	260 nM	260 nM	260 nM	260 nM	3.7 µM	3.7 µM	3.7 µM	3.7 µM	3.7 µM	3.7 µM	3.7 µM	3.7 µM

Table 6.3 (a) Artificial saliva samples of healthy control and (b) gastric cancer patients
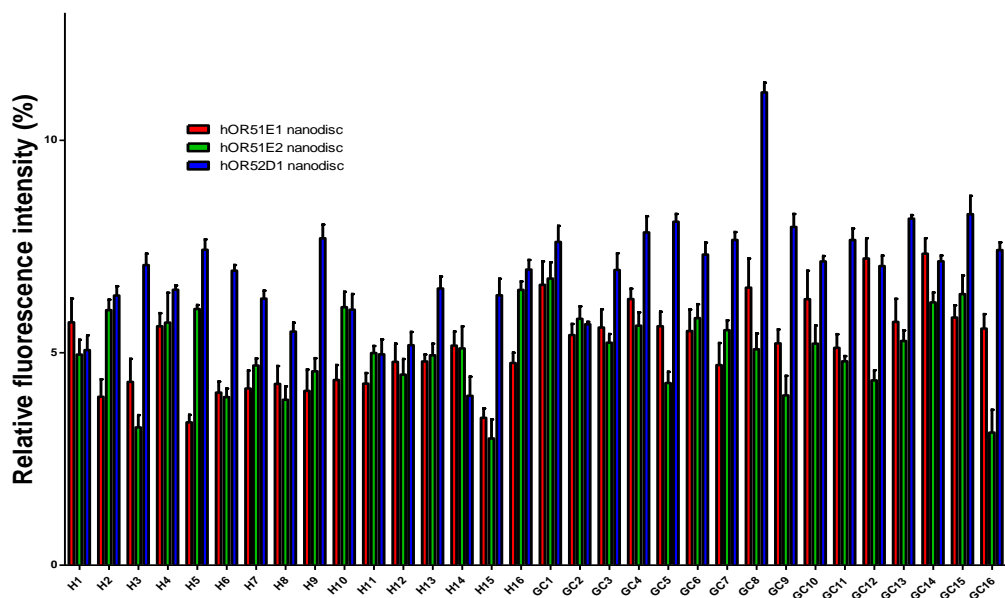
Figure 6.3 Tryptophan fluorescence quenching assay patterns of hOR-embedded NDs to artificial saliva samples

H: Healthy control sample, GC: Gastric cancer sample

6.4 Principal component analysis for artificial saliva samples

Principal component analysis score plot was obtained after dimensionality reduction of tryptophan fluorescence quenching signals of artificial saliva samples (**Figure 6.4**).

The first two components (PC1 and PC2) explained 80.6% of total variance, covering most of original variables. Overall, the healthy group had lower PC1 value than the gastric cancer patient group. Through principal component analysis, it was possible to classify healthy group and gastric cancer patient group, and it was confirmed that healthy group and gastric cancer patient group could be distinguished by human OR NDs.
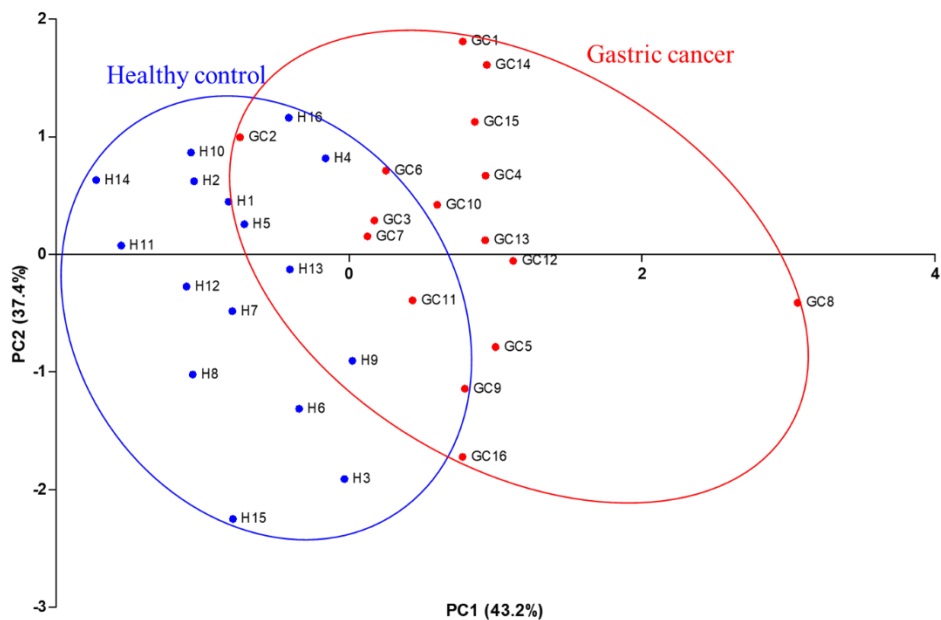
Figure 6.4 Principal component analysis of healthy control and gastric cancer patient artificial saliva samples

H: Healthy control sample, GC: Gastric cancer sample

6.5 Conclusions

In this study, human OR-embedded NDs (hOR51E1, hOR51E2 and hOR52D1) showed different patterns for gastric cancer biomarkers. Also, the NDs had different binding affinity to each target molecules. The different binding affinity to biomarkers would contribute to distinguish healthy group and gastric cancer patients.

In the experiment using artificial saliva, it was confirmed through principal component analysis that human OR ND could sufficiently distinguish healthy group from the gastric cancer patient group. This pattern analysis using the human OR NDs can be applied to BE-nose, and it is expected that in the future, it will be able to precisely diagnose gastric cancer patients and healthy groups.

Chapter 7

Pattern analysis for halitosis biomarkers in artificial saliva using olfactory receptor-embedded nanodiscs

7.1 Introduction

Halitosis is a broad term that refers to any unpleasant odor that emanates from the mouth, air, or breath, regardless of the source of the odor compounds[91–93]. VOCs in human breath will have originated from multiple sources inside the respiratory system. There are three major VOC sources that can be identified: (1) exogenous sources; VOCs inspired from background ambient gases and then expelled; (2) extra-oral; from microbes further down the respiratory tract (oropharynx, bronchioles), or else blood- circulatory VOCs that enter the lungs and are removed from the body through gaseous exchange; and (3) intra-oral; microbial VOCs from microbial biofilms encountered in the oral cavity[94]. Because of microbial activity from biofilms within the oral cavity, the majority of human people with halitosis (80 to 90 percent) have oral malodour[92].

The VOCs causing halitosis are sulfur compounds, diamines, short-chain fatty acids, alcohols, phenyl compounds and ketones (**Table 2.4**).

In this chapter, OR embedded-NDs, hOR51B4, hOR52D1 and TAAR13d, were used for patterns of halitosis biomarkers. ND is a suitable platform for reconstitution of ORs because of its stable structure for transmembrane proteins. Samples of healthy group and halitosis patients were prepared with artificial saliva dissolving halitosis biomarkers, and it was confirmed through principal component analysis

that healthy group and halitosis patients could be distinguished through the OR-embedded ND.

7.2 Characterization of olfactory receptor-embedded nanodiscs

The composition of the ORs and MSP1E3D1 in the NDs was confirmed by SDS-PAGE analysis (**Figure 7.1**). hOR51B4, hOR52D1 and TAAR13d bands were observed at approximately 38 kDa, and the MSP1E3D1 band was observed at approximately 30 kDa.

The size distribution and homogeneity of the OR-embedded NDs were analyzed by DLS. The average diameters of hOR51B4, hOR52D1 and TAAR13d were 8 nm, 14 nm and 11.7 nm respectively (**Figure 7.2**).
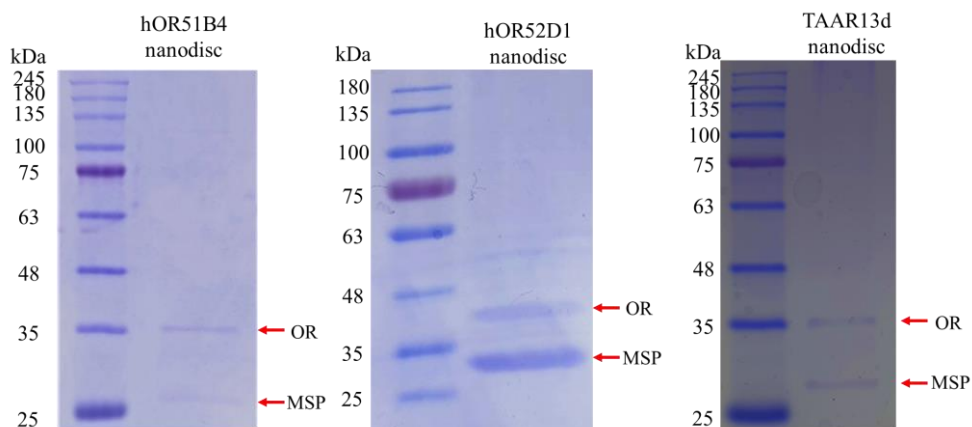
Figure 7.1 Coomassie blue staining analysis of purified hOR51B4, hOR52D1 and TAAR13d NDs
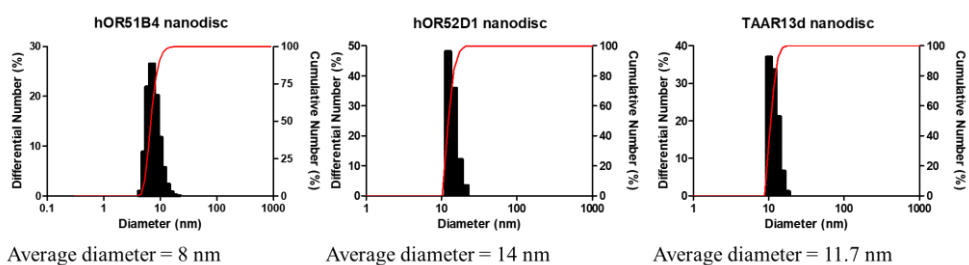
Figure 7.2 DLS profiles of hOR51B4, hOR52D1 and TAAR13d NDs

7.3 Patterns for halitosis biomarkers in artificial saliva

Through several researches, the amount of halitosis biomarkers present in saliva of healthy group and malodour patients was identified (**Table 7.1**)[142–145]. In particular, it was confirmed that propionic acid, butyric acid, and PT were dissolved at high concentrations in the saliva of malodour patients.

By combining three VOCs dissolved in high concentration in the saliva of malodour patients, artificial saliva samples of healthy and malodour patients were prepared (**Table 7.2**).

OR-embedded NDs showed different patterns for each sample (**Figure 7.3**).

Malodour VSCs and VOCs	Healthy	Malodor
Hydrogen sulfide	0-3 nM	4.6-21.6 nM
Methyl mercaptan	0-10 nM	13-77 nM
Dimethyl sulfide	0-4 nM	2.6-13.6 nM
Propionic acid	607-823 μM	0.8-9.5 mM
Butyric acid	43-73 μM	0.2-2.6 mM
Valeric acid	0 μM	86.2 nM
Putrescine	30-172 μM	0.1-3.5 mM
Cadaverine	7.83-26.4 μM	18.6-104 μM
Indole	119-385 nM	80.9-347 nM

Table 7.1 Concentration of malodour VSCs and VOCs in saliva

The three odorants dissolved in the highest concentration in saliva are marked in red.

a

	Heathy 1	Healthy 2	Healthy 3	Healthy 4	Healthy 5	Healthy 6	Healthy 7	Healthy 8
Propionic acid	607 μM	607 μM	607 μM	607 μM	823 μM	823 μM	823 μM	823 μM
Butyric acid	43 μM	43 μM	73 μM	73 μM	43 μM	43 μM	73 μM	73 μM
Putrescine	30 μM	172 μM	30 μM	172 μM	30 μM	172 μM	30 μM	172 μM

b

	Malodour 1	Malodour 2	Malodour 3	Malodour 4	Malodour 5	Malodour 6	Malodour 7	Malodour 8
Propionic acid	0.8 mM	0.8 mM	0.8 mM	0.8 mM	9.5 mM	9.5 mM	9.5 mM	9.5 mM
Butyric acid	0.2 mM	0.2 mM	2.6 mM	2.6 mM	0.2 mM	0.2 mM	2.6 mM	2.6 mM
Putrescine	0.1 mM	3.5 mM	0.1 mM	3.5 mM	0.1 mM	3.5 mM	0.1 mM	3.5 mM

Table 7.2 (a) Artificial saliva samples of healthy control and (b) malodour patients
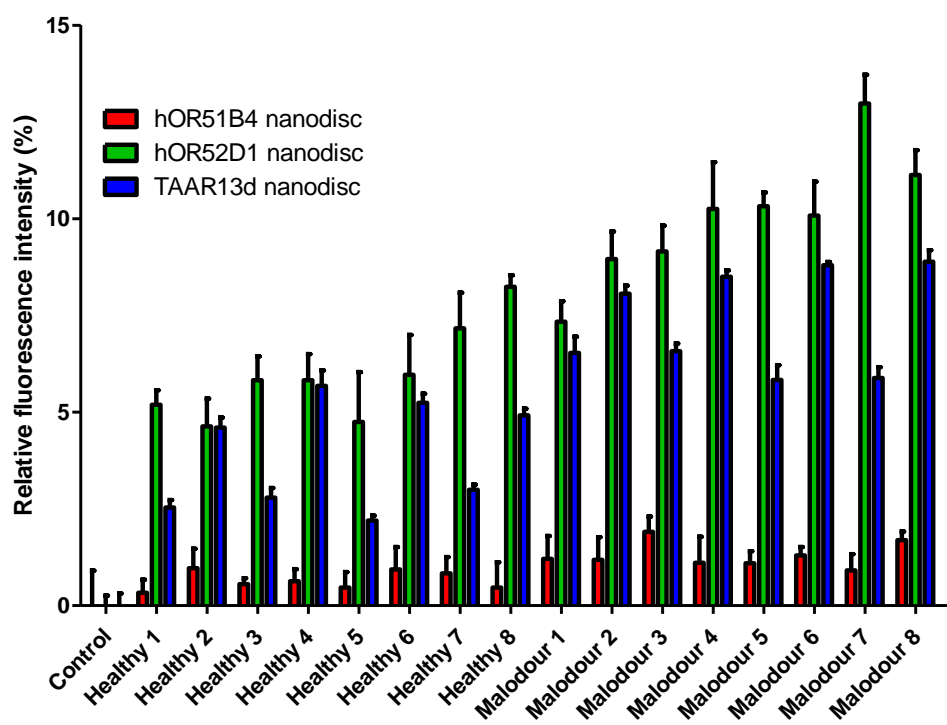
Figure 7.3 Patterns for halitosis biomarkers in artificial saliva

7.4 Principal component analysis for artificial saliva samples

Principal component analysis score plot was obtained after dimensionality reduction of tryptophan fluorescence quenching signals of artificial saliva samples (**Figure 7.4**).

The first two components (PC1 and PC2) explained 87.4% of total variance, covering most of original variables. Overall, the healthy group had lower PC2 value than the malodour group. Through principal component analysis, it was possible to classify healthy group and malodour patient group, and it was confirmed that healthy group and malodour patient group could be distinguished by OR NDs.
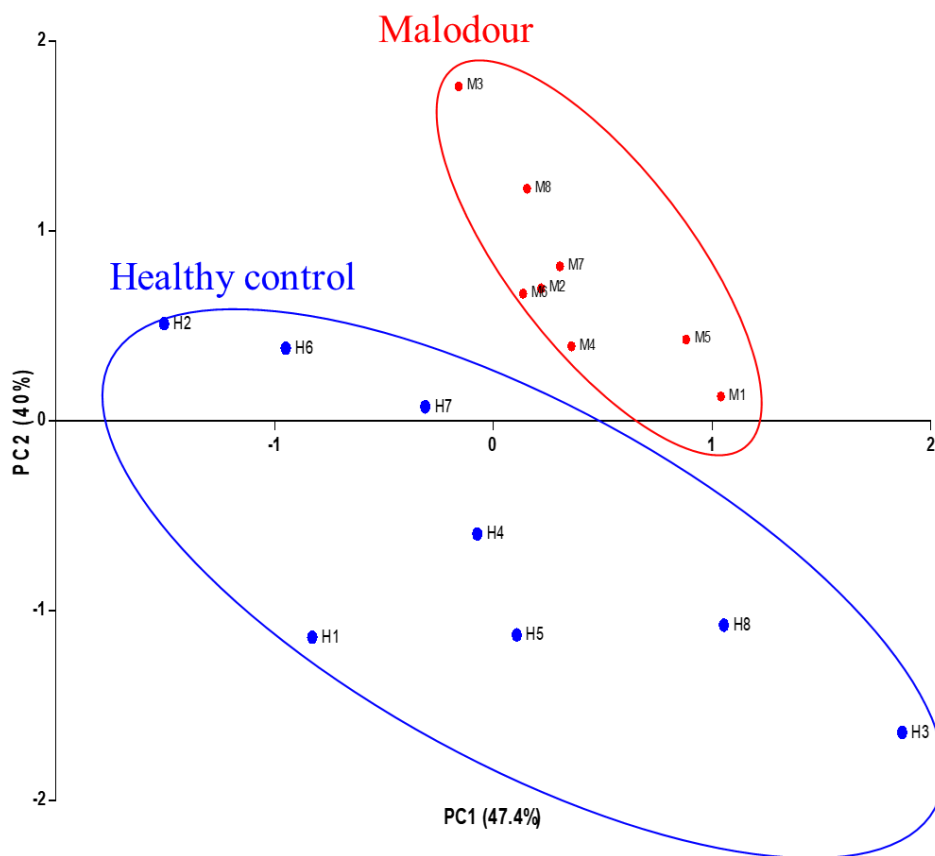
Figure 7.4 Principal component analysis plot for artificial saliva samples

H: Healthy control sample, M: Malodour patient sample

7.5 Conclusions

In this study, OR-embedded NDs (hOR51B4, hOR52D1 and TAAR13d) were highly purified and had proper diameters for biomaterials detecting target odorants. The NDs showed different patterns for artificial samples.

Through principal component analysis, it was proven that OR NDs could sufficiently discriminate the healthy group from the malodour patient group in an experiment using artificial saliva. This pattern analysis employing OR NDs can be applied to BE-nose and is expected to be able to precisely diagnose malodour patients and healthy groups in the future.

Chapter 8

Visual detection of geraniol using human olfactory receptor embedded in polydiacetylene/lipid nanovesicle

8.1 Introduction

Human ORs are the starting material for olfaction, and transmit a generated signal to the cerebrum by reacting with various odorants in air[146]. The hORs are seven-transmembrane receptors and bind to their specific olfactory ligands. Therefore, they are very useful for developing BE-noses to clearly distinguish between target odorants and control molecules[44,63,69]. These noses could be applied to a wide range of fields, such as disease diagnosis[45], food quality[49,51,52,147], and environmental monitoring[47]. However, until now, they can confirm the sense of smell only by an electrical signal which cannot be recognized by naked eye immediately. Therefore, various materials have been evaluated to overcome this limitation. A chromatic supramolecule consisting of π-conjugated molecules was used in this study.

Supramolecules could be used in a wide range of fields, including electronic materials, biotechnology, and environmental and chemical engineering[148,149]. A supramolecular body contains an artificial biomimetic membrane that simulates the structure of the cell membrane[150,151]. The surface that reacts as a chemical functional group is maximized and can interfere with other ions when dissolved in a solution[152]. Especially, PDA in the supramolecular body shows a chromatic transition from blue to red and a fluorescent transition from non-fluorescent to red-fluorescent against various stimulations, such as temperature, pH, solvent, a molecular recognition process (such as

ligand-receptor or antigen-antibody reaction), and mechanical stimulation[153–158]. The properties of these diacetylenes are maintained even in the presence of the phospholipid domains in vesicles[109,159]. In previous studies, a target molecule was detected by embedding a synthetic receptor in supramolecules consisting of phospholipid and PDAs[160,161], and the lipid morphology was confirmed by inserting rhodopsin in the polymerizable lipid[162].

In this study, for the first time, a novel PDA lipid bilayer was functionalized successfully with hORs (PDA/hORs). Polymerization of the membrane assembly containing hORs enabled the formation of a robust bilayer and minimally affected the hOR structure and activity. The nano-assembly showed selectivity to the target odorant of the hOR and a color transition from blue to purple, allowing of the visual detection of odorant. This could be applicable in biological and chemical technologies, such as environmental assessment and analysis of food quality.

8.2 Functionality of hOR1A2 embedded in detergent micelle and PDA/lipid nanovesicle

The functionality of hOR1A2 in detergent micelle was confirmed by tryptophan fluorescence quenching assay. Tryptophan which is sensitive to surrounding polarity of peptide or protein is selectively excited at 295

nm. When a receptor binds to its ligand, the conformation change of receptor causes the fluorescence quenching of tryptophan by photoinduced electron transfer reaction[163,164]. The geraniol is ligand of hOR1A2[71]. For confirming the functionality of hOR1A2 in detergent micelle, we selected the various odorants having similar scent or similar chemical structure (**Figure 8.1**).

hOR1A2 in detergent micelle bound to the target molecules, geraniol, dose-dependently (**Figure 8.2 (a)**) and specifically (**Figure 8.2 (b)**). Through the dose-dependent test and selectivity test, we confirmed that hOR1A2 produced in *E. coli* have the same functionality with produced in eukaryotic cell[47,71].
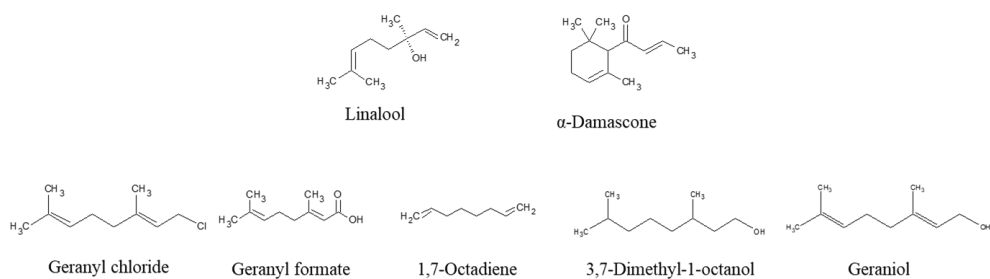
Figure 8.1 Chemical structure of odorants for selectivity test
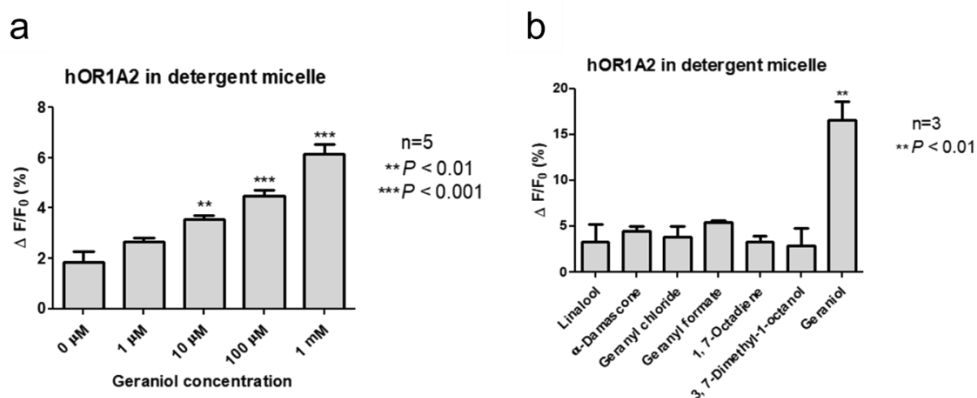
Figure 8.2 (a) Dose dependent test of hOR1A2 in detergent micelle with target odorant using tryptophan fluorescence quenching assay. (b) Selectivity test of hOR1A2 in detergent micelle with various odorants using tryptophan fluorescence quenching assay

8.3 Structural assay of hOR1A2 embedded in detergent micelle and PDA/lipid nanovesicle

The structure and function of hOR1A2 embedded in PDA complexes was confirmed using a CD spectrum analysis and the tryptophan quenching method. The hORs, seven-transmembrane proteins, are mainly composed of alpha helices. When well-folded hORs were analysed by CD spectrum, they show strong negative double peaks at approximately 210–230 nm wavelength[49], which is similar to the CD spectrum graph of hOR1A2 in detergent micelle. However, the hOR1A2 in elution buffer has no peak (**Figure 8.3 (b)**). The hOR has the ability to selectively discriminate different structures of odorants. Polymerization of the membrane assembly that contained embedded hORs enabled the formation of a robust bilayer and minimally affected the hOR structure and activity, as shown in **Figure 8.3 (a)** and (**c**). PDA/hOR complexes showed the dose-dependently fluorescence quenching when the target molecule, geraniol, was treated. However, PDA vesicle without hOR1A2 showed no fluorescence quenching or inconstant signal when geraniol was treated (**Figure 8.3 (c)**). The function of hOR1A2 was remained after embedded in PDA complexes same as in detergent micelle (**Figure 8.2**).
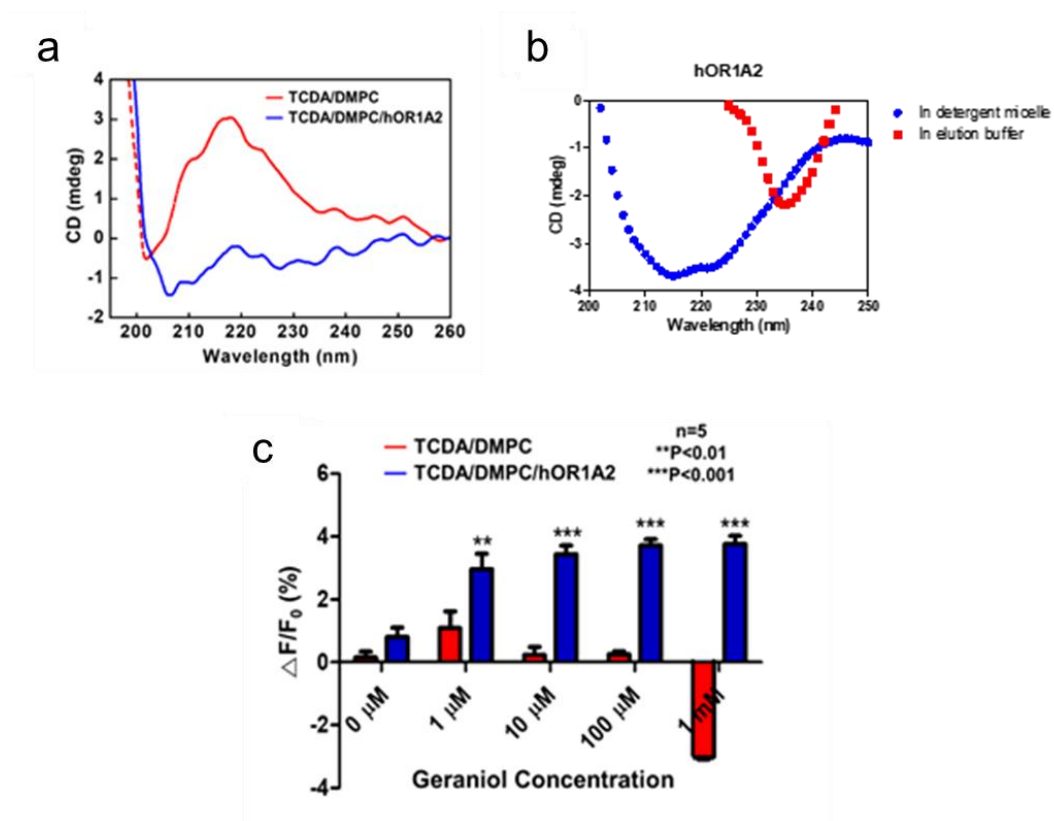
Figure 8.3 Structural and functional assay of the PDA vesicles and PDA/hOR complexes

(a) CD spectrum. (b) CD spectrum of hOR in elution buffer and detergent micelle. (c) Tryptophan fluorescence quenching of the PDA vesicles and PDA/hOR complexes

8.4 Size analysis and morphology of hOR1A2 embedded in PDA/lipid nanovesicle

The membrane of the polymerized assembly would undergo deformation resulting from conformational changes of hORs reacted with target odorants, showing chromatic and fluorescence transitions. Approximately 3 to 5 nm surfactant-capped hOR1A2 proteins were observed using HRTEM as shown in **Figure 8.4 (a)**. The morphology of the PDA vesicles and PDA/hOR complexes was examined by FE-SEM, as shown in **Figure 8.4 (b)** and **(c)**. The PDA vesicles had a uniform distribution of particles, whereas the PDA/hOR complexes showed aggregation of the particles. The shape and surface of these assemblies were confirmed by HR-TEM, as shown in the insets of **Figure 8.4 (b)** and **(c)**. In these images, unlike the PDA vesicle, the surface of the PDA/hOR complex showed that surfactant-capped hOR1A2 proteins were gathered around the assembly. The size distribution of these particles was obtained from DLS, and the PDA/hOR complexes were larger on average (~189 nm) than the PDA vesicles (~129 nm) (**Figure 8.5**)
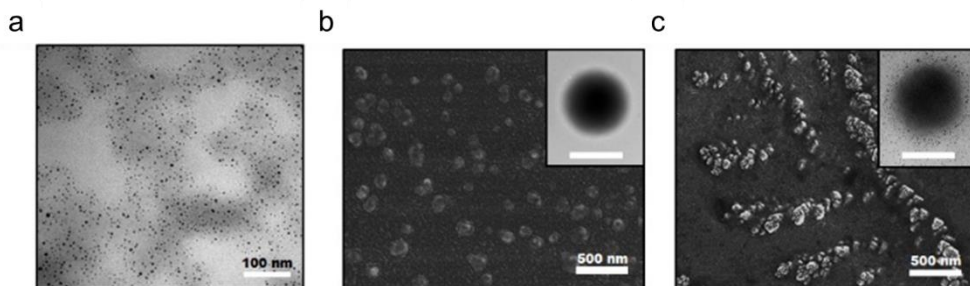
Figure 8.4 Morphology of the PDA vesicle and PDA/hOR complex

(a) HR-TEM image of hOR1A2. Field-emission scanning electron microscopy (FE-SEM) image of (b) the PDA vesicles and (c) the PDA/hOR complexes (Inset: HR-TEM images of those. The scale bar of the insets corresponds to 150 nm.)
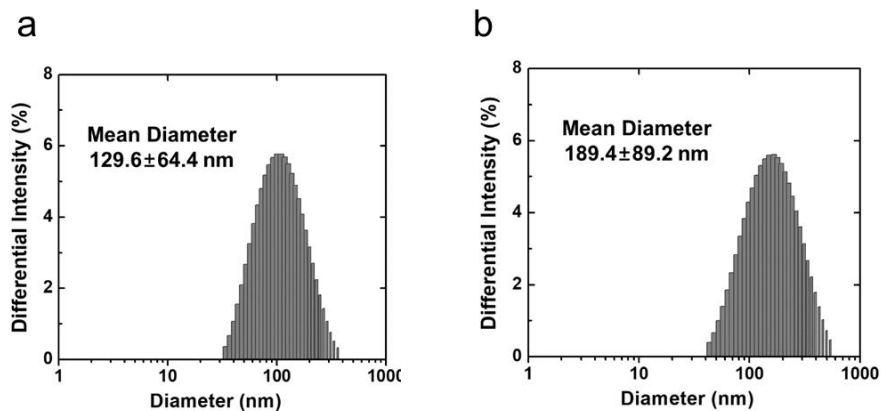
Figure 8.5 DLS data of the particles. Intensity distribution of (A) the PDA vesicles and (B) PDA/hOR complexes

The measurements were conducted at room temperature (RT).

8.5 Photoluminescence intensity of hOR1A2 embedded in PDA/lipid nanovesicle

Figure 8.6 (a) shows the PL spectra of the PDA and PDA/hOR assemblies as a function of the concentration of geraniol molecules. In this figure, the PL spectra of the assembly without the hOR1A2 proteins do not change. Conversely, the PL peaks of the hOR1A2 embedded assembly at 556 and 626 nm increased by an increase of the concentration of geraniol in a dose-dependent manner. This could be because a conformational change of hOR1A2 from the target reaction perturbs the ordered structures of the PDA/hOR complexes, thus causing the fluorescence transition. **Figure 8.6 (b)** shows the integrated fluorescence intensity areas of these assemblies from 530 to 720 nm as a function of the concentration of geraniol. This figure shows the difference in reactivity with the target of the hOR-embedded assemblies in comparison to the vesicles.

Finally, the interaction selectivity of the PDA/hOR complexes was evaluated using various odorants, such as geraniol, TMA, helional, and AB. These odorants are the target molecules of hOR1A2, TAAR5, hOR3A1, and hOR2AG1, respectively. As shown in **Figure 8.6 (c)**, the PL spectra of the hOR1A2-embedded assembly with the odorants had a different fluorescence intensity at the same concentration (1 mM). The PL spectrum of the assembly that reacted with geraniol showed the highest response (approximately 3.8 times), and this was also confirmed

in the inset image of **Figure 8.6 (c)**. For the reaction with geraniol, the PDA/hOR complex solutions showed an intense purple color, whereas other cases showed an intense blue or slight purple color. In addition, as shown in **Figure 8.6 (d)**, this spectroscopic result and image were in agreement with the quantitative ratio values of the fluorescence intensity of the assembly after incubation with geraniol or other odorants. These values were the ratios of the integrated fluorescence intensity area of PDA/hOR with DMSO (PL_0) to that of PDA/hOR with the odorants (PL) from 530 to 720 nm. In this figure, the minimal reactivity of the assembly with helional was obtained because helional is a secondary target molecule of the hOR1A2[71]. The colorimetric response measurements showed a similar tendency as the PL spectroscopic results (**Figure 8.7**).
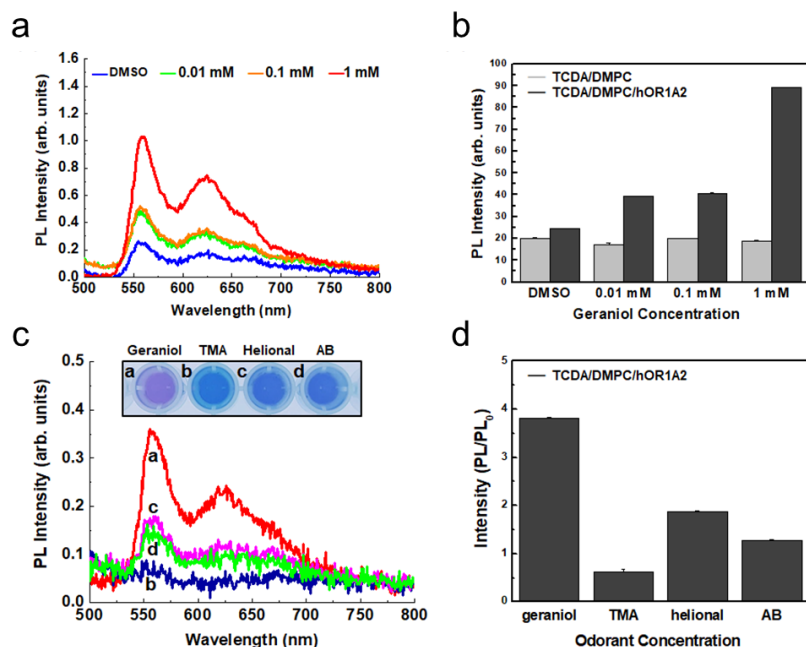
Figure 8.6 Dose dependence and selectivity test of the PDA vesicles and PDA/hOR complexes

(a) PL spectra of the PDA/hOR complexes with geraniol (0.01, 0.1, and 1 mM). (b) Integrated PL intensity of the PDA vesicles (control experiment) and PDA/hOR complexes with geraniol (0.01, 0.1, and 1mM). (c) PL spectra of the PDA/hOR complexes with **a** geraniol, **b** trimethylamine (TMA), **c** helional, and **d** amyl butyrate (AB) (1 mM) (inset: photograph of the PDA/hOR complexes with odorants). (d) Integrated PL intensity ratio of the PDA/hOR complexes with odorants. The parameter PL0 is the integrated area from 530 to 720 nm of the TCDA/DMPC/hOR1A2 with DMSO, and PL is the integrated area from 530 to 720 nm of the TCDA/DMPC/hOR1A2 with the odorants. The excitation wavelength was 450 nm.
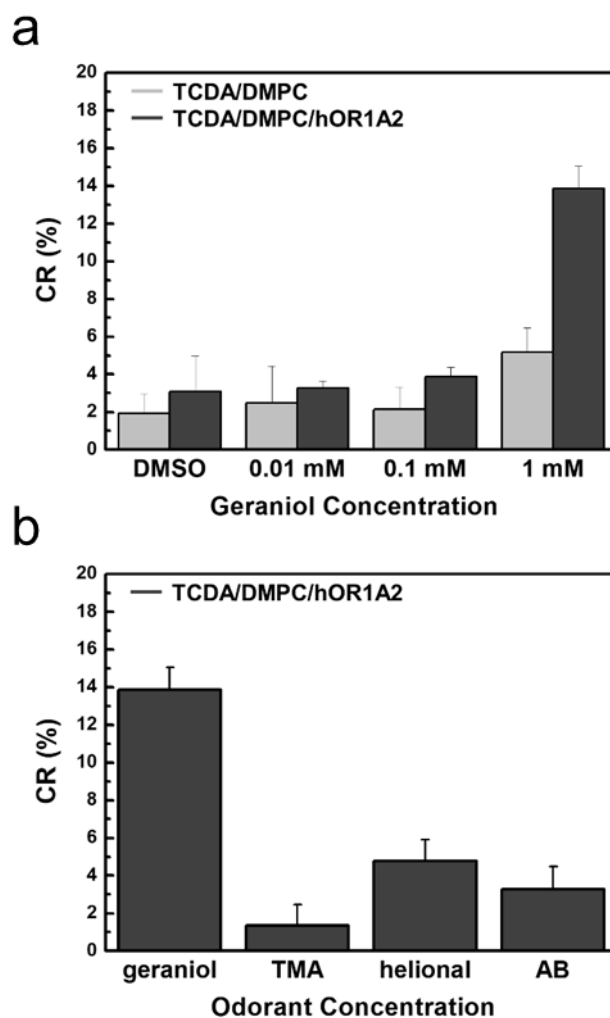
Figure 8.7 (a) Colorimetric dose-dependence test of the PDA vesicles and PDA/hOR complexes with geraniol (0.01, 0.1, and 1 mM). (b) Colorimetric selectivity test of the PDA/hOR complexes with geraniol, trimethylamine (TMA), helional, and amyl butyrate (AB) (1 mM)

8.6 Conclusions

In summary a PDA nano-assembly was functionalized successfully with hORs to react with specific odorants, for the first time. In the assembly, the structural and functional properties of the hOR1A2 were maintained. When the PDA/hOR complexes reacted with the target molecules, the fluorescence intensity of the assembly drastically increased in a dose-dependent manner, showing selectivity to geraniol, the target odorant of the hOR1A2 unlike other odorants, including TMA, helional, and AB. Hence, the visual detection of odorant was enabled by the reaction of the chromatic complexes with the target caused a color transition of the assembly from blue to purple. This novel hOR-embedded chromatic nano-assembly was robust and easy to prepare and could be utilized as odorant visualization in a wide range of biological and chemical technologies, such as environmental assessment and analysis of food quality.

Chapter 9

Overall discussion and further suggestions

Overall discussion and further suggestions

OR reconstituted into ND, detergent micelle and vesicle are very important technique for development of BE-nose or pattern analysis of odorants because of its specific function to target odorants and stability to various environment. OR-embedded ND, detergent micelle and vesicle have been applied for diagnosing diseases, monitoring food quality and environment.

Three basic principles emerge from spatial patterns of ORs. First, individual odorants activate subsets of receptors. This finding lends support to a hypothesis of combinatorial coding in which most odorants are identified not by the response of a single receptor, but by a pattern of receptor responses. Second, subsets of odorants activate particular receptors. ORs vary in their breadth of tuning: some are broadly tuned, responding to many odorants, while others are narrowly tuned, responding to only a few specific odorants. Broadly tuned receptors are particularly sensitive to odorants that are structurally similar. Third, increased odorant concentrations stimulate activity from a larger number of receptors. Thus, the number of active receptors represents both odor strength and odor identity[38–43].

In chapter 4, OR was overexpressed by co-expressing effector genes, such as *djlA*, the membrane-bound DnaK cochaperone, and *rraA*, inhibitor of the mRNA-degrading activity of *E. coli* RNase E. The *E.*

coli strains coexpressing DjlA or RraA suppressed protein-induced toxicity and overexpressed the ORs. By controlling the molar ratio of OR, membrane scaffold protein, and phospholipid, ND of appropriate size were made, and high-purity ND could be purified. OR-embedded NDs showed stability to various temperature and storage time.

In chapter 5, human OR embedded-NDs, hOR51E1, hOR51E2 and hOR52D1, were used for patterns of short-chain fatty acids. Short-chain fatty acids, such as propionic, butyric and valeric acids, were reported as biomarkers for gastric cancer or halitosis. ND is a suitable platform for reconstitution of hORs because of its stable structure for transmembrane proteins. There were no reports about patterns of odors using hOR-embedded NDs. Through tryptophan fluorescence quenching assay, the hOR-embedded NDs respectively had different EC_{50} values to short-chain fatty acids. Propionic acid had the lowest EC_{50} value when it bound with hOR51E1 ND, while butyric and valeric acid had the lowest EC_{50} value when it bound with hOR52D1 ND. The different binding affinity of hOR-embedded NDs to short-chain fatty acids caused different patterns or identities. Samples of healthy group and gastric cancer patients were prepared with artificial saliva dissolving short-chain fatty acids, and it was confirmed through principal component analysis that healthy group and gastric cancer patients could be distinguished through the hOR-embedded ND.

In chapter 6, we developed TAAR ND-based BE-nose for monitoring

meat freshness/spoilage. TAAR13c and TAAR13d, as ORs were utilized for specific recognition of the biogenic amines and were reconstituted with NDs to improve their functionality. The real-time responses of side-gated field-effect transistors (SG-FETs) toward various indicators showed high sensitivity and selectivity, and the LOD was 1 fM for CV and PT. In the gas sensor system, the LODs were 26.48 ppb for CV and 7.29 ppb for PT, indicating high performance. In addition, for the first time, a wireless portable TAAR13 NDs BE-nose integrated with commercial gas sensors allowed multiple monitoring of spoilage indicators from real food samples and showed high-performance and sensitivity. Our sensor system opens up the possibility of a portable TAAR13 NDs BE-nose system for on-site and in-situ freshness/spoilage monitoring.

In chapter 7, OR embedded-NDs, hOR51B4, hOR52D1 and TAAR13d, were used for patterns of halitosis biomarkers. ND is a suitable platform for reconstitution of ORs because of its stable structure for transmembrane proteins. Samples of healthy group and halitosis patients were prepared with artificial saliva dissolving halitosis biomarkers, and it was confirmed through principal component analysis that healthy group and halitosis patients could be distinguished through the OR-embedded ND.

In chapter 8, for the first time, a novel PDA lipid bilayer was functionalized successfully with hORs (PDA/hORs). Polymerization of

the membrane assembly containing hORs enabled the formation of a robust bilayer and minimally affected the hOR structure and activity. The nano-assembly showed selectivity to the target odorant of the hOR and a color transition from blue to purple, allowing of the visual detection of odorant. This could be applicable in biological and chemical technologies, such as environmental assessment and analysis of food quality.

In this thesis, various ORs were successfully reconstituted with ND or nanovesicles. The reconstructed OR is expected to be applied to food freshness monitoring, disease diagnosis by pattern analysis, and practical colorimetric sensors. In order to develop advanced technology that mimics the olfactory system, it is essential to high-throughput produce and reconstruct several ORs at once through cell-free protein expression. This approach could be applied to manufacturing various OR-embedded NDs at once, and time-consuming or labor-intensive tasks such as cell lysis and removal of detergent by Bio-Beads could be eliminated. It is expected that this research can be used in various fields such as disease diagnosis and food freshness monitoring in the future.

Bibliography

1   A. Sharma, R. Kumar, I. Aier, R. Semwal, P. Tyagi and P. Varadwaj, *Curr. Neuropharmacol.*, 2018, **17**, 891–911.

2   S. Katada, M. Tanaka and K. Touhara, *J. Neurochem.*, 2004, 90, 1453–1463.

3   S. Zozulya, F. Echeverri and T. Nguyen, *Genome Biol.*, 2001, **2**, 1–12.

4   X. Zhang and S. Firestein, *Nat. Neurosci.*, 2002, **5**, 124–133.

5   P. Duchamp-Viret, M. A. Chaput and A. Duchamp, *Science (80-.).*, 1999, **284**, 2171–2179.

6   A. T. Schaefer and T. W. Margrie, *Trends Neurosci.*, 2007, **30**, 92–100.

7   H. Spors and A. Grinvald, *Neuron*, 2002, **34**, 301–315.

8   J. J. Hopfield, *Pattern recognition computation using action potential timing for stimulus representation*, 1995, vol. 376.

9   A. S. Ghatpande and J. Reisert, *J. Physiol.*, 2011, **589**, 2261–2273.

10   P. F. Kent, M. M. Mozell, S. J. Murphy and D. E. Hornung, *J. Neurosci.*, 1996, **16**, 345–353.

11   M. M. Mozell, *J. Gen. Physiol.*, 1970, **56**, 46–63.

12   J. Jiang and K. Zhao, *J. Aerosol Sci.*, 2010, **41**, 1030–1043.

13   S. Junek, E. Kludt, F. Wolf and D. Schild, *Neuron*, 2010, **67**, 872–884.

14   S. Wagner, L. Baarst, A. J. Ytterberg, A. Klussmerer, C. S. Wagner, O. Nord, P. Å. Nygren, K. J. Van Wijks and J. W. De Gier, *Mol. Cell. Proteomics*, 2007, **6**, 1527–1550.

15   S. Wagner, M. L. Bader, D. Drew and J. W. de Gier, *Trends Biotechnol.*, 2006, **24**, 364–371.

16   S. Mallipeddi, N. Zvonok and A. Makriyannis, *Sci. Rep.*, 2018, **8**, 1–11.

17   K. Michalke, C. Huyghe, J. Lichière, M. E. Gravière, M. Siponen, G. Sciara, I. Lepaul, R. Wagner, C. Magg, R. Rudolph, C. Cambillau and A. Desmyter, *Anal. Biochem.*, 2010, **401**, 74–80.

18   S. Inagaki, R. Ghirlando, J. F. White, J. Gvozdenovic-Jeremic, J. K.

Northup and R. Grisshammer, *J. Mol. Biol.*, 2012, **417**, 95–111.

19   L. E. Petrovskaya, A. A. Shulga, O. V. Bocharova, Y. S. Ermolyuk, E. A. Kryukova, V. V. Chupin, M. J. J. Blommers, A. S. Arseniev and M. P. Kirpichnikov, *Biochem.*, 2010, **75**, 881–891.

20   H. Attrill, P. J. Harding, E. Smith, S. Ross and A. Watts, *Protein Expr. Purif.*, 2009, **64**, 32–38.

21   A. J. Link, G. Skretas, E.-M. Strauch, N. S. Chari and G. Georgiou, *Protein Sci.*, 2008, **17**, 1857–1863.

22   I. Dodevski and A. Plückthun, *J. Mol. Biol.*, 2011, **408**, 599–615.

23   C. Klenk, J. Ehrenmann, M. Schutz and A. Pluckthun, *Sci. Rep.*, 2016, **6**, 1–9.

24   A. Rinaldi, *EMBO Rep.*, 2007, **8**, 629–633.

25   P. Mombaerts, F. Wang, C. Dulac, S. K. Chao, A. Nemes, M. Mendelsohn, J. Edmondson and R. Axel, *Cell*, 1996, **87**, 675–686.

26   J. A. Ballesteros, A. D. Jensen, G. Liapakis, S. G. F. Rasmussen, L. Shi, U. Gether and J. A. Javitch, *J. Biol. Chem.*, 2001, **276**, 29171–29177.

27   S. P. Sheikh, T. A. Zvyaga, O. Lichtarge, T. P. Sakmar and H. R. Bourne, *Nature*, 1996, **383**, 347–350.

28   D. L. Farrens, C. Altenbach, K. Yang, W. L. Hubbell and H. G. Khorana, *Science (80-.).*, 1996, **274**, 768–770.

29   H. Breer, I. Boekhoff and E. Tareilus, *Nature*, 1990, **345**, 65–68.

30   U. B. Kaupp, *Nat. Rev. Neurosci.*, 2010, **11**, 188–200.

31   L. Belluscio, G. H. Gold, A. Nemes and R. Axel, *Neuron*, 1998, **20**, 69–81.

32   L. J. Brunet, G. H. Gold and J. Ngai, *Neuron*, 1996, **17**, 681–693.

33   J. Zheng and W. N. Zagotta, *Neuron*, 2004, **42**, 411–421.

34   A. Kato and K. Touhara, *Cell. Mol. Life Sci.*, 2009, **66**, 3743–3753.

35   S. T. Wong, K. Trinh, B. Hacker, G. C. K. Chan, G. Lowe, A. Gaggar, Z. Xia, G. H. Gold and D. R. Storm, *Neuron*, 2000, **27**, 487–497.

36   S. Pifferi, A. Boccaccio and A. Menini, *FEBS Lett.*, 2006, **580**, 2853–

2859.

37   D. Schild and D. Restrepo, *Physiol. Rev.*, 1998, **78**, 429–466.

38   E. A. Hallem and J. R. Carlson, *Cell*, 2006, **125**, 143–160.

39   C. Y. Su, K. Menuz and J. R. Carlson, *Cell*, 2009, **139**, 45–59.

40   S. A. Kreher, D. Mathew, J. Kim and J. R. Carlson, *Neuron*, 2008, **59**, 110–124.

41   B. Malnic, J. Hirono, T. Sato and L. B. Buck, *Cell*, 1999, **96**, 713–723.

42   H. Saito, Q. Chi, H. Zhuang, H. Matsunami and J. D. Mainland, *Sci. Signal.*, 2009, **2**, ra9.

43   Y. Xia, G. Wang, D. Buscariollo, R. J. Pitts, H. Wenger and L. J. Zwiebel, *Proc. Natl. Acad. Sci. U. S. A.*, 2008, **105**, 6433–6438.

44   H. J. Jin, S. H. Lee, T. H. Kim, J. Park, H. S. Song, T. H. Park and S. Hong, *Biosens. Bioelectron.*, 2012, **35**, 335–341.

45   J. H. Lim, J. Park, E. H. Oh, H. J. Ko, S. Hong and T. H. Park, *Adv. Healthc. Mater.*, 2014, **3**, 360–366.

46   J. Park, J. H. Lim, H. J. Jin, S. Namgung, S. H. Lee, T. H. Park and S. Hong, *Analyst*, 2012, **137**, 3249–3254.

47   M. Son, D. G. Cho, J. H. Lim, J. Park, S. Hong, H. J. Ko and T. H. Park, *Biosens. Bioelectron.*, 2015, **74**, 199–206.

48   J. H. Lim, E. H. Oh, J. Park, S. Hong and T. H. Park, *ACS Nano*, 2015, **9**, 1699–1706.

49   M. Son, D. Kim, H. J. Ko, S. Hong and T. H. Park, *Biosens. Bioelectron.*, 2017, **87**, 901–907.

50   M. Son, D. Kim, J. Kang, J. H. Lim, S. H. Lee, H. J. Ko, S. Hong and T. H. Park, *Anal. Chem.*, 2016, **88**, 11283–11287.

51   S. H. Lee, J. H. Lim, J. Park, S. Hong and T. H. Park, *Biosens. Bioelectron.*, 2015, **71**, 179–185.

52   J. H. Lim, J. Park, J. H. Ahn, H. J. Jin, S. Hong and T. H. Park, *Biosens. Bioelectron.*, 2013, **39**, 244–249.

53   H. Yang, D. Kim, J. Kim, D. Moon, H. S. Song, M. Lee, S. Hong and T. H. Park, *ACS Nano*, 2017, **11**, 11847–11855.

54   M. Lee, H. Yang, D. Kim, M. Yang, T. H. Park and S. Hong, *Sci. Rep.*, 2018, **8**, 1–12.

55   B. Wang, J. C. Cancilla, J. S. Torrecilla and H. Haick, *Nano Lett.*, 2014, **14**, 933–938.

56   S. Y. Tian, S. P. Deng and Z. X. Chen, *Sensors Actuators, B Chem.*, 2007, **123**, 1049–1056.

57   Q. Liu, W. Ye, L. Xiao, L. Du, N. Hu and P. Wang, *Biosens. Bioelectron.*, 2010, **25**, 2212–2217.

58   Q. Liu, F. Zhang, D. Zhang, N. Hu, K. J. Hsia and P. Wang, *Biosens. Bioelectron.*, 2013, **43**, 186–192.

59   H. J. Ko and T. H. Park, *Biosens. Bioelectron.*, 2005, **20**, 1327–1332.

60   H. J. Ko, S. H. Lee, E. H. Oh and T. H. Park, *Bioprocess Biosyst. Eng.*, 2010, **33**, 55–62.

61   S. R. Ahn, J. H. An, H. S. Song, J. W. Park, S. H. Lee, J. H. Kim, J. Jang and T. H. Park, *ACS Nano*, 2016, **10**, 7287–7296.

62   S. J. Park, O. S. Kwon, S. H. Lee, H. S. Song, T. H. Park and J. Jang, *Nano Lett.*, 2012, **12**, 5082–5090.

63   W. Yoon, S. H. Lee, O. S. Kwon, H. S. Song, E. H. Oh, T. H. Park and J. Jang, *Angew. Chemie – Int. Ed.*, 2009, **48**, 2755–2758.

64   S. H. Lee, O. S. Kwon, H. S. Song, S. J. Park, J. H. Sung, J. Jang and T. H. Park, *Biomaterials*, 2012, **33**, 1722–1729.

65   S. R. Ahn, J. H. An, I. H. Jang, W. Na, H. Yang, K. H. Cho, S. H. Lee, H. S. Song, J. Jang and T. H. Park, *Biosens. Bioelectron.*, 2018, **117**, 628–636.

66   I. G. Denisov and S. G. Sligar, *Chem. Rev.*, 2017, **117**, 4669–4713.

67   H. J. Ko and T. Hyun Park, *Biol. Chem.*, , DOI:10.1515/bc.2006.009.

68   O. S. Kwon, H. S. Song, S. J. Park, S. H. Lee, J. H. An, J. W. Park, H. Yang, H. Yoon, J. Bae, T. H. Park and J. Jang, *Nano Lett.*, 2015, **15**, 6559–6567.

69   T. H. Kim, S. H. Lee, J. Lee, H. S. Song, E. H. Oh, T. H. Park and S. Hong, *Adv. Mater.*, 2009, **21**, 91–94.

70   S. H. Lee, H. J. Jin, H. S. Song, S. Hong and T. H. Park, *J. Biotechnol.*, 2012, **157**, 467–472.

71   C. A. de March, S. E. Ryu, G. Sicard, C. Moon and J. Golebiowski, *Flavour Fragr. J.*, 2015, **30**, 342–361.

72   Z. Li, P. Hobson, W. An, M. D. Burch, J. House and M. Yang, *Water Res.*, 2012, **46**, 5165–5173.

73   M. H. Azarbad and H. Jeleń, *Food Anal. Methods*, 2015, **8**, 1727–1733.

74   T. Z. Wu and Y. R. Lo, *J. Biotechnol.*, 2000, **80**, 63–73.

75   P. Dalgaard, H. L. Madsen, N. Samieian and J. Emborg, *J. Appl. Microbiol.*, 2006, **101**, 80–95.

76   G. Luna, R. Aparicio and D. L. García-González, *Food Chem.*, 2006, **97**, 621–630.

77   C. Deng, X. Zhang and N. Li, *J. Chromatogr. B Anal. Technol. Biomed. Life Sci.*, 2004, **808**, 269–277.

78   F. Bray, J. Ferlay, I. Soerjomataram, R. L. Siegel, L. A. Torre and A. Jemal, *CA. Cancer J. Clin.*, 2018, **68**, 394–424.

79   M. Plummer, S. Franceschi, J. Vignat, D. Forman and C. De Martel, *Int. J. Cancer*, 2015, **136**, 487–490.

80   I. W. G. on the E. of C. R. to Humans, *IARC Monogr. Eval. Carcinog. Risks to Humans*, 2012, **100E**, 46–167.

81   C. P. Howson, T. Hiyama and E. L. Wynder, *Epidemiol. Rev.*, 1986, **8**, 1–27.

82   M. E. Adam, M. Fehervari, P. R. Boshier, S. T. Chin, G. P. Lin, A. Romano, S. Kumar and G. B. Hanna, *Anal. Chem.*, 2019, **91**, 3740–3746.

83   S. Kumar, J. Huang, N. Abbassi-Ghadi, H. A. MacKenzie, K. A. Veselkov, J. M. Hoare, L. B. Lovat, P. Spanel, D. Smith and G. B. Hanna, *Ann. Surg.*, 2015, **262**, 981–990.

84   S. Kumar, J. Huang, N. Abbassi-Ghadi, P. Španěl, D. Smith and G. B. Hanna, *Anal. Chem.*, 2013, **85**, 6121–6128.

85   A. Romano, S. Doran, I. Belluomo and G. B. Hanna, *Anal. Chem.*, 2018,

90, 10204–10210.

86   S. A. Jones, R. N. Butler, I. R. Sanderson and J. W. Wilson, *Exp. Cell Res.*, 2004, **292**, 29–39.

87   K. Daly and S. P. Shirazi-Beechey, *DNA Cell Biol.*, 2006, **25**, 49–62.

88   G. M. Matthews, G. S. Howarth and R. N. Butler, *Cancer Biol. Ther.*, 2007, **6**, 1051–1057.

89   S. R. Markar, T. Wiggins, S. Antonowicz, S. T. Chin, A. Romano, K. Nikolic, B. Evans, D. Cunningham, M. Mughal, J. Lagergren and G. B. Hanna, *JAMA Oncol.*, 2018, **4**, 970–976.

90   J. Huang, S. Kumar, N. Abbassi-Ghadi, P. Španěl, D. Smith and G. B. Hanna, *Anal. Chem.*, 2013, **85**, 3409–3416.

91   B. Aylikci and H. Çolak, *J. Nat. Sci. Biol. Med.*, 2013, **4**, 14–23.

92   M. Aydin and C. N. Harvey-Woodworth, *Gene Ther.*, 2014, **21**, E1.

93   G. Campisi, A. Musciotto, O. Di Fede, V. Di Marco and A. Craxì, *Intern. Emerg. Med.*, 2011, **6**, 315–319.

94   R. M. S. Thorn and J. Greenman, *J. Breath Res.*, , DOI:10.1088/1752-7155/6/2/024001.

95   C. Ruiz-Capillas and A. M. Herrero, *Foods*, 2019, **8**, 62.

96   X. Y. Xu, X. Lian, J. N. Hao, C. Zhang and B. Yan, *Adv. Mater.*, 2017, **29**, 1702298.

97   L. D. Kaale, T. M. Eikevik, T. Rustad and K. Kolsaker, *J. Food Eng.*, 2011, **107**, 141–146.

98   C. Rukchon, A. Nopwinyuwong, S. Trevanich, T. Jinkarn and P. Suppakul, *Talanta*, 2014, **130**, 547–554.

99   D. Dave and A. E. Ghaly, *Am. J. Agric. Biol. Sci.*, 2011, **6**, 486–510.

100   A. Halász, Á. Baráth, L. Simon-Sarkadi and W. Holzapfel, *Trends Food Sci. Technol.*, 1994, 5, 42–49.

101   Z. Xu and Q. Li, *Cell. Mol. Neurobiol.*, 2020, **40**, 257–272.

102   S. Bover-Cid, M. Izquierdo-Pulido and M. Carmen Vidal-Carou, *Meat Sci.*, 2001, **57**, 215–221.

103   A. R. Shalaby, *Food Res. Int.*, 1996, **29**, 675–690.

104   R. Draisci, G. Volpe, L. Lucentini, A. Cecilia, R. Federico and G. Palleschi, *Food Chem.*, 1998, **62**, 225–232.

105   M. Triki, A. M. Herrero, F. Jiménez-Colmenero and C. Ruiz-Capillas, *Foods*, , DOI:10.3390/foods7090132.

106   D. Gialama, K. Kostelidou, M. Michou, D. C. Delivoria, F. N. Kolisis and G. Skretas, *ACS Synth. Biol.*, 2017, **6**, 284–300.

107   D. Gialama, D. C. Delivoria, M. Michou, A. Giannakopoulou and G. Skretas, *J. Mol. Biol.*, 2017, **429**, 1800–1816.

108   M. UniversityMichou, C. Kapsalis, C. Pliotas and G. Skretas, *ACS Synth. Biol.*, 2019, **8**, 1631–1641.

109   Y. Porat, S. Kolusheva, R. Jelinek and E. Gazit, *Biochemistry*, 2003, **42**, 10971–10977.

110   J. Oh, H. Yang, G. E. Jeong, D. Moon, O. S. Kwon, S. Phyo, J. Lee, H. S. Song, T. H. Park and J. Jang, *Anal. Chem.*, 2019, **91**, 12181–12190.

111   F. Hagn, M. L. Nasr and G. Wagner, *Nat. Protoc.*, 2018, **13**, 79–98.

112   J. Ma, Y. Lu, D. Wu, Y. Peng, W. Loa-Kum-Cheung, C. Peng, R. J. Quinn, W. Shui and Z. J. Liu, *Anal. Methods*, 2017, **9**, 5851–5858.

113   D. Dave and A. E. Ghaly, *Am. J. Agric. Biol. Sci.*, 2011, **6**, 486–510.

114   B. De Las Rivas, Á. Marcobal, A. V. Carrascosa and R. Muñoz, *J. Food Prot.*, 2006, **69**, 2509–2514.

115   Z. Ma, P. Chen, W. Cheng, K. Yan, L. Pan, Y. Shi and G. Yu, *Nano Lett.*, 2018, **18**, 4570–4575.

116   H. Kim, B. T. Trinh, K. H. Kim, J. Moon, H. Kang, K. Jo, R. Akter, J. Jeong, E. K. Lim, J. Jung, H. S. Choi, H. G. Park, O. S. Kwon, I. Yoon and T. Kang, *Biosens. Bioelectron.*, 2021, **179**, 113063.

117   M. K. Morsy, K. Zór, N. Kostesha, T. S. Alstrøm, A. Heiskanen, H. El-Tanahi, A. Sharoba, D. Papkovsky, J. Larsen, H. Khalaf, M. H. Jakobsen and J. Emnéus, *Food Control*, 2016, **60**, 346–352.

118   C. Schaude, C. Meindl, E. Fröhlich, J. Attard and G. J. Mohr, *Talanta*, 2017, **170**, 481–487.

119   A. T. S. Semeano, D. F. Maffei, S. Palma, R. W. C. Li, B. D. G. M.

Franco, A. C. A. Roque and J. Gruber, *Food Control*, 2018, **89**, 72–76.

120   T. Siripongpreda, K. Siralertmukul and N. Rodthongkum, *Food Chem.*, 2020, **329**, 127165.

121   M. Valdez, S. K. Gupta, K. Lozano and Y. Mao, *Sensors Actuators, B Chem.*, 2019, **297**, 126734.

122   S. D. Liberles, in *Annals of the New York Academy of Sciences*, 2009, vol. 1170, pp. 168–172.

123   S. D. Liberles, *Curr. Opin. Neurobiol.*, 2015, **34**, 1–7.

124   Q. Li, Y. Tachie-Baffour, Z. Liu, M. W. Baldwin, A. C. Kruse and S. D. Liberles, *Elife*, , DOI:10.7554/eLife.10441.

125   A. Hussain, L. R. Saraiva, D. M. Ferrero, G. Ahuja, V. S. Krishna, S. D. Liberles and S. I. Korsching, *Proc. Natl. Acad. Sci. U. S. A.*, 2013, **110**, 19579–19584.

126   H. Zhuang and H. Matsunami, *Nat. Protoc.*, 2008, **3**, 1402–1413.

127   Y. R. Li and H. Matsunami, *Sci. Signal.*, , DOI:10.1126/scisignal.2001230.

128   H. Zhuang and H. Matsunami, *J. Biol. Chem.*, 2007, **282**, 15284–15293.

129   T. Kim, D. Moon, J. H. Park, H. Yang, S. Cho, T. H. Park and D. J. Ahn, *Nanoscale*, 2019, **11**, 7582–7587.

130   H. Yang, H. S. Song, S. R. Ahn and T. H. Park, *Biotechnol. Bioprocess Eng.*, 2015, **20**, 423–430.

131   K. H. Kim, S. H. Lee, S. E. Seo, J. Bae, S. J. Park and O. S. Kwon, *Micromachines*, 2020, **11**, 439.

132   B. Y. Lee, M. G. Sung, J. Lee, K. Y. Baik, Y. K. Kwon, M. S. Lee and S. Hong, *ACS Nano*, 2011, **5**, 4373–4379.

133   S. H. Lee, K. H. Kim, S. E. Seo, M. il Kim, S. J. Park and O. S. Kwon, *J. Ind. Eng. Chem.*, 2020, **83**, 29–34.

134   S. J. Park, S. E. Seo, K. H. Kim, S. H. Lee, J. Kim, S. Ha, H. S. Song, S. H. Lee and O. S. Kwon, *Biosens. Bioelectron.*, 2021, **174**, 112804.

135   A. Pircher, F. Bauer and P. Paulsen, *Eur. Food Res. Technol.*, 2007,

226, 225–231.

136   D. Mayr, R. Margesin, E. Klingsbichel, E. Hartungen, D. Jenewein, F. Schinner and T. D. Märk, *Appl. Environ. Microbiol.*, 2003, **69**, 4697–4705.

137   S. Bover-Cid, S. Torriani, V. Gatto, R. Tofalo, G. Suzzi, N. Belletti and F. Gardini, *J. Appl. Microbiol.*, 2009, **106**, 1397–1407.

138   F. Zhao, G. Zhou, K. Ye, S. Wang, X. Xu and C. Li, *Meat Sci.*, 2015, **100**, 145–149.

139   R. Reid, S. Fanning, P. Whyte, J. Kerry, R. Lindqvist, Z. Yu and D. Bolton, *Food Microbiol.*, 2017, **61**, 50–57.

140   L. Buňková, F. Buňka, G. Mantlová, A. Čablová, I. Sedláček, P. Švec, V. Pachlová and S. Kráčmar, *Food Microbiol.*, 2010, **27**, 880–888.

141   R. Sander, *Atmos. Chem. Phys.*, 2015, **15**, 4399–4981.

142   J. Dadamio, M. Van Tornout, F. Vancauwenberghe, R. Federico, C. Dekeyser and M. Quirynen, *J. Clin. Periodontol.*, 2012, **39**, 645–650.

143   R. Niederman, Y. Buyle-Bodin, B. Y. Lu, P. Robinson and C. Naleway, *J. Dent. Res.*, 1997, **76**, 575–579.

144   X. Yu, A.-M. Shahir, J. Sha, Z. Feng, B. Eapen, S. Nithianantham, B. Das, J. Karn, A. Weinberg, N. F. Bissada and F. Ye, *J. Virol.*, 2014, **88**, 4466–4479.

145   S. Van Den Velde, D. Van Steenberghe, P. Van Hee and M. Quirynen, *J. Dent. Res.*, 2009, **88**, 285–289.

146   S. Firestein, *Nature*, 2001, **413**, 211–218.

147   J. H. Ahn, J. H. Lim, J. Park, E. H. Oh, M. Son, S. Hong and T. H. Park, *Sensors Actuators, B Chem.*, 2015, **210**, 9–16.

148   Y. J. Kim, J. H. Kim, M. S. Kang, M. J. Lee, J. Won, J. C. Lee and Y. S. Kang, *Adv. Mater.*, 2004, **16**, 1753–1757.

149   T. Hasegawa, T. Fujisawa, M. Numata, M. Umeda, T. Matsumoto, T. Kimura, S. Okumura, K. Sakurai and S. Shinkai, *Chem. Commun.*, 2004, 2150–2151.

150   T. Kuwana, M. R. Mackey, G. Perkins, M. H. Ellisman, M. Latterich, R.

Schneiter, D. R. Green and D. D. Newmeyer, *Cell*, 2002, **111**, 331–342.

151   T. Aida, E. W. Meijer and S. I. Stupp, *Science (80-.)*, 2012, **335**, 813–817.

152   T. F. Otero, J. G. Martinez and J. Arias-Pardilla, *Electrochim. Acta*, 2012, **84**, 112–128.

153   A. Berman, D. J. Ahn, A. Lio, M. Salmeron, A. Reichert and D. Charych, *Science (80-.)*, 1995, **269**, 515–518.

154   S. Okada, S. Peng, W. Spevak and D. Charych, *Acc. Chem. Res.*, 1998, **31**, 229–239.

155   J. T. Cho, S. M. Woo, D. J. Ahn, K. D. Ahn, H. Lee and J. M. Kim, *Chem. Lett.*, 2003, **32**, 282–283.

156   J. M. Kim, J. S. Lee, H. Choi, D. Sohn and D. J. Ahn, *Macromolecules*, 2005, **38**, 9366–9376.

157   J. A. Dong and J. M. Kim, *Acc. Chem. Res.*, 2008, **41**, 805–816.

158   D. J. Ahn, S. Lee and J. M. Kim, *Adv. Funct. Mater.*, 2009, **19**, 1483–1496.

159   S. Kolusheva, E. Wachtel and R. Jelinek, *J. Lipid Res.*, 2003, **44**, 65–71.

160   S. Kolusheva, O. Molt, M. Herm, T. Schrader and R. Jelinek, *J. Am. Chem. Soc.*, 2005, **127**, 10000–10001.

161   S. Friedman, S. Kolusheva, R. Volinsky, L. Zeiri, T. Schrader and R. Jelinek, *Anal. Chem.*, 2008, **80**, 7804–7811.

162   V. Subramaniam, G. D. D'Ambruoso, H. K. Hall, R. J. Wysocki, M. F. Brown and S. S. Saavedra, *Langmuir*, 2008, **24**, 11067–11075.

163   S. M. D. Akbar, K. Sreeramulu and H. C. Sharma, *J. Bioenerg. Biomembr.*, 2016, **48**, 241–247.

164   N. Marmé, J. P. Knemeyer, J. Wolfrum and M. Sauer, *Angew. Chemie – Int. Ed.*, 2004, **43**, 3798–3801.

국문초록

G 단백질 연결 수용체 (GPCR)는 약물 표적 스크리닝을 위해 가장 집중적으로 연구되는 단백질이다. 특히, GPCR 계열의 약 85%를 차지하는 후각 수용체 (OR)를 포함하는 클래스 A GPCR은 표적 수용체를 코드화하고 스크리닝하는 데 더 중요하다. 인간의 후각 시스템에는 약 400 종류의 OR이 있다. OR과 냄새 물질 사이의 상호 작용은 패턴의 조합으로 뇌에 전달되는 신호를 생성한다. 인간은 말초 후각 코딩의 억제 및 향상과 같은 광범위한 OR에 의한 조절로 인해 제한된 수의 OR로도 1조개 이상의 후각 신호를 구별할 수 있다. 후각은 복잡한 외부 세계를 패턴으로 인식하기 때문에 OR의 반응을 모방하기 위해 많은 연구가 수행되었다. 특히, 단백질 기반 나노바이오센서는 양산성, 재사용 용이성, 저비용 등의 장점이 있어 후각을 모방하는 플랫폼으로 기대된다.

그러나 GPCR 구조의 재구성은 대장균 시스템에서 생성되는 거의 모든 GPCR이 봉입체로 발현되기 때문에 어려운 일이다. 이러한 이유로 세제 미셀, 나노베지클, 바이셀 및 나노디스크 (ND)와 같은 GPCR의 기능을 복구하기 위한 재구성 기술이 개발되었다. 이들 물질 중 ND는 다양한 환경에서의 안정성과 기능적 수명 때문에 가장 효과적인 재구성 물질로 여겨져 왔다.

본 논문에서는 대장균 시스템에서 높은 생산성으로 OR을 생산하여 나노디스크 또는 나노베지클 형태로 구조를 재구성하였다. 그런 다음 기능적

으로 재구성된 OR을 육류 신선도/부패 모니터링, 질병 진단 및 실용적인 비색 센서에 적용했다.

첫째, OR은 *djlA*, 막 결합 DnaK cochaperone 및 *rraA*, *E. coli* RNase E의 mRNA 분해 활성 억제제와 같은 이펙터 유전자를 공동 발현함으로써 과 발현되었다. DjlA 또는 RraA를 공동 발현하는 대장균 균주는 단백질 발현에 의한 독성을 억제하고 후각 수용체를 과발현했습니다. 후각 수용체, 막 지지체 단백질, 인지질의 몰비를 조절하여 적절한 크기의 ND를 만들고 고순도 ND를 정제할 수 있었다. 후각 수용체가 내장된 ND는 다양한 온도 및 보관 시간에 대해 안정성을 보였다.

둘째, 위암 및 구취 바이오마커에 결합하는 인간 OR은 ND 형태로 성공적으로 재구성되고 정제되었다. ND는 표적 분자에 대한 다양한 결합 친화성을 가졌기 때문에 인공 타액 샘플에 대한 다양한 패턴을 가졌다. 인공 타액 샘플에 대한 다양한 패턴의 주성분 분석을 통해 건강한 대조군 샘플과 환자 샘플을 구별할 수 있었다.

셋째, 미량 아민 관련 수용체 (TAAR), TAAR13c 및 TAAR13d가 대장균 시스템에서 성공적으로 과발현되었고 ND 형태로 재구성되었다. 이러한 ND는 육류 신선도를 모니터링하기 위한 ND 기반 전자 코의 개발에 활용되었다. ND 기반 전자 코는 다양한 현장 및 실제 샘플에 성공적으로 작동되었으며 육류의 신선도를 모니터링하는 데 사용할 수 있었다.

마지막으로 인간 OR1A2 (hOR1A2)를 세제 미셀로 재구성하여 제라니올을 감지하는 비색 센서 개발에 활용하였다. 폴리다이아세틸렌 (PDA)은 후각 수용체의 반응을 시각화하기 위한 2차 변환기로 사용되었다. hOR1A2의 구조적 및 기능적 특성은 PDA/지질 나노베지클에 내장되었을 때 유지되었다. PDA/지질 나노베지클에 내장된 hOR1A2가 geraniol과 반응할 때 파란색에서 보라색으로 색상 전이를 일으킨 반면 다른 분자와 반응할 때는 색상 전이가 없었습니다.

이 연구에서는 다양한 OR이 ND 또는 나노베지클로 성공적으로 재구성되었다. 재구성된 OR은 식품 신선도 모니터링, 패턴 분석에 의한 질병 진단 및 실용적인 비색 센서에 적용될 수 있을 것으로 기대가 된다.

주요어: G 단백질 연결 수용체, 후각수용체, 나노바이오센서, 대장균, 나노디스크, 나노베지클

학 번: 2015-22830   **성 명:** 문동석